

The high rate mechanical properties of energetic materials, their binders or simulants

17th Technical Meeting, 2007
Cambridge, United Kingdom

Theoretical Development of EOS and Constitutive Models for PBXsD. Porter¹ and P.J. Gould²¹QinetiQ Ltd., Farnborough GU14 0LX, UK²QinetiQ Ltd., Bristol BS16 1EJ, UK.**Abstract**

In this paper, we outline the development of a self-consistent set of models to predict the equation of state (EOS) and constitutive model for a PBX, and polymeric materials in general. The models are based upon the energy of interaction between characteristic groups of atoms, and all the model parameters can be calculated directly in terms of the chemical structure and hierarchical morphology of the material. The high-rate EOS is calculated directly from the potential function of binding energy as a function of volume in a polymer, and PBXs are treated as a composite of polymeric binder and energetic particles using specific additivity rules. Rate-dependent constitutive models for polymers are based upon the bulk elastic modulus from the EOS, and engineering moduli are calculated from the energy dissipated through thermomechanical processes at the molecular level during deformation. The change in temperature of the main loss peaks with rate is the basis of the rate dependence of mechanical properties. Finally, a constitutive model for PBXs is presented that includes damage in the form of debonding of the matrix from the energetic particles, thereby reducing the active elastic modulus in proportion to the fraction of debonded sites.

Introduction and Outline

In the past, polymers and organic materials have presented particular difficulties for the prediction of high-rate equations of state and constitutive models, due to their unusual macromolecular chain structure and the relative magnitude of the different energy terms that determine key physical properties such as modulus, thermal expansion, and melting temperature.

The initial aim of this work was to develop a theoretical high-rate equation of state (EOS) for polymers and PBXs that accurately reproduced all the pressure and temperature nonlinearities observed in plate impact experiments. Moreover, the model should be derived from the structure of the materials at the molecular level; thereby making a direct link between their composition and properties to provide insights for the development of new and improved materials or the solution of problems with current ones. Another major driver for this approach was that a quantitative understanding of thermal and mechanical properties of the components of a PBX would allow us to explore in detail how thermal energy develops and is distributed in the binder and energetic components under impact conditions.

The development of such an EOS was described in previous DYMAT papers, and moved from a straightforward use of molecular dynamic simulations [1] to a much simpler method based upon mean-field potential functions [2], which is outlined below in the section on equations of state. The practical result is that we can now predict a full nonlinear EOS for a polymer or PBX in the form of a PVT profile or Hugoniot Us-Up plot in a matter of minutes. If the composition of the material is correctly specified, predictions usually fall within the bounds of experimental variability. Equally important, modelling can now address situations where little or no experimental data is available, and where engineering simulations need to be performed quickly in response to events in the field

The next major step was to be able to predict the constitutive behaviour of polymeric materials as a general function of rate, rather than the relatively simple property of bulk elastic modulus under shock conditions. Ideally, the EOS properties should just be the limiting high rate values of the engineering moduli described by the constitutive equation. Fortunately, we had already developed a basic model framework for polymer properties, based upon the same mean-field approach used for the EOS, which is called Group Interaction Modelling (GIM) [3]. Coincidentally, a paper by Mulliken and Boyce [4] showed empirically that the GIM approach could be refined as the basis for a full rate and temperature-dependent constitutive model for thermoplastic polymers, which is outlined below in the section on constitutive models.

Finally, we needed to incorporate damage into the PBX constitutive model to quantify the irreversible deterioration in mechanical properties under mechanical deformation. Clearly, this would also allow us to explore how damage might change the thermomechanical response of a PBX, and its consequential effect upon the hazard response of the material. Fortunately again, we had already developed a model for the mechanical properties of a specific particulate composite in the form of concrete, which is composed of higher modulus filler particles (sand and aggregate) in a binder matrix of cement. Here, the tensile modulus of the material is reduced as the interfaces between matrix and filler debond; thereby not allowing stress to be transferred in the fraction of material around each debonding side. This simple model provides a reasonable first estimate to be made of the nonlinear and irreversible stress-strain profile of a particulate composite such as a PBX, and is described in the section on particulate composites.

Equation of State

Molecular modelling can be an effective method to generate physically-based equations of state to complement experimental methods that are difficult, relatively expensive and time-consuming. Although techniques such as molecular mechanics and dynamics with a well-validated force field can give good predictions of PVT properties for a wide range of organic materials [1], these techniques require specialised computer simulations, and reliability of predictions below pressures of about 1 GPa can be poor.

Since molecular dynamics methods use empirical expressions to quantify the forces and energy between atoms, we simplified these 'forcefields' to the most basic level of interactions between characteristic groups of atoms on adjacent polymer chains. Since all the ensemble-average energy parameters associated with these groups of atoms can be described quantitatively using models from polymer physics, we were able to develop so-called mean-field methods to provide analytical expressions to predict thermal and mechanical properties of polymers both quickly and within experimental variability [2,3].

For polymers and many organic materials, their response to mechanical deformation is determined largely by the weak van der Waal's forces between groups of atoms normal to the chemically-bonded polymer chain axis. Such forces can be represented reliably by a simple 6-12 Lennard-Jones equation for energy as a function of separation distance between chains, r . To a good first approximation, the stiffness in the chain axis is large enough for volume, V , to be proportional to r^2 ; such that the potential energy well of group interactions, E , with a depth equivalent to the zero-point cohesive binding energy, E_{coh} , at the volume V_0 can be written

$$E = E_{\text{coh}} \left(\left(\frac{V_0}{V} \right)^6 - 2 \left(\frac{V_0}{V} \right)^3 \right) \quad (1)$$

Pressure, P , is calculated as a function of volume using the differential

$$P = \frac{dE}{dV} = \frac{6 E_T}{V_T} \left(\left(\frac{V_T}{V} \right)^4 - \left(\frac{V_T}{V} \right)^7 \right) \quad (2)$$

where subscript T is used to denote property values at temperature T. The model parameters for these equations for any polymer can be calculated very simply by means of either group contribution tables or connectivity indices, and are described in detail elsewhere [2,3].

High pressures associated with Hugoniot equations of state mean that we also need to take account of the smaller volumetric strain due to the shrinkage in the relatively stiff chain axis, which has an modulus of the order $Y_p \approx 240$ GPa in a poly(ethylene) structure, for example. As a good first approximation, we find that the shrinkage in the two axes can be simply added. The chain axis modulus is suggested to have a volume dependence due to reduced normal cross-sectional area, which simultaneously increases modulus and reduces force at a given pressure.

$$Y_p \rightarrow Y_p \left(\frac{V_0}{V} \right)^2 \quad (3)$$

The special case of PTFE needs to be noted, since the bulky fluorine atoms effectively increase the value of Y_p in compression so much that shrinkage in the chain axis is very small. Another anomaly due to chain axis deformation has been

noted previously, where phenyl rings in polymers such as poly(styrene) and poly(carbonate) collapse at a compressive stress of about 20 GPa, to give a stepwise reduction in volume and shifts in U_s - U_p plots [1].

The particle and shock velocities are calculated by the usual expressions

$$U_p = \sqrt{\frac{P(1-V/V_T)}{\rho_T}} \quad U_s = \sqrt{\frac{P}{(1-V/V_T)\rho_T}} \quad (4)$$

Figure 1 shows a number of examples of model predictions for a number of common polymers. Generally, model predictions (lines) are seen to be in excellent agreement with experimental data (points). Figure 2 makes the same comparison for a model PBX material and its components, where the combination of the two materials as a composite is calculated using a cohesive energy density (E_T/V_T) in equation (2) for pressure that is simply the average value of the two separate materials.

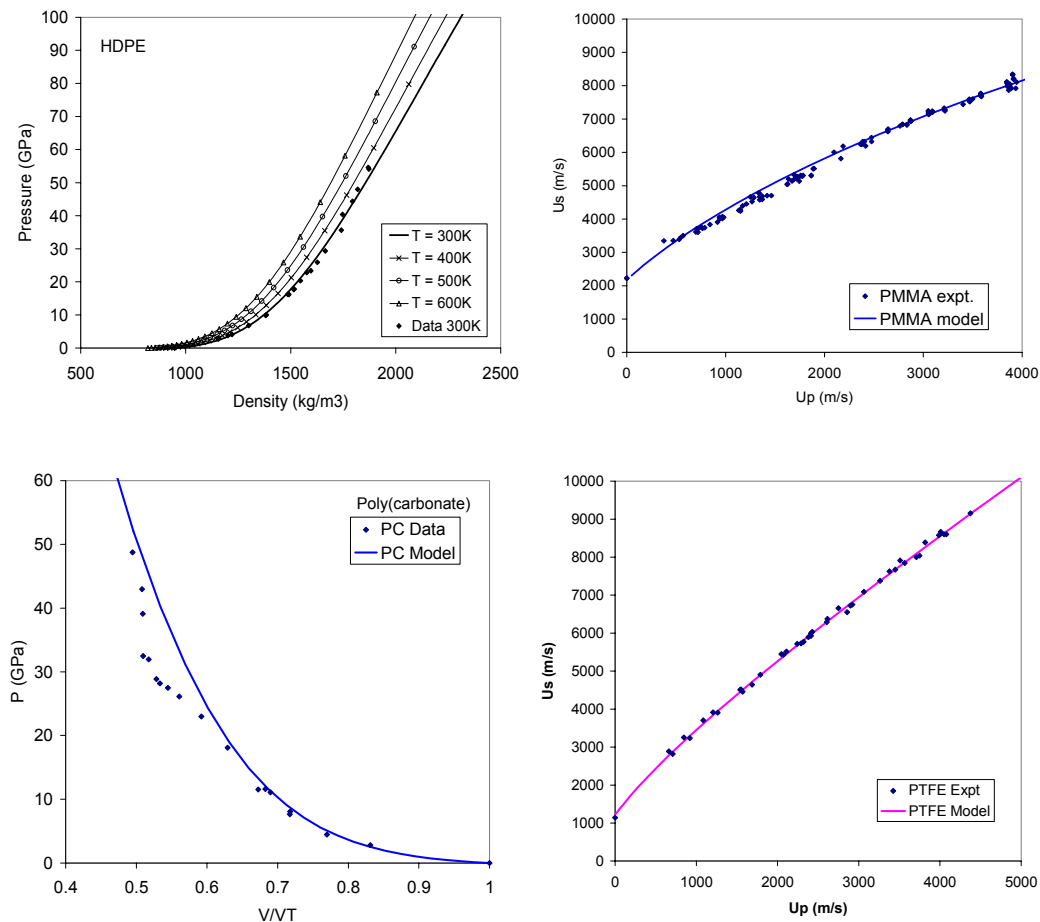


Figure 1. Comparison of EOS model predictions with observation for a number of common polymers as labelled.

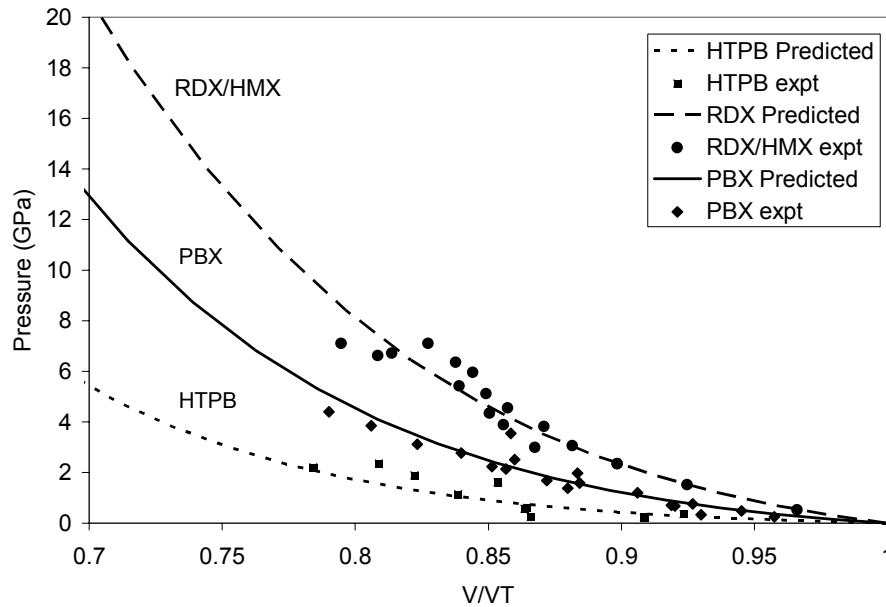


Figure 2. Model predictions of pressure-volume relations for a model PBX and its components compared with observation.

Rate Dependent Constitutive Relation for Polymers

The elastic modulus associated with shock events is assumed here to be unrelaxed bulk modulus, B , at very high rates of deformation, where the atoms and molecules have no time to redistribute themselves in the duration of the shock event and thereby do not dissipate any significant amounts of energy. GIM uses this ideal volumetric elastic modulus as the starting point for calculating the full mechanical property profile of a material. In particular, we are interested here in the tensile or Young's modulus, Y , of a polymer as a function of rate and temperature. We give a brief outline of the model approach here to illustrate the general principles, and details will be published elsewhere.

The physical mechanism used to model Y is that molecules undergoing uniaxial deformation redistribute themselves much more than during simple isotropic bulk compression. This redistribution of molecules causes mechanical energy to be dissipated as heat by a thermo-mechanical coupling process that can be quantified by calculating the change in heat capacity that is induced by mechanical loading by changing the Debye reference temperature of the material [3]. Since mechanical energy is lost, the effective elastic modulus of the material reduces relative to the ideal value of B . The energy dissipation process is described by the parameter of loss tangent, $\tan\delta$, which is roughly the ratio of energy dissipated to energy stored in a deformation cycle.

Figure 3 shows in schematic form the relationship between Y and B via the loss tangent as a function of temperature for a very general semi-crystalline polymer. As the area under the loss tangent curve increases, $\int \tan\delta dT$, the value of Y reduces relative to B . The greatest changes in Y occur at the transition temperatures denoted by T_α and T_β in Figure 3, which are the glass transition and beta relaxation temperatures respectively.

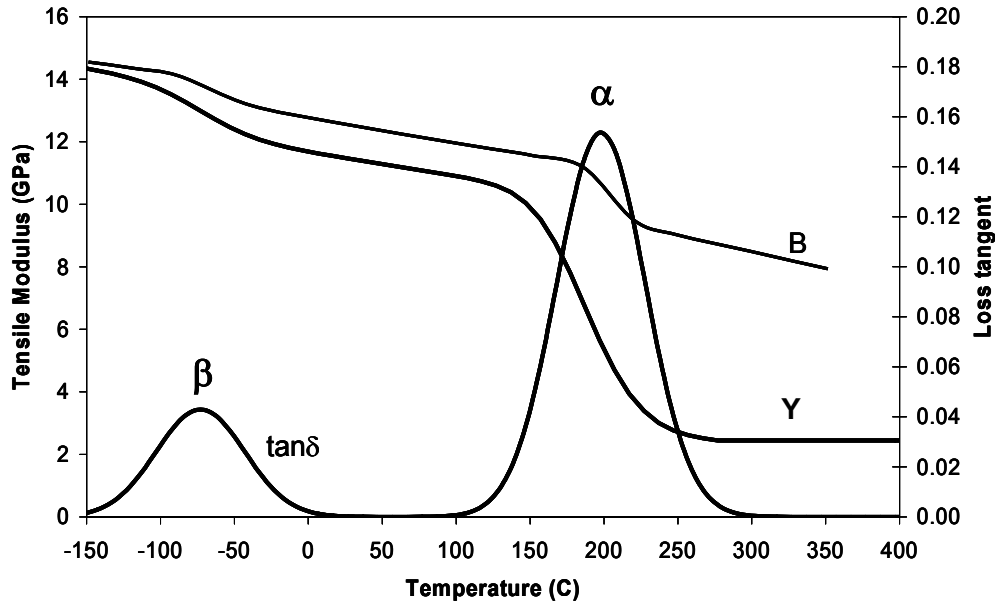


Figure 3. Schematic picture of the relationship between Y and B through the loss tangent as a function of temperature for a general semicrystalline polymer.

Below the glass transition temperature, Y and B are generally of the same order of magnitude of GPa, with values of Poisson's Ratio in the range 0.35 to 0.43 for the most brittle to most ductile polymers respectively. Here, we can use the relation [5]

$$Y = B \exp\left(-\frac{\int \tan\delta \, dT}{A B}\right) \quad (5)$$

where A is structural parameter related to the size of the polymer groups and has a magnitude $A \approx 1.2 \text{ GPa}^{-1}$. We can quantify the integrated loss tangent through the transition temperatures by calculating the total energy dissipated by the respective changes in the number of degrees of freedom and distributing this with a Normal distribution function around the mean transition temperature.

Through the glass transition, the change in modulus is so great that we need to use a special relation for the rubberlike modulus, Y_r (of the order MPa), in terms of the area under the loss tangent curve at T_g , $\tan\Delta_g$, and the tensile modulus just below T_g , Y_g

$$Y_r = \frac{Y_g}{(1 + \tan\Delta_g)^2} \quad (6)$$

Although equations (5) and (6) for tensile modulus might look quite abstract, they are based on a very straightforward principle of energy dissipation reducing elastic modulus and can be quantified relatively simply in terms of the polymer structure; since both B and $\tan\delta$ can be predicted by GIM relations. The great advantage of these equations for modelling the effect of rate is that we can predict the rate (or more specifically, frequency) dependence of the temperature of the relaxation peaks. Both peak temperatures increase with rate, and the beta peak increases faster than the glass transition peak.

Mulliken and Boyce showed empirically that the shift of relaxation temperatures with rate can be used to model the rate dependence of modulus in the way described above [4]; since the effect of energy dissipation reduces with increasing peak temperature, so Y reduces less at higher rates.

The dynamic mechanical modulus-temperature profile shown in Figure 3 can be transformed directly into stress-strain relations by using thermal expansion through a hypothetical temperature change to predict stress and strain

$$\varepsilon = \int_{T_0}^T \beta \, dT \quad \sigma = \int_{T_0}^T \beta Y \, dT \quad (7)$$

where β is the linear coefficient of thermal expansion, that can be predicted using GIM. The most important effect here is the yield point, which corresponds directly to the glass transition temperature, such that the yield strain corresponds to the thermal expansion between ambient temperature and T_g . Since T_g increase with rate, the yield stress and strain must increase with increasing rate. Figure 4 shows predictions for the compressive yield stress of PMMA compared to observation, and the agreement is seen to be quite good.

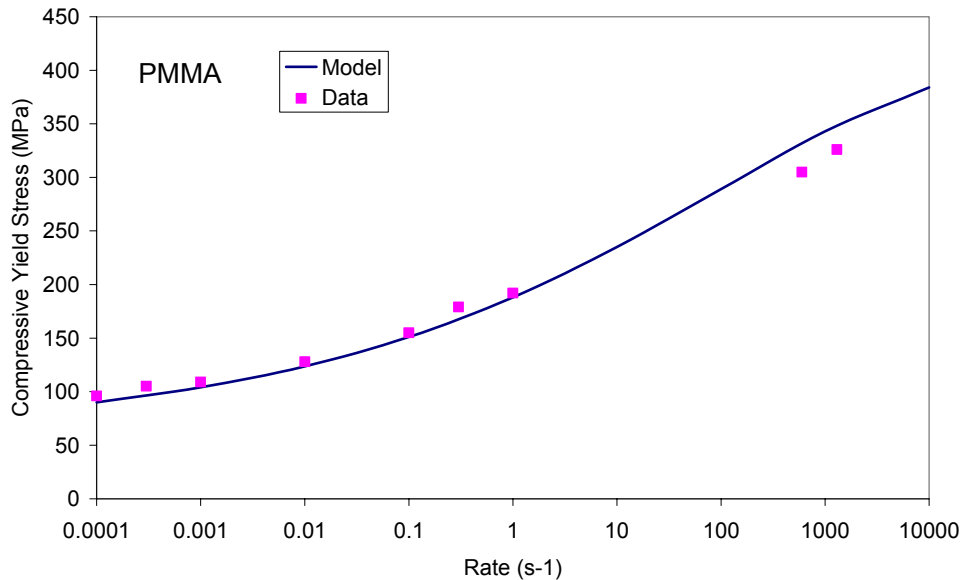


Figure 4. Comparison of predictions (line) and experimental data (points) for the compressive yield stress of PMMA [4].

Rubberlike Binders for PBXs

The very general relations for the rate and temperature dependence of polymer constitutive relations discussed above need to be refined more specifically for the case of binders for PBXs. Binders such as HTPB are generally rubberlike, with elastic modulus values often far lower than 1MPa, since they operate at temperatures far above their nominal glass transition temperature and are often modified by a significant (> 30%) plasticiser. The effect of plasticiser is to reduce the elastic modulus of the binder and this effect is quantitatively embodied in equation (6), since $\tan\Delta_g$ increases in an inverse dependence on the concentration of the elastically-active polymer in the binder.

The structure of a typical HTPB binder and DOS plasticiser are shown below, and Figure 5 shows as points the modulus vs temperature profile of a binder with about 30% plasticiser from DMA measurements at a frequency of about 1 Hz. Also shown in Figure 5, as a line, is the model prediction for the detailed modulus-temperature profile of the same binder, noting that all of the different possible interactions between sub-groups in the HTPB and DOS structures must be taken into account in the model calculation. The model looks reasonable, bearing in mind that the experimental values of modulus should be of the order GPa at low temperatures below T_g , which does suggest some calibration issues with the experimental data.

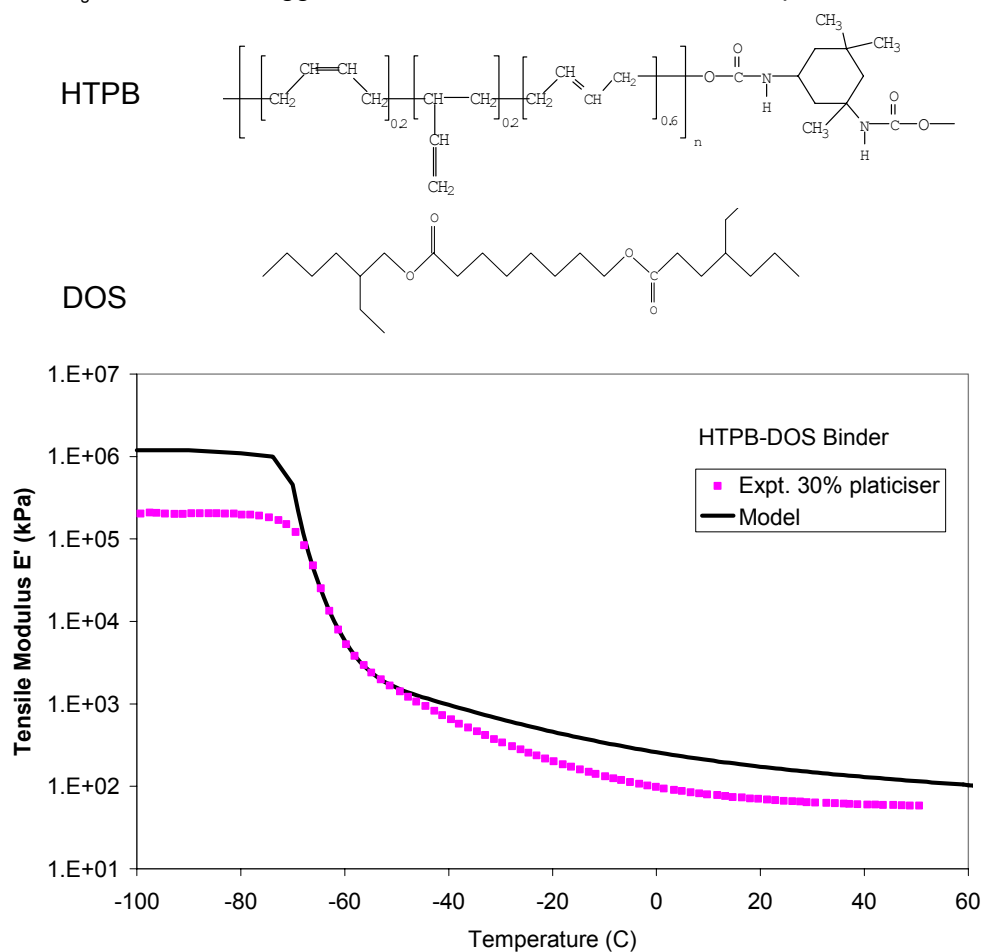


Figure 5. Modulus vs temperature plot for a typical plasticised HTPB binder.

Particulate Composites

While working on a composite model for the stress-strain relationship in concrete, we were able to relate the elastic modulus of the material to the damage caused by debonding of the cement matrix from the particulate filler of sand or aggregate. To do this, we simply said that the modulus, M , should reduce linearly with the fraction of the concrete which is rendered elastically-inactive by the loss of stress transfer between matrix and filler, f_a . To a good first approximation, for low levels of debonding damage, we suggested that the damaged fraction could be quantified by an Arrhenius activation function in the strain energy density relative to an activation energy. Since elastic energy density is proportional to strain squared, we suggest a relation in terms of the initial elastic modulus M_0 and an activation strain, ε_a , which is equivalent to an activation energy, around which debonding starts to develop.

$$M = M_0 (1 - f_a) = M_0 \left(1 - \exp \left(- \left(\frac{\varepsilon_a}{\varepsilon} \right)^2 \right) \right) \quad (8)$$

Figure 6 shows a schematic plot of equation (8) in the form of a simplified stress-strain plot, with the model parameters of M_0 and ε_a having a value of one.

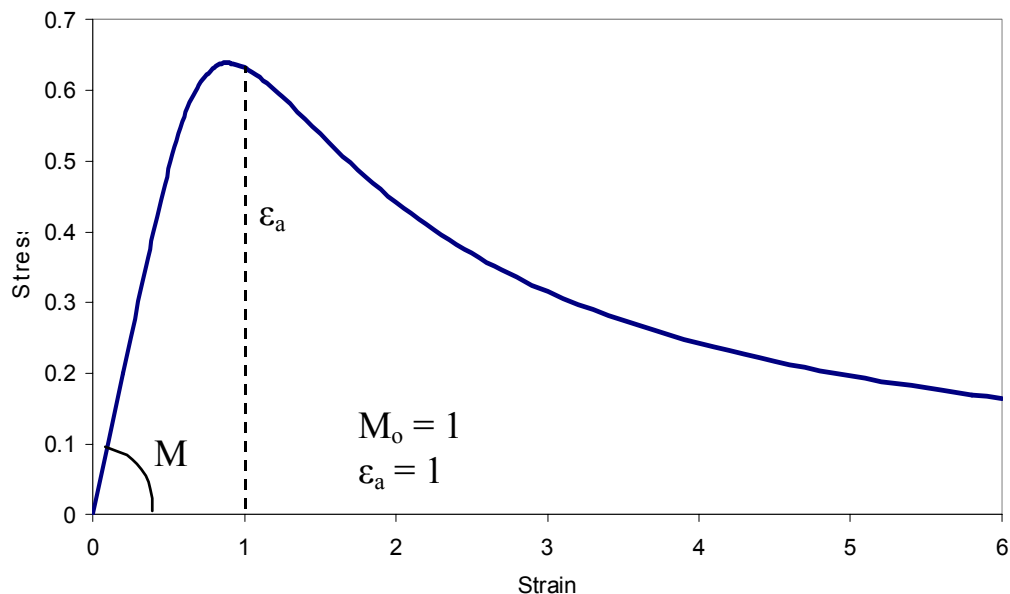


Figure 6. Schematic plot of the constitutive model.

The model has the great advantage of needing only two parameters. The initial modulus, M_0 , can be calculated for the composite using additivity rules for the fraction of fraction of binder in the composite, or can simply be taken as an empirical value from experimental data at low strains. The activation strain for the composite, ε_a , is calculated using a relation derived from the energy required to create free surface area at the particle-binder interface. If the interparticle distance is d , the binder modulus is M_b , and the binding energy per unit interface area is Γ

$$\varepsilon_a \approx A \sqrt{\frac{12\Gamma}{dM_b}} \quad (9)$$

where A is a scaling factor for the applied strain on the composite to the local strain in the binder. For example, for a composite with 20% binder by volume, the fraction of binder in any linear axis is only 8%; so $A \approx 0.08$. Similarly, the distance parameter d can be estimated from the particle size and the volume fraction, bearing in mind that larger distances require a smaller strain or stress loading to fail, due to the greater elastic energy in the larger volume to generate interfacial debonding; so d must be weighted to the distance between larger particles in the size distribution, rather than the smaller particles. This may be further complicated, in that the binder between larger particles may itself be made up of a sub-composite of smaller particles in binder, which is the case in concrete, where the binder between larger aggregate particles is a composite of small sand particles in cement; this will also affect the value of the active binder modulus M_b in equation (9). For many polymeric binder systems, the binding energy takes a relatively constant value of $\Gamma \approx 0.15 \text{ Jm}^{-2}$.

PBX Constitutive Model

To illustrate the model, let us start with a relatively simple model propellant, with a 20% volume fraction of plasticised HTPB binder discussed above with a modulus $M_b \approx 0.3 \text{ MPa}$. The energetic particulate fraction is dominated on a number average basis by particles of about $7.5 \mu\text{m}$, such that the distance parameter $d \approx 0.6 \mu\text{m}$. This suggests an activation strain of $\varepsilon_a \approx 0.24$ for the composite, using equation (9). The initial composite modulus is estimated from the binder modulus and the fraction of binder in a linear axis to be $M_o \approx 0.3/0.08 \approx 4 \text{ MPa}$.

Figure 7 plots the model predictions of equation (8) against experimental observation in the form of a stress-strain plot for the model propellant, and we see that the general form of the damage-induced reduction of modulus due to the activated debonding process are reproduced quite well up to the point where larger-scale fracture events lead to catastrophic failure of the sample.

PBXs are usually more complex than the simple propellant example, and some care is needed in determining model parameters. For example, particle size distribution of energetic material in the binder can lead to unusual effects on the composite modulus due to small particles in the binder becoming effectively a new matrix phase in its own right. Figure 8 shows a stress-strain plot for a model PBX with about 21% HTPB binder by volume and a bimodal particle size distribution. A detailed calculation of the composite tensile modulus easily reproduces the composite modulus of about 11 MPa, with about 50% of the energetic materials being smaller particles that make an effective matrix with a modulus of about 2.5 MPa within the larger particles. However, the activation strain of 0.1 is still determined by the HTPB binder with a modulus 0.3 MPa with the interparticle distance of about $4 \mu\text{m}$ that is appropriate for the average particle size of about $50 \mu\text{m}$. Again the general form of the constitutive model is reasonable, even if the calculation of model parameters from the PBX composition is less than straightforward.

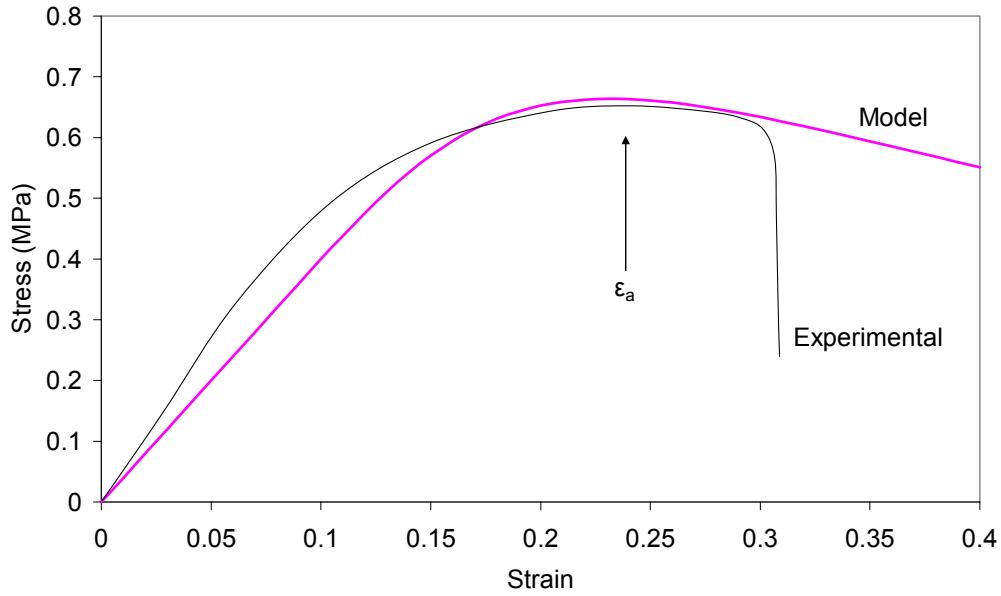


Figure 7. Comparison of predictions of equation (8) with experimental observation for the model propellant composite.

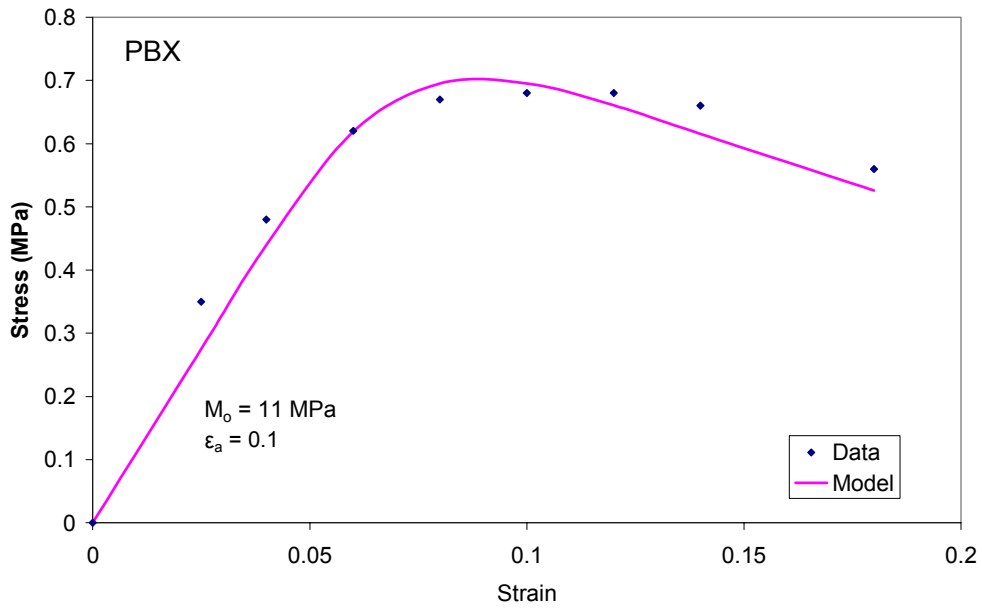


Figure 8. Comparison of predictions of equation (8) with experimental observation for a model PBX.

Summary

We have presented a brief outline of the development of EOS and constitutive models for PBXs and polymers in our work on a number of different projects for MoD over the past 5 years. These models represent a clear departure from previous models, which generally try to reproduce experimental data in a series of empirical relations for input into hydrocodes, for example. The most significant advantages of the models discussed here are:

- Mechanical properties can be quantified directly from the chemical composition and hierarchical structure of the materials.
- All properties are inter-related; for example, the tensile modulus in a constitutive relation is calculated directly from the EOS bulk modulus. All properties are thereby self-consistent for any material.
- Thermal properties are an integral part of the model and energy exchanges due to mechanical deformation (elastic or lossy) can all be converted into temperature changes for subsequent energetic calculations.

The single most pressing problem in this work is to develop a strategy for intermediate to high-rate constitutive relations for complex binders in PBXs. Current models do not accurately predict the modulus-temperature-rate relations for highly plasticised binders and PBXs at higher rates $> 10^3 \text{ s}^{-1}$; such as those in Hopkinson bar experiments. This problem is probably more a matter of not yet understanding the physics of deformation under these conditions, rather than the inability of the model framework to cope with these complex events. For example, factors such as the criteria for onset of shock conditions in different parts of a material may play an important role.

References

- [1] D. Porter and P. Gould, *J. Phys. IV France*, **110** (2003) 809-814.
- [2] D. Porter and P. Gould, A general equation of state for polymeric materials, *J. Phys. IV France*, **134** (2006) 373-378.
- [3] D. Porter. Group Interaction Modelling of Polymer Properties, Marcel Dekker, New York (1995).
- [4] A.D. Mulliken and M.C. Boyce, *International Journal of Solids and Structures*, **43** (2006), 1331-1356.
- [5] D. Porter, F. Vollrath, Z. Shao, *Eur. Phys. J. E*, **16** (2005), 199-206.

Acknowledgements

This work was carried out as part of the Weapons and Platform Effectors Domain of the MoD Research Programme.

We would also like to thank Ian Cullis, Phillip Church, and Rory Cornish for their help and support during this work.

Analysis at the mesoscale of the response of the propellant under dynamic loading : numerical and mechanical modelisations issues.

A.Fanget¹, G. Contesse¹, A.Dragon², C. Nadot-Martin², S. Dartois², M. Touboul²

¹ Centre d'Etudes de Gramat, 46500 France

² Laboratoire de Mécanique et Physique des Matériaux (LMPM), ENSMA, Téléport2/1, Av. C. Ader, F-89961 Futuroscope, Chasseneuil, France

Key words : X-ray microtomography, homogenisation, granular media, numerical simulation.

Abstract.

The understanding of the response of a propellant, specifically under dynamic loading needs, as many author claim, to know its mesostructural morphology and the mechanical behaviour of each of its components. But the scale of the mechanical description of the behaviour of a propellant is relative to its heterogeneities and the wavelength of loading. The shorter it is, the more important the topological description of the material is. In our problems, involving the safety of energetic materials, the propellant can be submitted to a large spectrum of loadings. In this paper, an analysis is first presented which gives the domain in terms of stress and strain involved. It shows that we have to describe the behaviour of the material from mesoscale to macroscale. Mesoscale response requires the direct description of the morphology of the sample, whereas macroscale response embedding local information can be obtained from homogenisation techniques. Following this analysis, we show how we built from microtomography data the mesoscopic description of the sample and the equivalent schematisation of Christoffersen which is the support of the homogenisation. Then we present the frame and the results obtained in the homogenisation processes for hyperelasticity and damage approach. Experimental studies in static and dynamic loading are described which allow extraction of coefficients for constitutive law and to realised a first qualitative analysis on physical phenomena appearing after loading. Finally, numerical simulations at the mesoscopic level are shown to justify the homogenised approach and the problems appearing.

I. Introduction.

Understanding the response and modelising the behaviour of energetic materials, such as plastic bonded propellants (P.A), is of concern to determine their threshold of safety to moderate strain rate loading. The physical processes involved in this range of loading are numerous [1], complex and interdependent. One of the reasons is the complex response of such composite material, consisting of particle energetic crystal bound in an inert polymer binder phase that we can call the first structural level (mesoscale). An other problem is that the safety problem involved massive quantities of substance, which constitutes a second structural level that we call macroscopic level. As simulation of the global mechanical response of a block of propellant at the mesoscale level is impossible, we extracted local physical information through an homogenisation process. In chapter 1, we show on a simple example of impact that we can decompose the mechanical processes in three classes. One where we need the discretisation at the mesoscale, another for which an homogenised approach may be used and the last where classical macroscopic description is sufficient. For the mesoscale description we extract

morphological information from microtomography and image analysis. This is the object of chapter 2. Chapter 3 deals with the work performed about the homogenisation process to get mechanical description of the behaviour in the frames of hyperelasticity and damage. This homogenisation based on a schematisation of the microstructure in the sense of Christoffersen is recalled with the hypothesis involved. Chapter 4, some experimental static and dynamic results are shown. In chapter 5, numerical simulations of a mesoscopic volume are presented for different loadings. The aim of this paper is to show briefly the new results obtained in the different ways we have defined in the past [2].

II. Domains of investigation :

The configuration test is the classic impact of a small steel sphere (simulating a fragment) on a sandwich composed of a block of propellant embedded between a front aluminium and rear steel plates. The thickness of the plates are 1.5 mm, 25 mm and 15 mm respectively for aluminium, the propellant and the steel their diameters are identical equal to 80 mm. The initial velocity of the sphere of 10 mm diameter is 100 m/s. Figure 1a shows the configuration of impact and figure 1b shows the six loci from which the numerical information is extracted. The behaviour laws used are elastoplastic type for aluminium and steel, and viscoelastic type for the propellant. The simulation is realised through an explicit scheme.

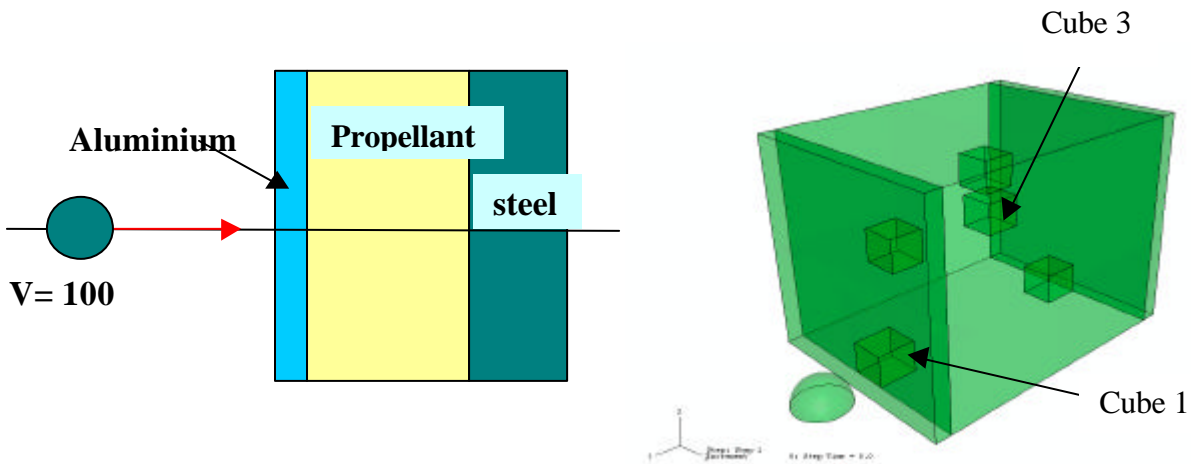


Figure 1 : a : Initial configuration b : Loci of numerical analysis

The loci for numerical analysis are constituted of six cubes of 2.6 mm size. This size is chosen because in this volume there is at least 694 grains of P.A of 400 μm which must be close to the Statistical Elementary Volume (SEV). Figure 2 shows for cubes 1 and 3 respectively the deformation and the III invariant of the stress. Cube 1, close to the impact locus has very large deformations (>40%), as we will see in a simple experimental test. At this level of loading the material response may be only describe at the mesoscopic scale. The mechanical response of the other cubes are closed one of the others and are submitted to compression and tension of which the min and max values are in the range [- 1.e8 Pa, 1. e8 Pa].

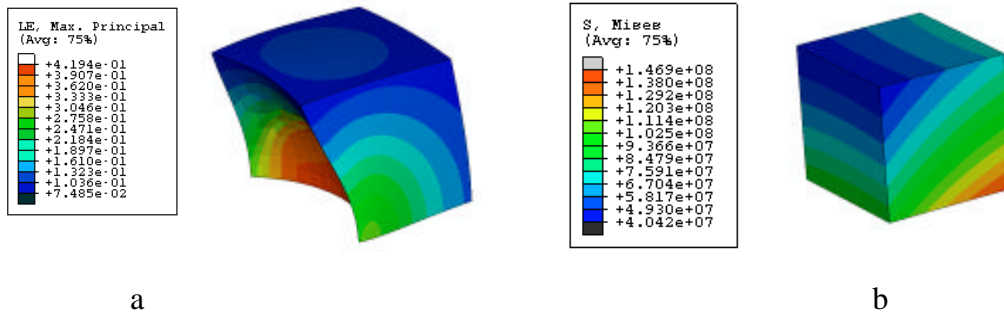


Figure 2: a : cube 1 b : cube 3

III. Microtomography acquisitions.

To describe the mechanical behaviour at mesoscale we need to know the morphology of the sample at this scale. To do that an X-ray microtomography system has been used which allows the acquisition of images. The microtomographic apparatus used to perform the acquisition of morphologic structure of the sample is a Skyscan microtomograph of 100kV. The sample, of which the maximal dimensions are 20 mm diameter and 40 mm of height, is set on a console-table in rotation. The X-ray source is fixed and a CCD camera records the images (generally 782 by test). The figures 1a and 1b recall the performances of it.

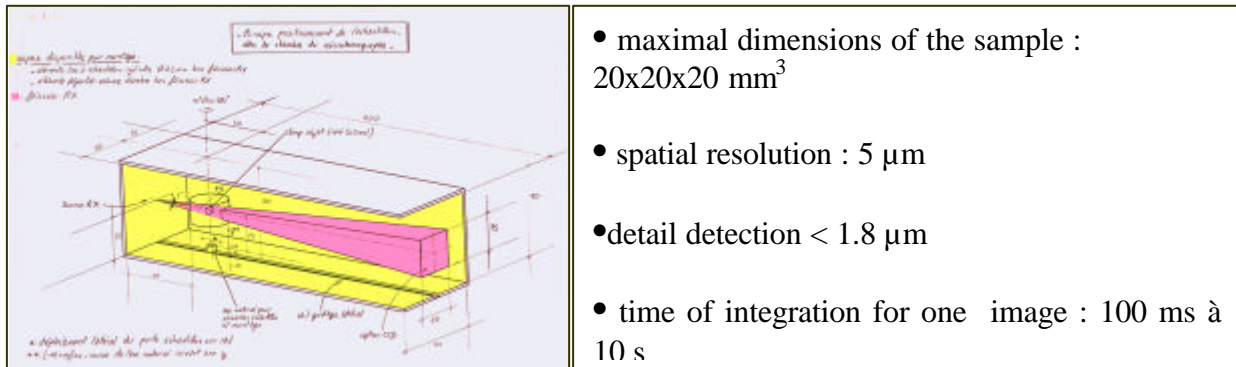


Figure 3: Principle and characteristics of acquisition

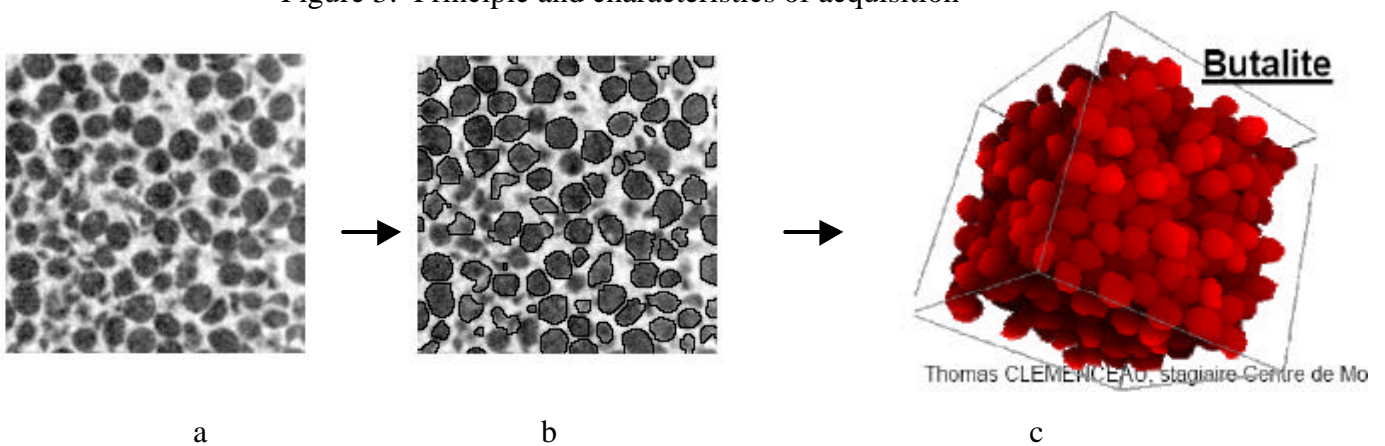


Figure 4 : a . Acquisition ; b. segmentation ; c. binarisation

Once the acquisition is performed, a sequence of filtration, threshold value, segmentation and binarisation is applied as it is schematised in figure 4. The 3D reconstruction of the sample with the grains and the binder has been performed through an application developed by LSI and CEG [3].

From a statistical analysis of the morphology of the X-ray investigation a lot of informations may be obtained, such granulometry spectrum, anisotropy, euclidean distance between elements and so on. In our example, we show granulometry spectrum and anisotropy in figure 3. A fully three-dimensional characterisation of the material microstructure has been obtained on a propellant composed of PBHT (43%) and P.A (400 μm). The resolution of this acquisition is 8 μm . On the figure 2 c 3D image shows a cube of a 2.6 mm size of this material containing 800 grains. The anisotropy is defined from the notion of covariance, that is the correlation of an image with itself. A perfect anisotropy will show a disc form around the peak of covariance, which is close to being the case here.

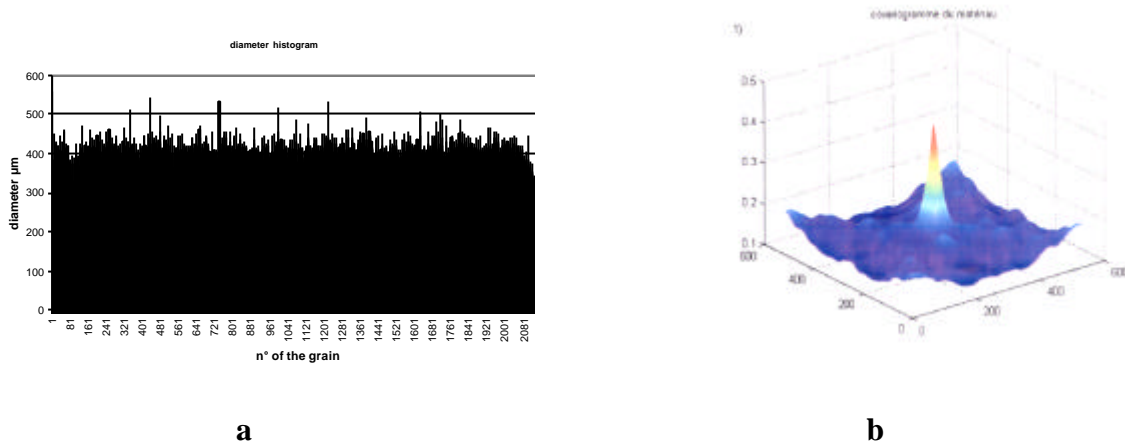


Figure 5 : a . Spectrum granulometry b. anisotropy diagram

IV. Homogenisation processes

The approaches start with a geometrical schematisation of initial random microstructure of the material considered. In the initial configuration, the grains of a highly filled particulate composite are represented by polyhedra; the matrix phase is discretized by an assembly of thin layers with constant thicknesses separating the polyhedral grains. This schematisation illustrated in “morphological parameters” is defined in the non-deformed configuration:

- h^a , the constant thickness of layer a
- A^a , the projected area of layer a ; the associated volume is then $A^a h^a$
- \mathbf{d}^α , the vector linking the centroids of the two polyhedra (grains) separated by layer a
- \mathbf{n}^α , the unit vector normal to the plane interface grain/layer a .

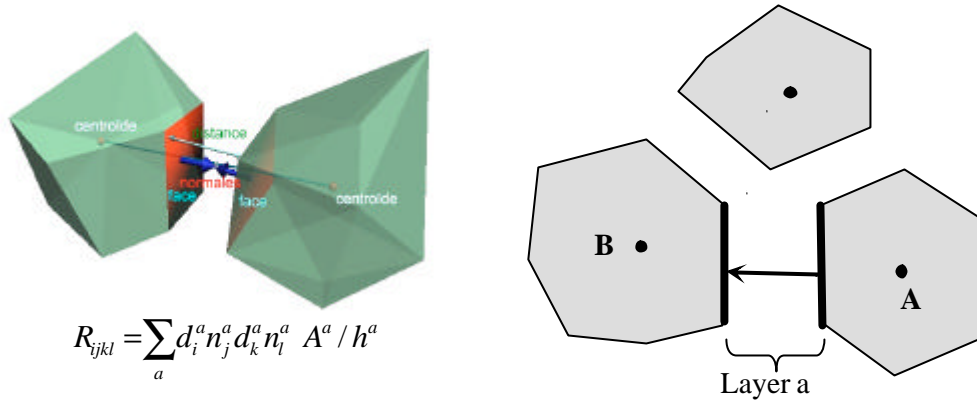


FIG. 6 : Microstructure geometrical schematization by Christoffersen

Once the grains are replaced by polyhedra (satisfying the condition of parallelism between the interfaces of opposite grains), the parameters \mathbf{d}^α , \mathbf{n}^α and h^α are readily determined. For a random microstructure, the projected area A^a —leading to the definition of the matrix zone between neighboring grains called “layer a”— may be determined as follows. Starting from the centroids of the two grains considered, the two opposite interfaces are projected on the middle plane of the intergranular zone. Then, an average projection is defined and chosen as the area A^a . In this way, layer a (associated volume $A^a h^a$) does not correspond exactly to the matrix zone strictly confined between the two opposite interfaces.

Even if such a geometrical schematization (polyhedral grains, parallelism of opposite interfaces) is an approximation of the particulate microstructure, salient information concerning real morphology is nevertheless accounted for in the approach considered. In the original paper of Christoffersen [4], dependency of estimates on possible texture of the composite considered, on grain shapes’ irregularities and on layers’ thickness is demonstrated; in finite strain, this is obviously preserved. From a practical point of view, the challenge is to optimize the correspondence of the “true” microstructure with the Christoffersen-schematized one in order to confer a fair relevance on the morphological parameters involved in the estimates.

The second step of the approach is the formulation of simplifying kinematical assumptions concerning the local fields in the schematized volume. They are recalled below and are the direct generalization to finite strain of the Christoffersen’s original kinematical hypotheses:

- the deformation gradient in the grains, noted \mathbf{f}^0 , is supposed to equal the macroscopic deformation gradient \mathbf{F} at the centroids of the grains; \mathbf{F} is considered as the data of the localization-homogenization problem.
- \mathbf{f}^0 is assumed to be homogeneous and identical for all the grains;
- the deformation gradient in a layer a, noted \mathbf{f}^α , is supposed to be homogeneous in that layer, but it can vary from one layer to another;
- local disturbances at grain edges and corners are neglected on basis of thinness of the layers.

IV.1 Local problem approach

IV.1.1 Finite deformations.

In this schematised context, the deformation gradient \mathbf{f}^α of any layer can be expressed as a function of the morphological parameters of the layer :

$$f_{ij}^\alpha = f_{ij}^0 + \left(\mathbf{F} - \mathbf{f}^0 \right)_{iK} \frac{d_K^\alpha n_j^\alpha}{h^\alpha}$$

This formulation offers a way to take into account some strain heterogeneity in the matrix phase represented by an assembly of layers. It is coherent with the fact that in non linear homogenisation context it was shown that local heterogeneities must taken into account. On the other hand, the identical deformation gradient f^0 for all grains could be reductive, but we must keep in mind that large part of the total deformation is absorbed by the binder. The compatibility between local motion and the macroscopic one, characterised by the deformation gradient F , is given through the equation :

$$F = \langle f \rangle_{V_0} = (1-c) f^0 + \frac{1}{V_0} \sum_{\alpha} f^{\alpha} A^{\alpha} h^{\alpha} \qquad \frac{1}{V_0} \sum_{\alpha} d_{I n J}^{\alpha} A^{\alpha} = \delta_{IJ}$$

$$(1-c) s_{Ji}^{-0} + \frac{1}{V_0} \sum_{\alpha} s_{Ji}^{-\alpha} A^{\alpha} h^{\alpha} - \frac{1}{V_0} \sum_{\alpha} s_{Ki n K}^{-\alpha} A^{\alpha} d_j^{\alpha} = 0$$

taking into account the compatibility condition, intrinsic of Christoffersen schematisation. Using the Hill-Mandel principle of macro-homogeneity, in the frame work of finite strain in the case of homogeneous stress boundary conditions, lead to solve the equation above:

where s^0 and s^{α} denote the average nominal stress tensors respectively macroscopic and microscopic in the grains and layer α . In this equation are introduced the constitutive law of the matrix and grain phases. So the preceding equation can be solve in f^0 and F , considering that F is a data for the localization-homogenization problem characterizing the loading applied. A numerical procedure is used to solve this non linear equation [5].

IV.1.2 Damage.

It concerns the damage created by the debonding between grain and matrix. This damage is observed under quasi-static loading which may be represent a large part of the loading in securisation of propellant. In the frame of the schematisation of Christoffersen, the mechanical description has been extended to debonding [6]. It means that faces between grain and binder may be separate and by consequence the gradient of deformation f^{α} has for expression :

$$f_{ij}^{\alpha} = f_{ij}^0 + (F_{ik} - f_{ik}^0) d_k^{\alpha} n_j^{\alpha} / h^{\alpha} + f_{ij}^{\alpha D} \quad ; \quad \langle b_i^{\alpha} \rangle_{I_1^{\alpha}} = - \langle b_i^{\alpha} \rangle_{I_2^{\alpha}} = - \frac{1}{2} f_{ij}^{\alpha D} c_j^{\alpha}$$

Where is the mean displacement discontinuity vectors of the interfaces. The supplementary term $f^{\alpha D}$ represents the contribution of the two interfacial defects located at the boundary of the debonded layer α . For linear-elastic and isotropic constituents the expression of f^0 is :

$$f_{ij}^0 = (Id^1 - B^{-1} : A')_{ijkl} F_{lk} - B_{ijuv}^{-1} L_{uvkl}^{(s)'} \left[\frac{1}{|V|} \sum_{\gamma} \Pi_{\gamma}^f \varepsilon_{lk}^{\gamma D} A^{\gamma} h^{\gamma} + \delta_{\gamma\alpha} \frac{1}{|V|} \sum_{\beta} \varepsilon_{lk}^{\beta D} A^{\beta} h^{\beta} \right]$$

$f_{ij}^{0(d)}$

$\varepsilon^{fD} = \text{Sym. } f^{fD} \qquad \varepsilon^{sD} = \text{Sym } f^{sD}$

β and f denote respectively the layers with opening and closed defects

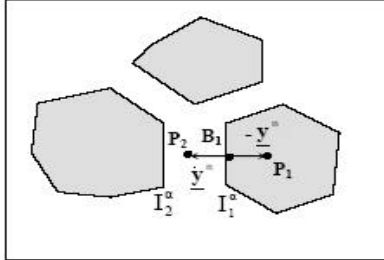
The mechanical modulus A' and B' are the mechanical modulus naturally degraded by two damage tensors:

These tensors emerge via the solution of the local problem, they represent micro mechanical entities about the deterioration mechanism generated within grains/layers aggregate. The non symmetry of D induced a complex anisotropy. They denote the character of local damage and the interaction (the non local effect) of these damages.

$$D_v = \frac{1}{|V|} \sum_p d^n n^p A^p$$

$$\bar{D}_{\text{uni}} = \frac{1}{|V|} \sum_p d^n n^p d^n n^p A^p / h^p$$

At the nucleation of a any pair of defects no continuity condition can be written at micro scale.



$$\Delta u_i = u_i^a(\underline{y}^p) - u_i^o(\underline{y}^p) = \left[2f_{ij}^0 + (F_{ik} - f_{ik}^0) \frac{d_k^n n_j^a}{h^a} \right] y_j^n$$

$$\underline{y}^n = \frac{1}{k} h^a \underline{n}, \quad d_{\text{norm}}^a = \left| \frac{2h^a}{k} + \Delta \underline{u} \underline{n}^a \right| - \frac{2h^a}{k} \quad k > 1$$

The criteria is satisfied when d_{norm}^a is $>$ dcrit

Figure 7 : Definition of the vector y^n

But the Christofersen type approach in the presence of damage allows for access to the analytical expressions of local and strain fields. Indeed, one can extract the increase of the displacement between points belonging respective at the grain and at the binder (see fig 6)[6].

IV.2 Results

IV.2.1 Finite deformations.

For the two phases constituting the material it was choose the compressive Mooney-Rivlin model given by the expression :

$$\omega^{\text{matrix}}(\bar{I}_1, \bar{I}_2, J) = C_{10}(\bar{I}_1 - 3) + C_{01}(\bar{I}_2 - 3) + \frac{K}{2}(J - 1)^2$$

$$\text{with } \bar{I}_1 = I_1 J^{-2/3} = \text{tr}(\mathbf{C}) J^{-2/3}, \bar{I}_2 = I_2 J^{-4/3} = \frac{1}{2} \left((\text{tr}(\mathbf{C}))^2 - \text{tr}(\mathbf{C}^2) \right) J^{-4/3}, J = (\det(\mathbf{C}))^{1/2}$$

C_{10} , C_{01} and K are respectively the Mooney-Rivlin coefficients and the bulk modulus, \mathbf{C} denotes the right Cauchy-Green stretch tensor. The same model is used for the two components with a contrast coefficient of 10. For the matrix, $C_{10} = C_{01} = 0.5$ MPa and $K = 100$ MPa, the poisson ratio is 0.49.

The validation of the homogenisation process for an hyperelasticity description is realised through comparisons between analytical and F.E results. For the sake of minimisation of calculation time, the mesostructure chosen is a periodic one. Three loading past, uniaxial compression deformation, an incompressible tension and a simple shear were tested defined by the deformation gradients:

$$\mathbf{F}^{\text{comp}} = \begin{pmatrix} \lambda & 0 & 0 \\ 0 & 1 & 0 \\ 0 & 0 & 1 \end{pmatrix}, 0.3 \leq \lambda \leq 1; \quad \mathbf{F}^{\text{tens}} = \begin{pmatrix} \kappa & 0 & 0 \\ 0 & 1/\kappa & 0 \\ 0 & 0 & 1 \end{pmatrix}, 0 \leq \kappa \leq 2; \quad \mathbf{F}^{\text{shear}} = \begin{pmatrix} 1 & \beta & 0 \\ 0 & 1 & 0 \\ 0 & 0 & 1 \end{pmatrix}, 0 \leq \beta \leq 0.6$$

If the loading conditions are straight forward for the morphological approach (noted M.A), it is not the case for FE (see [5] for details).

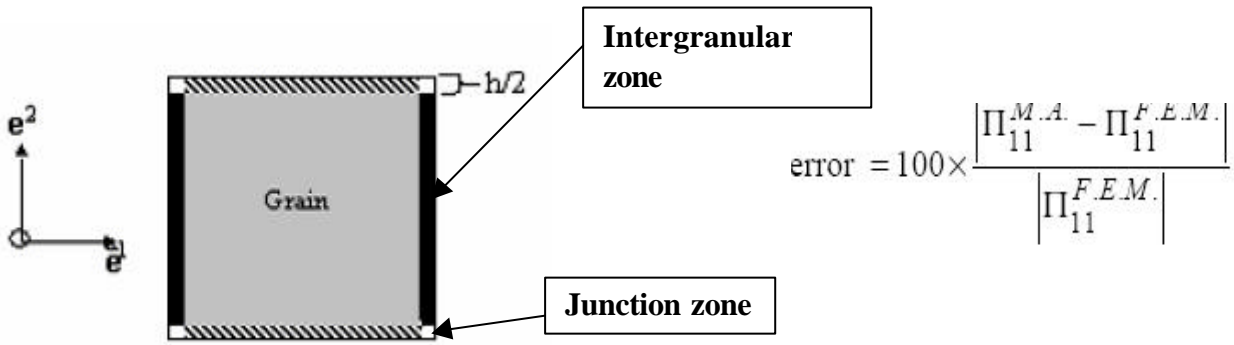


Figure 8: a. Intergranular zone in the F.E. approach, b. Expression of the calculated error.

The results of the first loading are illustrated by the comparison of the first Piola-Kirchhoff stress (component 11 and 22) versus the macroscopic factor λ (for $0.65 < \lambda < .7$) on figure 9a. A good agreement between M.A and F.E.M in all part (an error < 3%) except for the grain facets (“junction” zones) and in an the very close neighbourhood of these zones where the error can rise until 18%.

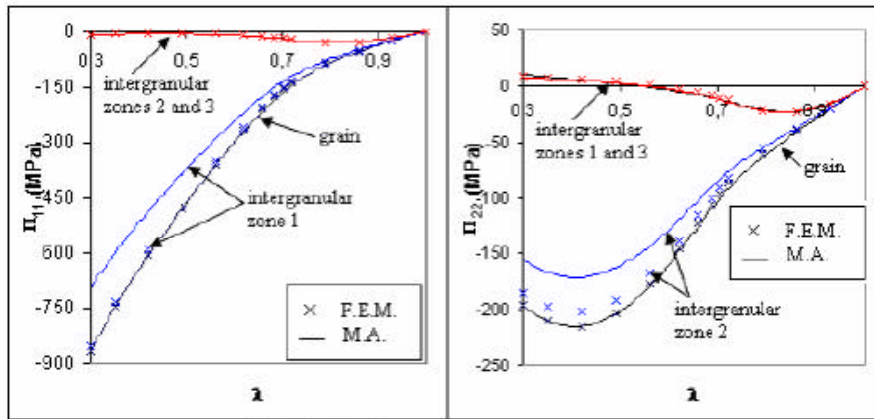
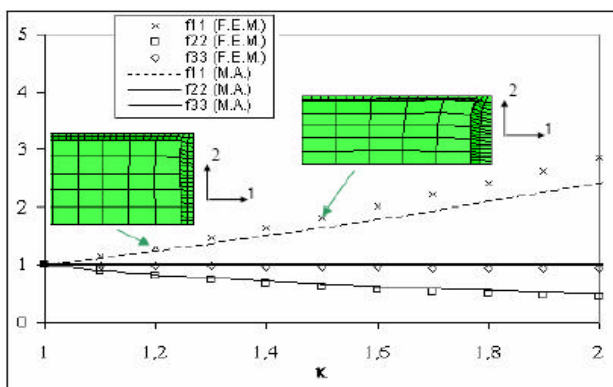


FIG. 9 : Local average first Piola-Kirchhoff stresses for simulated uniaxial compressive deformation: a) in direction 1; b) in direction 2

Same kind of comments about the results for the incompressive tension for which the greatest relative error was 15% at the end of the loading. In this case, the hypothesis of piecewise homogeneity of the local deformation gradient in the matrix is less evident than for the uniaxial loading, nevertheless the M.A provide an acceptable approximation of the average strain in the grain and the intergranular zones. On figure 10, it is showed the comparison between M.A and F.E.M for the average principal stretches in intergranular zone1 versus κ and the distortion of the F.E.M mesh in the junction zone involving discrepancies between M.A and F.E.M.



Average principal stretches in granular zone 1 (M.A and F.E.M) versus κ and associated deformed shape (F.E.M) 2D plane section to simulate incompressive tension.
Figure 10

Lastly, the simple shear loading for a maximum level of $\beta = 0.6$ shows enough good convergence between M.A and F.E.M results (relative error lower than 6%) for all the components in the homogeneous parts of deformation excepts f_{22} and f_{12} respectively in intergranular zones 2 and 3 as it is shown figure 11.

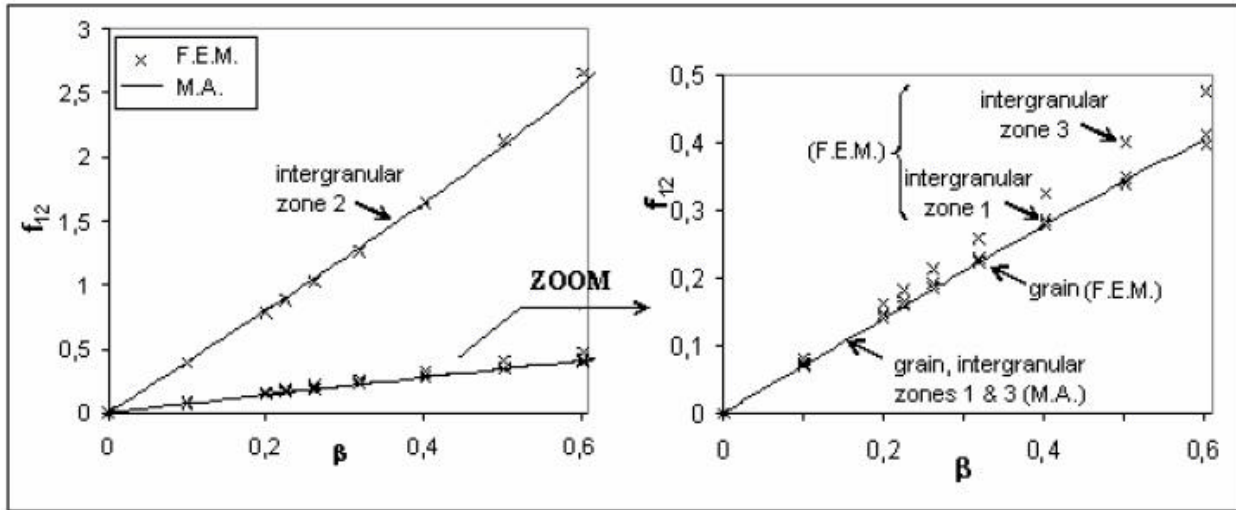


Figure 11 : Average local deformation gradient (component 12) for simulated simple shear

IV.2.2 Damage.

The first homogenised simulation has been performed on an hazardous cubic structure of 400 polyhedron. A loading of 1.25 % longitudinally and .25 % transversally is applied to this cube. At this time, the behaviour of grains and binder are elastic with a contrast between phase of 10 .The result is that 45 faces was debonding on 2213 for this macroscopic loading for a $d_{critical} = 0.50095$ and $\lambda = h/10$.

V. Experimentations

All the experimental tests have been performed with the composition PBHT – P.A 400 μm described previously.

V.1 Static tests.

The behaviour of granular material are dependent of the pressure term, so we have proceeded at triaxial tests to determined this sensibility. The process of the tests consist to bring the medium at the pre-defined pressure and to impose an uniaxial constraint. The tests performed for the pressure of confinement 100 MPa, , 200 MPa, 300 MPa, 400 MPa, 600 MPa. The loading pressure gradients are strictly identical and allow to extract the evolution of the pressure versus the volumic deformation and the bulk modulus. On figure 11 are plotted the evolution of the pressure for the test at 600 MPa with a fit of it. Bulk modulus can be represented through a linear function of e_{kk} and belong to the range [0.458 GPa, 1.26 GPa] for e_{kk} belonging to the range [0., 7%]. The triaxial loadings which reached the longitudinal deformations from 6% to 14 % and transversal deformation from 5% to 9 % have exhibited a volume recompression for the loading pressure of 200, 300 and 400 MPa, the most characteristic was for 400 MPa as it can be see on figure 11.

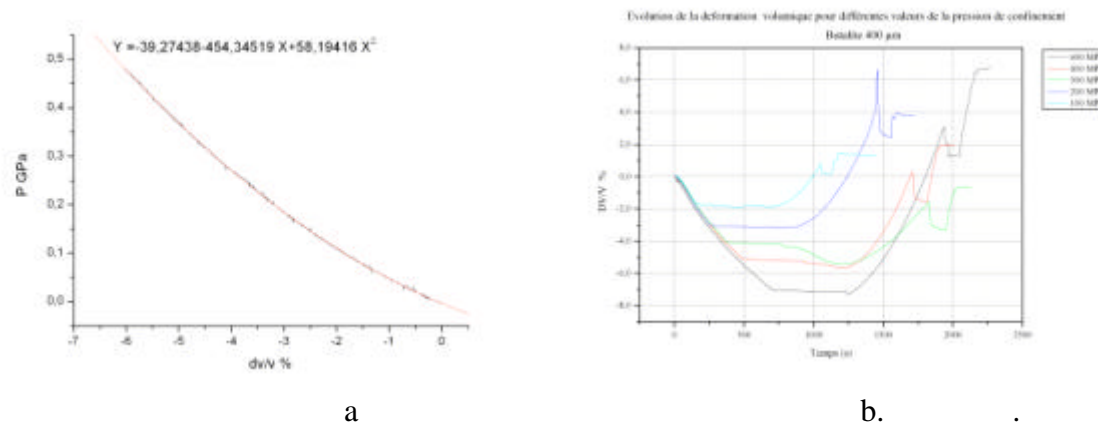


Figure 11 : a. Pressure versus ϵ_{kk} ; b. ϵ_{kk} versus time

The low level of the constraint induced with a signal/ noise low in triaxial configuration allowed us only to extract a Young's modulus for the confinement pressure of 600 MPa. This signal showed on figure12 is saturated at a average of 25 MPa above the confinement pressure and the value of the Young's modulus is 1300 MPa. An other series of tests will be performed to explain why a volumetric compression takes place and to determine at 75 and 90 MPa of confinement the evolution of the Young's modulus.

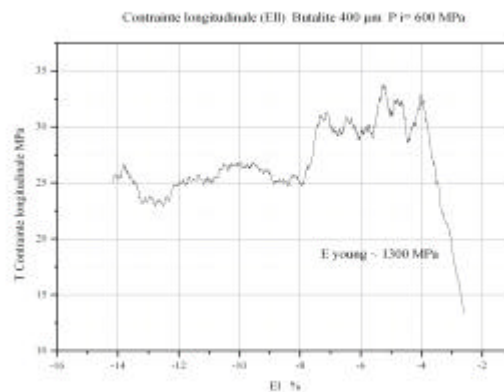


Figure 12 : Longitudinal stress versus longitudinal deformation

To perform numerical simulations at the mesoscopic level, it needs to have some mechanical information about the behaviour of each component. For the binder (PBHT) tests in simple traction have been realised to determine the coefficients of the Mooney-Rivlin law [7] and triaxial hydrostatic compression up to 120 MPa to determine the bulk modulus versus ϵ_{kk} . The values obtained from simple traction tests are:

$$C_{10} = 1,143 \cdot 10^{-2} \text{MPa}, C_{01} = 2,095 \cdot 10^{-2} \text{MPa}$$

Figure 13 shows the evolution of P versus ϵ_{kk} for the binder. On same figure is plotted the previous measured P(ϵ_{kk}) for the butalite. One can see that the rise up of P for the butalite is less than for the binder and it needs to reach $P \sim 400$ MPa or $\epsilon_{kk} \sim 5\%$ to get the intersection of the two curves. Probably it needs to collapse voids (between grain and binder, inside grain) or the density of binder is not the same when it is mixed with grains or not?

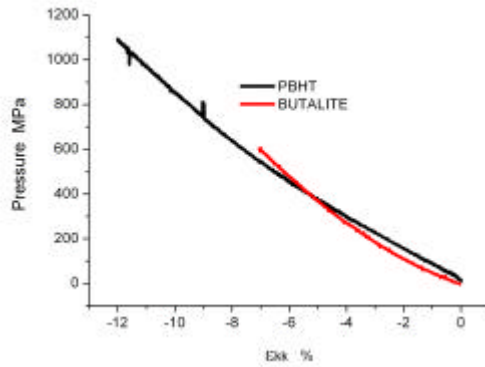


Figure 13: Pressure versus ekk black : PBHT; red : Butalite

The last static tests involved traction tests inside the microtomograph. The aim of these tests is to « feed » the homogenised model with damage. This damage consists in the debonding between the grains and the binder. The principle is simple, a cylinder of butalite of 7 mm in diameter and 10 mm height is introduced in a system (see figure 14) which allows to pull on it by screw a nut. The increment in elongation for a turn is around 0.4 mm. The size of the pixel for these acquisitions were 8 μm. and figure 15 shows the results for one turn.



Figure 14: Pulling system and apparatus in the μtomograph

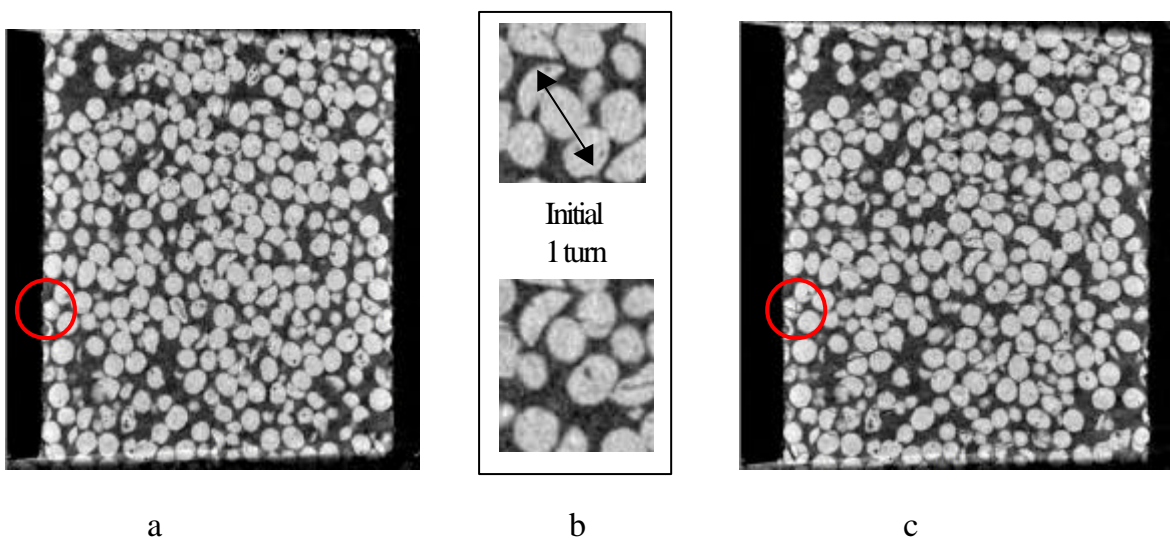


Figure 15 : a Original ; b Comparison ; c after deformation

Until now, the treatment of the images is incomplete to give quantitative values of the intergranular distances and the increase of the porosity. Nevertheless, the macroscopic deformation are $\epsilon_{II} = 5.48 \%$ and $\epsilon_{rr} = 1.73 \%$. On figure 15 b, a zoom on the central middle part of the sample shows the new distances between grains, the norm of the arrow (fig 15b) is respectively 0.96mm for original and 1.01mm for stretch sample. But only a 3D reconstruction can take into account of rotation of the grains. An other difficulty is the note of some of grains fail (red circle). Taking into account the previous remarks, the analysis must be considered the initial porosity of the sample. The test at 1.5 turns has caused a partly rupture of the sample at the level of its bottom after it relaxed during one night.

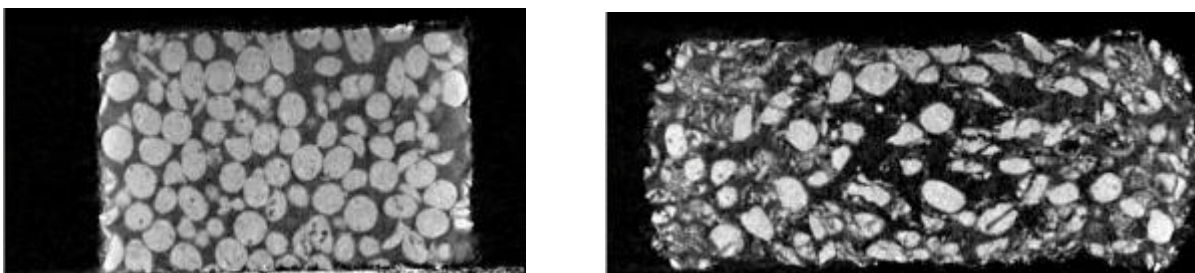
V.2 Dynamic tests

Two preliminary tests at the «mouton de choc » for respectively 5 and 2 kg at 10 cm height have been done. The dimensions of the samples are $\phi = 5 \text{ mm}$ and $h = 3 \text{ mm}$. The morphologic mesoscopic states of the sample before and after loading are presented figures 16 and 17. One can say:

1. For the test at 5 kg the residual macroscopic deformations are 31% in diameter and of 13% in width. The microtomography of the sample after test shows an mesoscopic state in which the major part of the grains have been: extremely distorted, multifissurised (on can tell pulverised for some) and in zones where the grains «disappear ». The multifissuration process is more pronounced on the periphery whereas the «annihilation » process is more central at the sample.
2. For the test at 2 kg kg the residual macroscopic deformations are 21% in diameter and of 9 % in width. The μ microtomography of the sample after test shows a mesoscopic state for which one see a fissuration of the grains when these ones are few «confined » by neighbouring and have not or few initial internal defaults, a burst of the grains «confined » and of those presenting an initial pre-damage (porosity). The multi fissuration is more pronounced on the periphery of the sample. One ascertain of similar manner, but with less pronounced a «annihilation » of P.A medium: chemical reaction, non detectable with our RX setup.. ?

In on hand, the complete analysis of the microtomography is not totally over, because it involved serious problems of imagery to obtain quantitative segmentation of the objects. In on other hand, physico-chemical analysis will be need to know what going on in the «annihilation » zones. The loading at which that the sample is submit is not so simple, it needs to be clarified precisely. It seems in fact very complex as for from loading point of view by increasing the level of this through the reflection of waves between the anvil confining the sample than the finites deformations it reached. The recovered energy by rebound of the projectile is too worse information because :

1. We ignore the kinematics history of the weight and anvil ;
2. The precision of the value of this energy is low for low height of fall..



a

b

Figure 16: Test 5Kg – 10 cm Cut : a Initial ; b After test

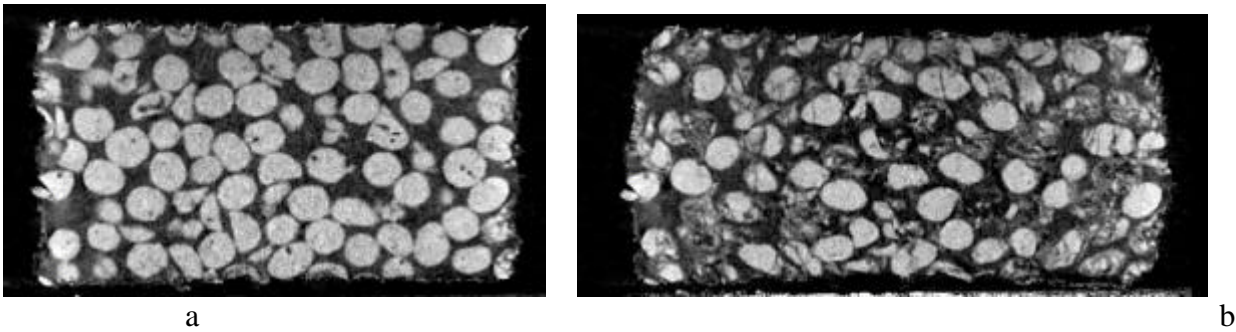


Figure 17: Test 2Kg – 10 cm Cuts : a Initial; b After test

VI. Numerical simulations.

The aim of the numerical simulations is to: 1. justify the homogenised approaches by comparison the mechanical response of the simulation of “real” and schematised configurations; 2. Extend as possible in low dynamic the schematised approach and 3. Support the definition of experimental configurations.

Until the binarisation operation is done, a tool is used which help to extract a volume of the sample, to associate at each grain a geometric representation, to make some logical operations, to build the equivalent schematisation configuration and send it to a meshing algorithm. The part of the of the butalite retained is a parallelepiped of 2.6 mm x 2.6 mm x 2.6 mm, containing 682 grains. On figure 18 the “real” and schematised configurations are shown. For the first purpose of this work, we applied boundary conditions on its block with :

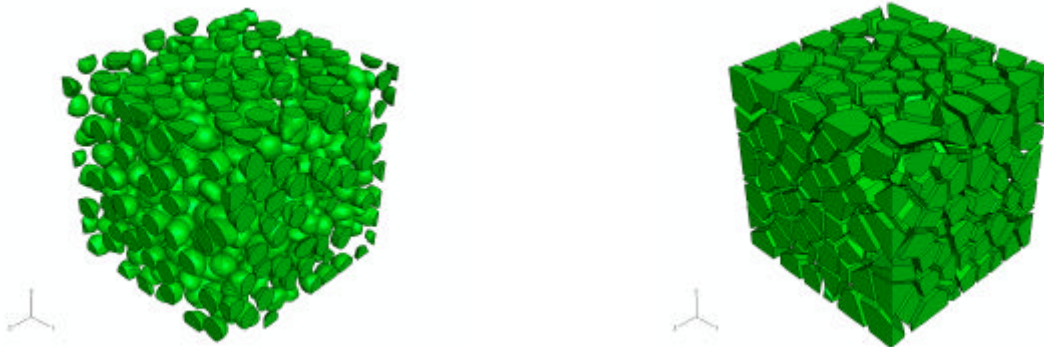


Figure 18 : Initial configurations for grains and polyhedron.

For hyperelasticity the experimental displacement measured during the hydrostatic compression, the loading is shown on figure 11 b. The constitutive equations and the material coefficients (find in the literature) are those used for homogenised tests. The results for configurations with grains , polyhedra and experimental are shown figure 19. One can see that the average F.E.M responses are globally the same but differ strongly from data. This discrepancy is probably du to the material coefficients. Numerical simulation will be performed with the coefficient got from triaxial tests which shown that for the bulk modulus indeed belongs to [0.458 GPa, 1.26 Gpa].

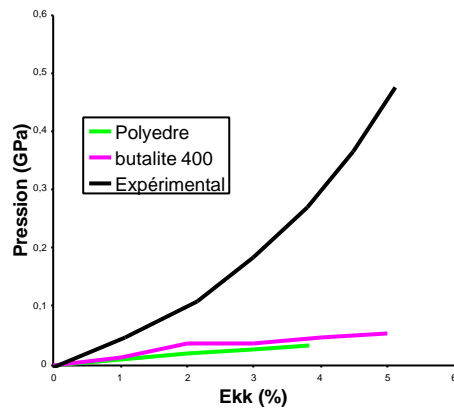


Figure 19 : Pressure versus ϵ_{kk} : Comparison between experimental data and configurations with grains and polyhedron.

Conclusion

Tools have been developed to go from the RX acquisitions to the numerical simulations. They permit to do some progresses to have better understanding about the mechanical response at the mesoscale level of propellants. Nevertheless, they must be improved particularly to increase the quality of the information we got from X-ray. The knowledge of real initial state of the sample : porosity, grains non homogenous, grains braked, distribution of grains which was not obvious initially for us must not be ignored in numerical simulations. In on other hand, the architecture of the codes is not well addressed to treat efficaciously the problems we have to solve.

The mechanical modelisation of the behaviour of bi-modal material in hyperelasticity and damage through an homogenised procedure begin to be improved, their implementations in numerical code is a part of the next step to arise the capacity of prediction of behaviour of propellants.

Knowledgments : The authors thanks P. Delcours , M. Labrunie and P. Rey for their strong help for numerical and experimental realisations.

References

- [1] J.K Dienes : Impact initiation of explosives and propellants via statistical crack mechanics. J. Mech.Phys. Solids, vol. 54 (2006), pp. 1237-1275
- [2] A. Fanget and Al : De la microtomographie au calcul numérique: premier pas. Congrès MECADYMAT Metz 3 – 4 juin 2004
- [3] D. Jeulin and Al : Morphological analysis of 3D images of pyrotechnical granular materials obtained by microtomography (in this DYMAT 2007congres)
- [4] Christoffersen : "Bonded granulates". J. Mech.Phys. Solids, vol. 31 (1983), pp. 55-83
- [5] M. Touboul and Al : A multiscale "morphological approach" for highly-filled particulate composites: evaluation in hyperelasticity and first application to viscohyperelasticity.
- [6] S. Dartois and Al : Introduction of damage evolution in a scale transition approach for highly-filled particulate composites. Ing. Fracture Mech. (to appear)
- [7] S. Castagnet : Private communication.

Temperature-time response of a UK PBX

DM Williamson¹, CR Siviour², WG Proud¹, SJP Palmer¹

¹ SMF Group, Cavendish Laboratory, 19 J J Thomson Avenue, Cambridge CB3 0HE, UK.

² Department of Engineering Science, University of Oxford, Parks Road, Oxford OX1 3PJ, UK.

Abstract

The compressive strength of EDC37 has been measured at a temperature of 293 ± 2 K over a range of strain rates from 10^{-8} to 10^3 s⁻¹, and at a strain rate of 10^{-3} s⁻¹ over a range of temperatures from 208 to 333 K. The results show that failure stress is a monotonic function of applied strain rate or temperature, which is dominated by the relaxation properties of the polymeric binder; this is confirmed by Dynamic Mechanical Thermal Analysis performed on both EDC37 and its binder. Similarities between the compressive strain rate/ temperature data sets can be understood by temperature-time superposition; data collected at a strain rate of 10^{-3} s⁻¹ over a temperature range 208 to 333 K were mapped on to a plot of strain rate dependent strength at 293 K, using an empirically determined sensitivity of -13.1 ± 0.3 K per decade of strain rate.

1 Introduction

EDC37 is a Polymer Bonded eXplosive (PBX) formed from crystalline cyclotetramethylene tetranitramine (HMX), and a gel-based binder system chosen for its explosive performance and structural properties. The HMX in EDC37 is responsible for 91 % of the compositions by mass. Figure 1 is an optical micrograph of the structure following sectioning and polishing. Within single crystals of HMX, parallel striations features can be seen. These are not artefacts of the polishing, but rather evidence of twins (Palmer and Field 1982) formed either during crystallisation, or else by being mechanically induced during charge fabrication. The 9 % of mass due to the binder is further composed of 13 % nitrocellulose and 87 % K10 nitro-plasticiser. At room temperature the binder material is well above its glass transition temperature of 210 K as measured by differential scanning calorimetry (Govier 2000).

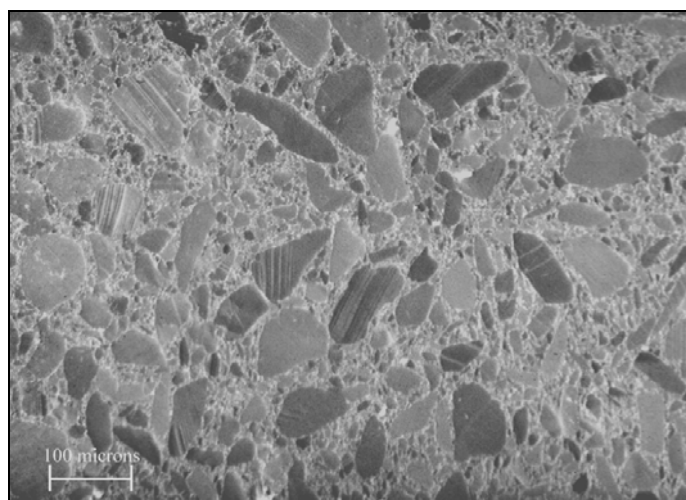


Figure 1. Micrograph of polished EDC37 microstructure.

17th DYMAT Technical Meeting, 2007, Cavendish Laboratory, Cambridge

Within the published literature, the composition conceptually most akin to EDC37 that has received the most attention, in terms of its compressive strength, is the American composition PBX 9501 (Blumenthal *et al.* 2000; Funk *et al.* 1996; Gray *et al.* 1998, 2000; Idar *et al.* 1998, 2002; Wiegand and Reddingius 2004). The main difference between PBX 9501 and EDC37 lies in the binder; EDC37 has a gel-based binder whereas PBX 9501 has a plasticized polyurethane based rubber called Estane 5703. The results for PBX 9501 show increasing strength with increasing strain rate or decreasing temperature. Strains to failure remain almost constant throughout, at a level of approximately 1 to 3 %.

Experiments on EDC37 by Siviour *et al.* (2004) at room temperature at Split Hopkinson Pressure Bar (SHPB) rates of strain have shown a similar stress-strain and strain rate dependent behaviour, albeit with EDC37 being notably weaker than PBX 9501 within the regime studied. Ellis *et al.* (2005) performed experiments in compression, flexure and tension in an investigation into damage evaluation. Each mode of testing was carried out at a fixed strain rate and temperature.

Dynamic mechanical thermal analysis is a technique that can be used to gain an impression of the relaxation processes in polymers. It has previously been used to investigate PBX and binder properties, most notably by Hoffman (2001, 2003) and references therein. Despite the wealth of data available, it is difficult to collate the compressive strain rate response of a single composition over a large range; the existing literature tends to be limited to either dynamic rates of around 10^3 s^{-1} achieved by drop-weight machines and SHPBs, or else to quasi-static rates of around 10^{-3} s^{-1} achieved with Instron-type material testing machines. Very little data exist between these two regimes.

A principal motivation for this study is the need for experimental data, required to develop and verify computational models to predict the response of EDC37 over its planned life cycle. To date there are limited published experimental data available. This study addresses this problem by combining compressive data from many experimental techniques, thereby providing a continuous data set covering eleven decades of strain rate (10^{-8} to 10^3 s^{-1}) at a single temperature of 293 K, and additionally over a range of temperatures (208 to 333 K) at a single strain rate of 10^{-3} s^{-1} . DMTA gives a measure of the relaxation properties of the NC/K10 binder material. The resulting data strongly indicate that it is the relaxation characteristics of the polymeric binder that dictate the EDC37 failure stress envelopes as a function strain rate and temperature, and that a linear time-temperature relationship can be used to describe the equivalency of the effects of strain rate and temperature.

2 Experimental

2.1 Compressive sample preparation

Samples were prepared from pressed billets of EDC37. Rods were turned on a lathe to the required diameter, and individual samples cut from the rods using a specialised fine-toothed band saw. All samples were inspected after machining, and the parallelism of the ends checked to ensure correct loading of the sample during testing.

2.2 Compressive sample size

To obtain data over a wide range of strain rates required testing at four different locations using seven different machines:

17th DYMAT Technical Meeting, 2007, Cavendish Laboratory, Cambridge

Samples investigated by the Atomic Weapons Establishment (AWE) were standard AWE compression cylinders, length 50.80 mm and diameter 20.27 mm, giving an aspect ratio of 2.5.

Samples at Picatinny Arsenal, New Jersey were cylinders of length 38.0 mm and diameter 19.0 mm, giving an aspect ratio of 2.0.

Samples at the University of Cambridge were much smaller than those investigated by AWE and Picatinny Arsenal due to the specific requirements of specimen equilibrium and inertia in high strain rate experiments (Gray and Blumenthal 2000, Gorham 1989). The samples were all of 8 mm diameter and varied in length from 2.2 – 5 mm, giving aspect ratios of 0.28 – 0.63.

2.3 Compressive sample Temperature

Experiments carried out to determine the effect of strain rate were all performed at a temperature of 293 ± 2 K.

The fixed 10^{-3} s⁻¹ strain rate, variable temperature data were obtained with the Cavendish screw-driven Instron machine, using a chamber capable of maintaining a fixed temperature over the range 208 to 333 K during the experiment, to within two degrees. Additionally some data were obtained using Picatinny Arsenal's MTS machine at 308 and 323 K and lower strain rates of 5, 50, 500 and 5000×10^{-6} s⁻¹.

2.4 Compressive sample strain rate

The fixed 293 K temperature, variable strain rate data were obtained at a variety of locations using the following procedures summarised in table 1.

Table 1. Summary of locations, equipment, strain rates and temperatures used in this study.

Location	Equipment	Strain Rates / s ⁻¹	Temperature /K
AWE Aldermaston	Creep	10^{-10} to 10^{-4}	293 ± 1
AWE Aldermaston	Instron load-hold	5×10^{-8} to 5×10^{-7}	293 ± 1
AWE Aldermaston	Slow rate Instron	5×10^{-6} s ⁻¹ to 5×10^{-3}	293 ± 1
Picatinny Arsenal	MTS	5×10^{-6} to 1	293, 308, 323 ± 1
Cavendish	Instron	10^{-4} to 1	208 to 333 ± 2
Cambridge Dept. Eng.	Schenk	2 to 230	293 ± 2
Cavendish	Drop weight	150	293 ± 2
Cavendish	SHPB	200 to 5×10^3	293 ± 2

3 Results

3.1 Compressive strength as a function of strain rate

Some typical results taken from each of the above systems are shown in figure 2; creep data are not shown as the comparatively small peak loads measured are not appropriate for this stress range. The oscillations present on the drop-weight data arise from elastic waves travelling through the gauged anvil as various structural components are mechanically excited by the impact. It can be seen that the strain at failure increases from approximately 0.5 % at the slowest strain rates to 1 % at the fastest strain rates.

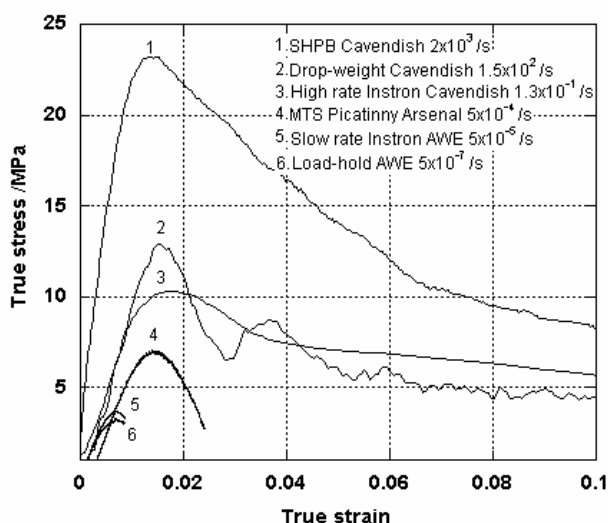


Figure 2. Typical results from the isothermal experimental techniques performed at 293 K

When all the failure stress data are plotted versus strain rate on a semi-logarithmic plot, two linear regions of positive gradient are apparent, and between these two regions a plateau is observed. Figure 3 shows the totality of the collected data.

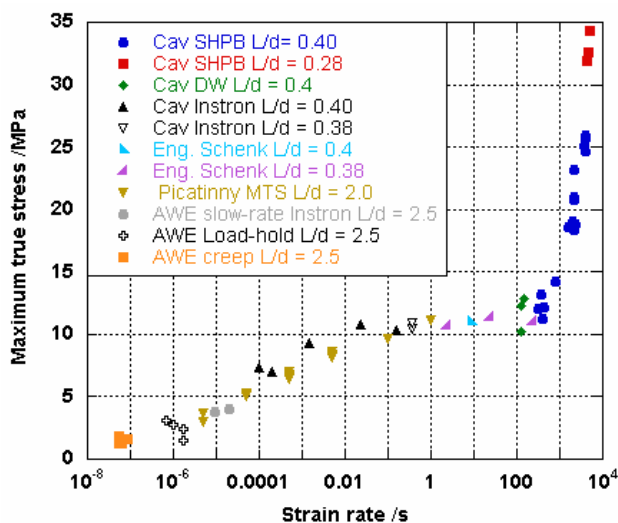


Figure 3. Fixed 293 K data: failure stress as a function of strain rate.

3.2 Compressive strength as a function of temperature

Data from the fixed strain rate, variable temperature experiments are shown in figure 4. It can be seen that the strain at failure increases from approximately 1 % at the highest temperatures to 2.5 % at intermediate temperatures and reduces to 2 % at the coldest temperatures. This greater variation in failure strain, compared to figure 2, is most likely due to thermal contraction/expansion within the sample. This was accounted for to a first approximation by taking the EDC37 contraction/expansion to be equal to the axial average linear coefficient of thermal expansion of HMX; 46.7×10^{-6} m/K (Menikoff 2002). The contraction/expansion due to the 9 %

by weight of binder is unknown to the authors, and was ignored in calculations of the sample dimension at temperature.

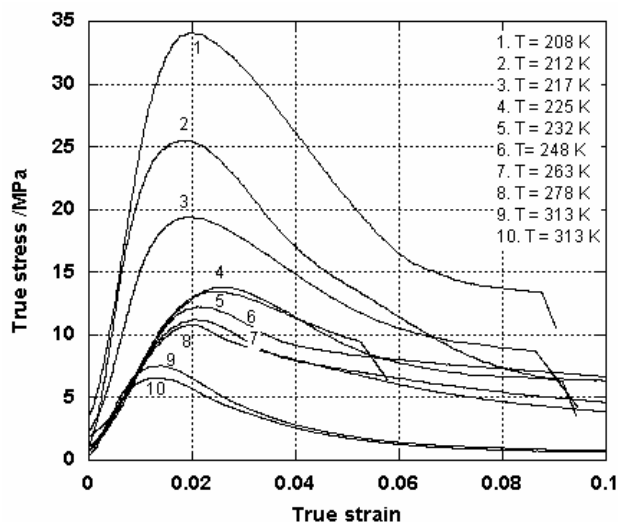


Figure 4. Typical results from the experiments performed at a strain rate of 10^{-3} /s.

Failure stress versus temperature data are shown in figure 5 on a linear plot. Note the same general trend as seen in figure 3.

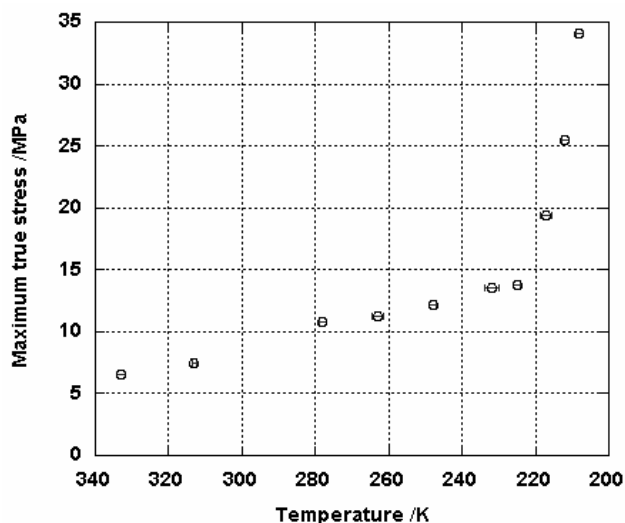


Figure 5. Fixed 10^{-3} s⁻¹ data: failure stress as a function of temperature.

3.3 Dynamic mechanical thermal analysis

Traces of storage modulus as measured by dynamic mechanical thermal analysis performed on both the NC/K10 binder system and EDC37 powder samples are shown in figure 6. The overall trend in each case is the same, and is characteristic of the relaxation processes of an amorphous polymer (Hourston 1999). That both traces follow the same trends indicates that the presence of HMX plays little role in the relaxation properties of EDC37 within the range studied.

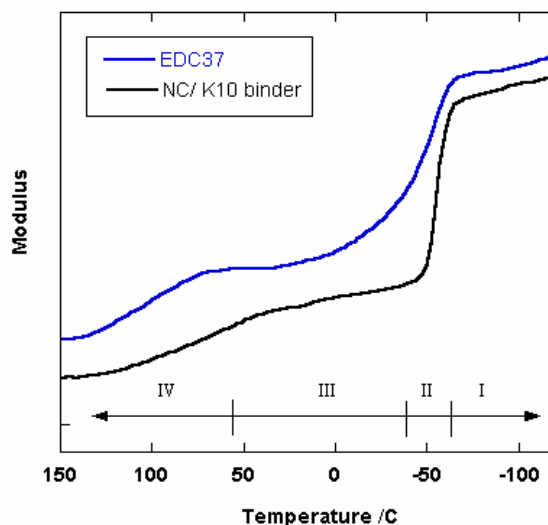


Figure 6. Storage modulus DMTA traces of NC/K10 binder and EDC37 powder samples. Region I is the glassy state, region II is the glass transition region, region III is the rubbery plateau and region IV is the melt region.

Within figure 6 region I is the glassy state, region II is the glass transition region, region III is the rubbery plateau and region IV is the melt region. These terms are explained in the following discussion section. The viscoelastic nature of the binder system means that the glass transition temperature is frequency (strain rate) dependent; hence a higher value is measured by DMTA ($-53\text{ }^{\circ}\text{C}$) than by DSC ($-63\text{ }^{\circ}\text{C}$).

Note that the EDC37 curve is somewhat smoother than that of the binder alone. This may be due to the binder in EDC37 experiencing a range of strain rates by virtue of having a range of inter-particle (binder) lengths on the microstructural level.

4 Discussion

In a paper by Siviour *et al.* (2005) on polycarbonate PC and polyvinylidene difluoride (PVDF), the authors investigated the strengths of these materials at strain rates of between 10^{-4} to 1 s^{-1} and 10^3 to 10^5 s^{-1} at room temperature, and -50 to $+150\text{ }^{\circ}\text{C}$ at 10^3 s^{-1} , using a combination of an Instron testing machine and Hopkinson bars. Dynamic Material Analysis (DMA) data were also taken at several frequencies between temperatures of -100 and $200\text{ }^{\circ}\text{C}$. It was concluded that the increase in strength observed in each material at high strain rates, was due to the shift of low temperature polymer relaxations to room temperatures via a Williams-Landel-Ferry (WLF) type time-temperature superposition relation (Williams *et al.* 1955). Using a time-temperature superposition principal, experimental results can be understood in relative terms: experiments performed at fixed temperature and varied strain rate become conceptually equivalent to fixed strain rate varied temperature experiments (and vice-versa). Within the range of temperatures and strain rates studied, the value of -17 K per decade of strain rate was found to successfully map the data from variable temperature to variable strain rate for both materials.

Thus, in the case of EDC37, the similarity between failure stress as a function of strain rate (figure 3) and temperature (figure 5) can be explained if there exists a similar time-temperature relationship.

4.1 Time-Temperature superposition

Time-temperature superposition is the phenomenon whereby a change in strain rate can equivalently be represented by a change in temperature. The physical processes that underlie time-temperature superposition can be identified with molecular motions exhibited by the polymers. Molecular motions are possible only if there is sufficient thermal energy to overcome the potential energy barriers required for movement, and if so will occur with a characteristic temperature dependant frequency and associated time parameter known as a relaxation time. Energy barriers may be described in the simplest terms by the Arrhenius equation. Given that there is sufficient thermal energy available, then for stimuli applied on time scales greater than the relaxation time the molecules can move in response, resulting in low moduli. However, for stimuli applied on time scales less than the relaxation time the molecules cannot respond, and remain essentially frozen in place, resulting in higher moduli. The relaxation time is temperature dependant, and it may be understood from simple kinetic theory that relaxation time decreases with increasing temperature. Thus it is clear that a given molecular relaxation can be frozen out either by decreasing the stimuli time scale (increasing strain rate) or reducing the temperature. The most important relaxation is the one corresponding to large scale chain motion and is known as the glass transition, this separates the glassy from the rubbery regions seen in figure 8. Secondary transitions may occur at temperatures below the glass transition and be associated with small scale chain motions, e.g. side chain motion. Providing that it is permitted (no crystallinity or cross-linking), the response to stimuli applied over the longest time scales and highest temperatures is viscous flow.

The most well-known function to describe time-temperature equivalence is that due to Williams, Landel and Ferry (Williams *et al* 1955). The so-called WLF relation describes a shift function $a_T(T, t)$ which relates changes in time to changes in temperature observed in the mechanical properties of viscoelastic solids such as polymers, it is discussed in greater detail within Ferry's book (Ferry 1980). The form of the WLF equation applicable to these data is:

$$\Delta \log(\dot{\epsilon}) = \frac{C_1(T - T_g)}{C_2 + T - T_g} \quad (1)$$

This equation describes the equivalent isothermal difference in strain rate, $\dot{\epsilon}$, between two experiments performed at the same strain rate, one at the glass transition temperature T_g and another at an elevated temperature T . When the data are referenced to the glass transition as above, then the constants $C_1 = 17.44$ and $C_2 = 51.6$ °C are found to universally apply to a large range of polymers in the range T_g to $T_g + 100$ K (Swallowe 1999).

Using the collected data, it is possible to graphically measure the apparent change in strain rate, $\Delta \log(\dot{\epsilon})$, as a function of temperature, see figure 7. This was done for the data in the rising parts of the failure stress curves only, since measurements taken in the plateau region are ambiguous in the direction of the shift. Figure 8 shows $\Delta \log(\dot{\epsilon})$ as a function of temperature, with the classic WLF curve for comparison using a T_g of 210 K. It can be seen that the measured data are much more linear than the WLF equation would predict. As in the case of Siviour *et al.* (2005), a linear fit to the data is justifiable. The errors shown were calculated in a least squares fashion.

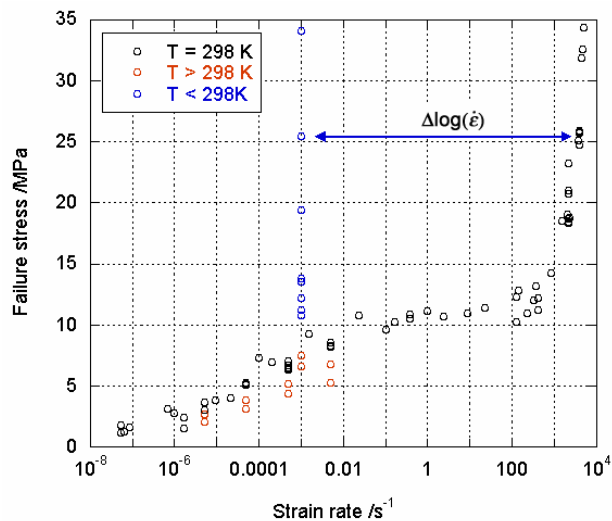


Figure 7. Graphical measure of $\Delta \log(\dot{\epsilon})$.

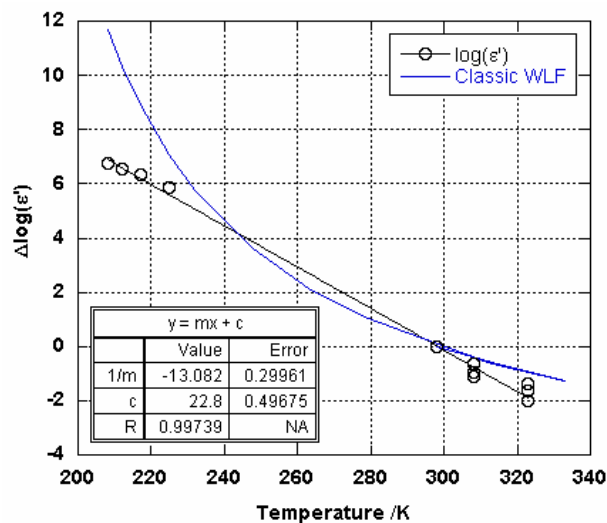


Figure 8. Strain rate shift factor, referenced to T_g , as a function of applied temperature.

Incorporating the linear fit result in to a function which describes the apparent shift in strain rate brought about by a change in temperature results in the following simple empirical equation:

$$\frac{\Delta \log \dot{\epsilon}}{\Delta T} = -13.1 \pm 0.3. \quad (2)$$

Using a linear mapping of -13.1 ± 0.3 K per decade of strain rate, the variable temperature data can be mapped on to the variable strain rate data: see figure 9. It can be seen that the mapping is successful over all the strain rates concerned. Data points 1 to 4 are taken using lower aspect ratio samples than the surrounding data.

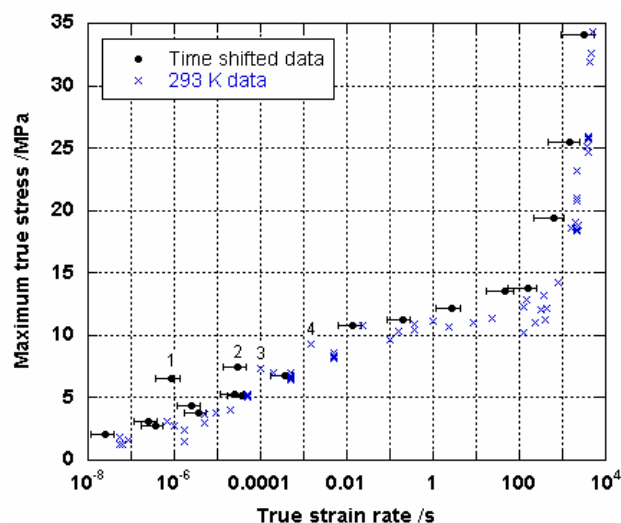


Figure 9. Application of time-temperature superposition principal using a linear transformation of -13.1 kelvin per decade of strain rate. Data points 1 to 4 are of lower aspect ratio than the surrounding data in this region.

4.2 Implication of an approximately constant failure strain

A failure strain that is relatively insensitive to strain rate and temperature is commonly seen in PBX systems, an observation which leads Wiegand (2003) to speculate about a ‘constant global-strain to failure’ criterion. Wiegand argues that the damage function is dependent only on strain, and not on temperature/strain rate. The consequence of an insensitive failure strain is that, as a first approximation, the failure stress becomes proportional to the relaxation modulus ($\sigma(t)/\epsilon$). Hence the similarity between the DMTA results of figure 8, and failure stress as a function of temperature and strain rate. The interpretation is therefore that the compressive failure stress envelopes of EDC37 as functions of both strain rate and temperature are governed by the relaxation properties of the NC/K10 binder system and they are made equivalent by a factor of 13.1 ± 0.3 K per decade of strain rate. It is important to note that in the above no mention is made of what dictates the *absolute* value of failure stress; that is a complicated function of the properties of the HMX and the binder.

4.3 Limitations of time temperature equivalency

Currently no analytical function exists to describe the form of the failure stress curves. However by using the collected data set, it is now possible to predict the ultimate failure stress over a large range of temperatures and strain rates by utilising the time-temperature equivalency.

There are of course limitations to the time-temperature equivalency analogy. In general, different relaxations may have different time-temperature sensitivities. Changing sample temperature will bring about internal stresses via differential thermal contraction, and this cannot be simulated by appropriate choice of strain rate.

5 Conclusions

Many different techniques performed at various locations have cumulated in a coherent data set that reveals the monotonic nature of the compressive failure stress of EDC37 as a function of applied strain-rate or temperature. The data cover eleven decades of strain rate and 125 K temperature range and should be valuable to future computational modelling efforts. It provides real data on the strain rate regimes as experienced by the material during its whole-life cycle against which modelling efforts can be validated.

It has been shown that the time-temperature superposition principal can be successfully applied to the compressive failure stress of EDC37, and that the shift function within the range of strain rates and temperatures studied is essentially linear. Using a value of -13.1 ± 0.3 K per decade of strain rate, the fixed strain rate data were mapped on to the fixed temperature data. The classic WLF function, with the 'standard' constants, is not suitable.

The potential benefit of a time-temperature superposition approach in further research is that if the principal can be applied with confidence, then all the required experiments to map out a materials response can be made on a single test machine with a limited strain rate range on which the temperature of testing is controllable. Thus negating the large number of experimental approaches currently needed to map out strain rate response over a practicably useful range.

DMTA has been performed on both EDC37 powder samples and NC/K10 binder. The results show that the presence of HMX has little effect on the polymer relaxation processes within the range of temperatures studied.

The compressive failure stress envelope of EDC37 has been shown to be dominated by the relaxation properties of the binder system, despite the fact that its contribution to the composition is only 9% by mass. The high degree of correlation that exists between the trends of failure stress and those of DMTA is due to a failure strain which is relatively insensitive to the effects of time and temperature.

A cautionary note is added; in general the temperature-time sensitivity of each relaxation will be different and a linear mapping as above can only be expected to work within a finite regime. Furthermore certain physical effects brought about by the application of temperature, for example the degree of internal stress due to differential thermal expansion, cannot be reproduced by appropriate choice of strain rate.

6 Acknowledgements

The authors would like to thank EPSRC for studentships for D.M. Williamson and C.R. Siviour and grants for the high-speed cameras. They would also like to thank AWE Aldermaston for samples, data, discussion and funding. D. Wiegand of Picatinny arsenal is thanked for performing the experiments there. WG Proud is QinetiQ Senior Research Fellow at the Cavendish Laboratory. CR Siviour would like to thank the Worshipful Company of Leathersellers for funding. Prof. J.E. Field is thanked for his valuable advice and comments. R. Flaxman and D. Johnson of the Cavendish Laboratory's workshop are thanked for technical assistance.

17th DYMAT Technical Meeting, 2007, Cavendish Laboratory, Cambridge**Bibliography**

Blumenthal W.R., Gray III G.T., Idar D.J., Holmes M.D., Scott P.D., Cady C.M. and Cannon D.D. 2000 Influence of Temperature and Strain Rate on the Mechanical Behaviour of PBX 9502 and Kel-F 800. In *Shock Compression of Condensed Matter - 1999* (eds. M.D. Furnish, L.C. Chhabildas, R.S. Hixson), pp. 671-674, American Institute of Physics.

Ellis K., Leppard C., and Radesk H. 2005 Mechanical properties and damage evaluation of a UK PBX. *Journal of Materials Science* **40** 6241-6248.

Ferry J.D. 1980 *Viscoelastic Properties of Polymers*. John Wiley & Sons Inc.: New York ISBN 0-471-04894-1

Funk D.J., Laabs G.W., Peterson P.D. and Asay, B.W. 1996 Measurement of the Stress/Strain Response of Energetic Materials as a Function of Strain Rate and Temperature: PBX 9501 and Mock 9501. In *Shock Compression of Condensed Matter - 1995* (eds. S.C. Schmidt, W.C. Tao), pp. 145-148, American Institute of Physics.

Gorham D.A. 1989 Specimen inertia in high strain rate experiments. *Journal of Physics D: Applied Physics* **22** 1888-1893.

Govier R. 2000 The study of thermally induced phase transitions in a Nitrocellulose and K10 polymer binder system. Degree thesis, Brunel University and Trowbridge College.

Gray III, G.T., and Blumenthal, W.R. 2000 Split-Hopkinson pressure bar testing of soft materials. In *ASM Handbook. Vol. 8: Mechanical Testing and Evaluation*, edited by H. Kuhn and D. Medlin, ASM International, Materials Park, Ohio, pp. 488-496.

Gray III G.T., Idar D.J., Blumenthal W.R. Cady C.M. and Peterson P.D. 2000 High- and Low-Strain Rate Compression Properties of several Energetic Material Composites as a Function of Strain Rate and Temperature. In *Proc. 11th Symposium (Int.) on Detonation*, pp. 76-84, Office of Naval Research.

Gray III G.T., Blumenthal W.R., Idar D.J. and Cady C.M. 1998 Influence of Temperature on the High-Strain Rate Mechanical Behaviour of PBX 9501. In *Shock Compression of Condensed Matter - 1997* (eds. S.C. Schmidt, D.P. Dandekar, J.W. Forbes), pp. 583-586, American Institute of Physics

Hoffman D.M. 2003 Dynamic Mechanical signatures of Viton A and polymer bonded explosives based on this polymer. *Polymer Engineering and Science* **43** 139-154.

Hoffman D.M. 2001 Dynamic Mechanical Signatures of a Polyester-Urethane and Plastic-Bonded Explosive Based on this Polymer. *Journal of Applied Polymer Science*. **83** 1009-1024.

Hourston D.J. *Glass transition*. 1999 In Mechanical Properties and Testing of Polymers, An A-Z Reference. ed. G. M. Swallowe, Dordrecht, The Netherlands, Kluwer Academic Publishers: pp. 109-112.

17th DYMAT Technical Meeting, 2007, Cavendish Laboratory, Cambridge

Idar D.J., Peterson P.D., Scott P.D. and Funk D.J. 1998 Low Strain Rate Compression Measurements of PBXN-9, PBX 9501 and Mock 9501. In *Shock Compression of Condensed Matter – 1997* (eds. S.C. Schmidt, D.P. Dandekar, J.W. Forbes), pp. 587-590, American Institute of Physics.

Idar D.J., Thompson D.G., Gray III G.T., Blumenthal W.R., Cady C.M., Peterson P.D., Roemer E.L., Wright W.J. and Jacquez B.L. 2002 Influence on Polymer Molecular Weight, Temperature, and Strain Rate on the Mechanical Properties of PBX 9501. In *Shock Compression of Condensed Matter – 2001* (eds. M.D. Furnish, N.N. Thadhani, and Y. Horie), pp. 821-824, American Institute of Physics.

Menikoff R. and Sewell T.D. 2002 Constituent Properties of HMX needed for Mesoscale Simulations. *Combustion Theory & Modelling*. **6** 103-125.

Palmer S.J.P. and Field J.E. 1982 The deformation and fracture of β -HMX. *Proceedings of the Royal Society of London, Series A* **383** 399-407.

Palmer S.J.P., Field J.E., and Huntley J.M., 1993 Deformation, strengths and strains to failure of polymer bonded explosives. *Proceedings of the Royal Society of London, Series A* **440** 399-419.

Schroeder W., and Webster D.A. 1949 Press-forging thin section: effect of friction, area, and thickness on pressures required. *Journal of Applied Mechanics* **16** 289-294.

Siviour C.R., Walley S.M., Proud W.G., and Field J.E. 2005 The high strain rate compressive behaviour of polycarbonate and polyvinylidene difluoride. *Polymer* **46** 12546-12555

Siviour C.R., Williamson D.M., Grantham S.G., Palmer S.J.P., Proud W.G., and Field J.E. 2004 Split Hopkinson Bar Measurements of PBXs. In *Shock Compression of Condensed Matter – 2003* (eds. M.D. Furnish, Y.M. Gupta, and J.W. Forbes), pp. 804-807, American Institute of Physics.

Swallowe G.M. 1999 *Time-Temperature Equivalence*. In *Mechanical Properties and Testing of Polymers, An A-Z Reference*. ed. G. M. Swallowe, Dordrecht, The Netherlands, Kluwer Academic Publishers: pp. 249-251.

Wiegand D.A. 2000 Mechanical failure of composite plastic bonded explosives and other energetic materials. In *Proc. 11th Symposium (Int.) on Detonation*, pp. 744-750, Office of Naval Research.

Wiegand D.A. 2003 Constant Strain Criteria for Mechanical Failure of Energetic Materials. *Journal of Energetic Materials* **21** 109-124.

Wiegand D. and Reddingius B., 2004 Mechanical Properties of Plastic Bonded Composites as a Function of Hydrostatic Pressure. In *Shock Compression of Condensed Matter – 2003* (eds. M.D. Furnish, Y.M. Gupta, and J.W. Forbes), pp. 812-815, American Institute of Physics.

Williams M.L., Landel R.F., and Ferry J.D. 1955 The temperature dependence of relaxation mechanisms in amorphous polymers and other glass-forming liquids. *Journal of the American Chemical Society* **77** 3701-3707.

Studying and modelling a pressed HMX-based energetic material.**G. Vivier^{1,2}, F. Hild², M. Labrunie³, P. Lambert⁴, H. Trumel^{1*}**

¹ Commissariat à l'Énergie Atomique, Centre du Ripault
BP 16, 37260 MONTS, France

² Laboratoire de Mécanique et de Technologie (UMR CNRS 8535), ENS Cachan
61, avenue du Président Wilson, 94235 CACHAN Cedex, France

³ Délégation Générale pour l'Armement, Centre d'Études de Gramat
46500 GRAMAT, France

⁴ Société Sciences et Applications
Le Lafayette, avenue Kennedy, 33700 MERIGNAC, France

Abstract : In the context of explosive vulnerability to low velocity impacts, the behaviour of a pressed HMX-based composition is investigated. In a first part, explosive samples are examined by polarized light optical microscopy after having been submitted to various mechanical stimuli. The respective roles of strain rate and, above all, pressure, are highlighted. The results lend some support to the frictional hot spot mechanism for ignition. A three-scale thermomechanical model is then defined, in which the material is seen as a statistical distribution of elementary cells containing a cracked grain embedded in a composite small grains-binder mixture. A mechanical model of elementary cell is then built, which allows the dissipated heat flux on crack faces to be computed. A ABAQUS Explicit simulation of a Steven test is then performed, and the macroscopic fields used as input parameters for the elementary cell model. The results show the capabilities of the model, its versatility and robustness, and indicate clearly the future research directions to be followed.

1-Introduction

The problem of explosive vulnerability to low velocity impacts has been investigated actively these years. It is now well established that regardless to the level of impact velocity, ignition prior to detonation or deflagration takes place by hot spot processes [Bowden and Yoffe, 1952]. In the case of high velocity impact, prompt transition to detonation (SDT) occurs by a pore collapse process, which becomes less and less effective as the impact velocity decreases, due to increasing small scale thermal conduction losses. Below the SDT threshold, it is thus logical to envisage new hot spot mechanisms. For the pressed HMX composition investigated here, the most likely candidate seems to be closed microcrack friction, as proposed by [Field et al., 1992], and later by [Bennett et al., 1998].

For the shock loading process involved in SDT, the load is relatively well characterized by the longitudinal stress jump across the shock surface, and stress gradients are relatively smooth along the shock surface, such that the single value of longitudinal stress most often suffices to describe the SDT process. In the case of low impact velocities, however, this is no longer the case. Very strong gradients must be accounted for, such that the problem can only be handled through numerical simulation using tensorial constitutive laws for the explosive behaviour description.

The present work aims at building a *physically-based* ignition model adapted to low velocity impact loading by a multi-scale approach, which first implies to acquire an understanding of the micromechanisms of deformation and ignition under static and dynamic loading. This

* To whom correspondence should be sent at herve.trumel@cea.fr.

defines a two-fold methodology, consisting on the one hand in investigating microstructure evolutions in response to various mechanical stimuli, on the other hand in developing a multi-scale ignition model. The paper follows this organization, and ends up with a brief outline of future plans.

2-Deformation and reaction micromechanisms

2-1-Methodology

Since it is not yet possible to perform real-time microstructural observations, deformation and reaction mechanism investigations are conducted on post-mortem samples after being submitted to various well controlled representative mechanical stimuli. Some preliminary calculations showed that, for moderate impact velocities, say below $100 \text{ m}\cdot\text{s}^{-1}$, of heavy projectiles on confined explosive samples, as in the case of the so-called Steven-test [Vandersall et al., 1998], pressure ranges between zero and a few kilobar, while maximal deformation is roughly 100%, and strain rates lie between 1 and 10^4 s^{-1} .

As seen in Figure 1 below, the concrete-like microstructure of our material suggests strong pressure sensitivity, whereas the presence of binder, although to a very limited amount, will induce rate sensitivity. As will become obvious below, the macroscopic effects of pressure and strain rate are particularly strong and must be investigated thoroughly at the microscale. Up to now, uniaxial static and dynamic (Hopkinson) compression tests have been performed, as well as triaxial quasi-static compression tests for confining pressure ranging from 2.5 to 800 MPa (8 kbar).

Samples are recovered, impregnated and mounted in epoxy. They are then sectioned and polished according to a very carefully designed protocol insuring that no preparation artefact is introduced. Samples are finally observed using polarized light reflection optical microscopy.

2-2-Initial microstructure

Figure 1 shows a large field of the initial material at medium magnification. It appears as a concrete-like material, containing large HMX grains (the aggregate) embedded in a composite matrix (the mortar) itself containing small HMX grains, a few percent of a thermoset binder, and around 1% porosity.

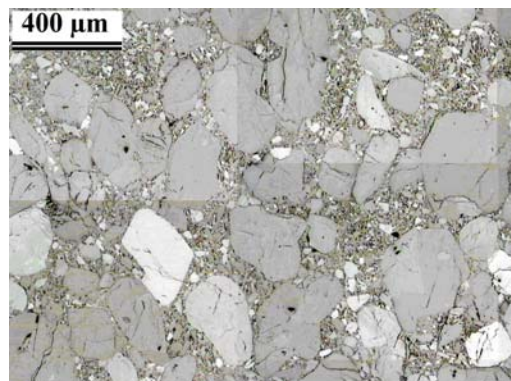


Figure 1 : *Initial microstructure.*

As the material is manufactured by isostatic pressing at high pressure and temperature, it contains defects, most of which being trans- and intergranular (debonding) microcracks. Large grains are not monocrystals, and also contain a little amount of manufacture-induced deformation twins.

2-3-Microstructural effect of various kinds of mechanical loadings

The compressive mechanical response of the material at low confining pressures is displayed in Figure 2. Uniaxial experiments reveal concrete-like, i.e. elastic damage behaviour, characterized by a (rate dependent) stress peak followed by strain softening. The post-peak behaviour is unstable and sensitive to boundary conditions. Generally, platen friction induces strain gradients and macrocracks appear at sample corners. High microcrack densities may be reached in the central quasi-homogeneous part of the samples, whereas edges are close to the initial state. Highly damaged zones are associated with typical patterns containing small scale porosity and rounded microcrack surfaces, interpreted here as unpropagated reaction zones (see Figure 3).

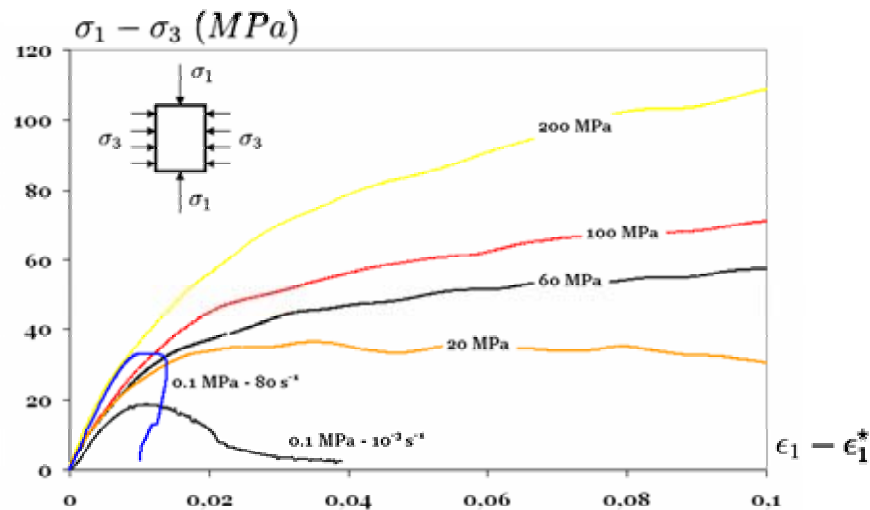


Figure 2 : *Low confining pressure stress-strain curves*
 ϵ_1^* is the longitudinal strain corresponding to a hydrostatic stress of σ_3 .

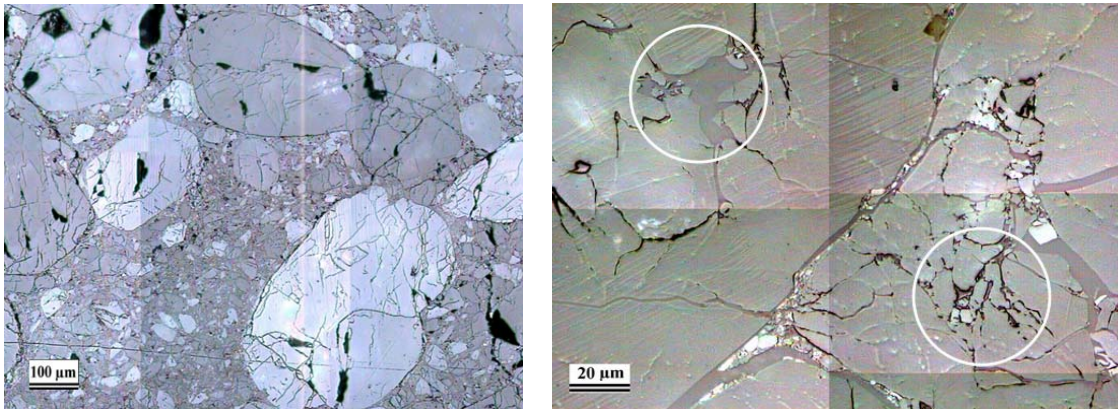


Figure 3 : *A typical microstructure after a uniaxial quasi-static experiment.*

left : strong microcrack density ; right : small scale reacted spots (white circles).

Dynamic ($\sim 80 \text{ s}^{-1}$) uniaxial compression experiments induce a similar response, except that the peak stress is much higher, and that microcracks are clearly oriented, the normal to their plane pointing towards maximum tensile strain component (see Figure 4). Moreover, the microcrack density appears much higher than in the quasi-static case, most large grains containing many parallel transgranular cracks which do not propagate through the matrix. Besides, many reaction spots are observed.

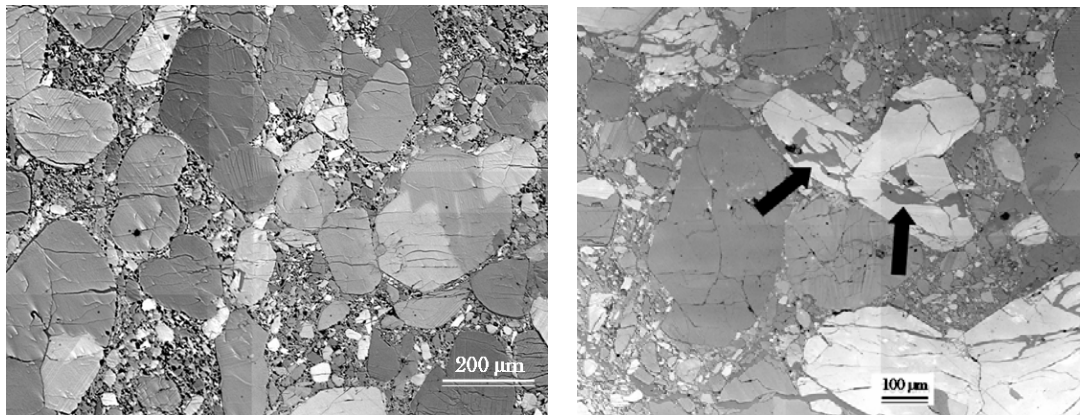


Figure 4 : *Microstructure after dynamic compression (the load direction is horizontal)
left : network of oriented microcracks ; right : a highly reacted zone (black arrows).*

Quasi-static confinement induces a transition to more ductile behaviour, as high strain levels (tests interrupted at 20% longitudinal strain) can be reached without fracturing the samples (see Figures 2 and 5). This is associated with a progressive disappearance of corner macrocracks as confining pressure increases to 200 MPa and above.

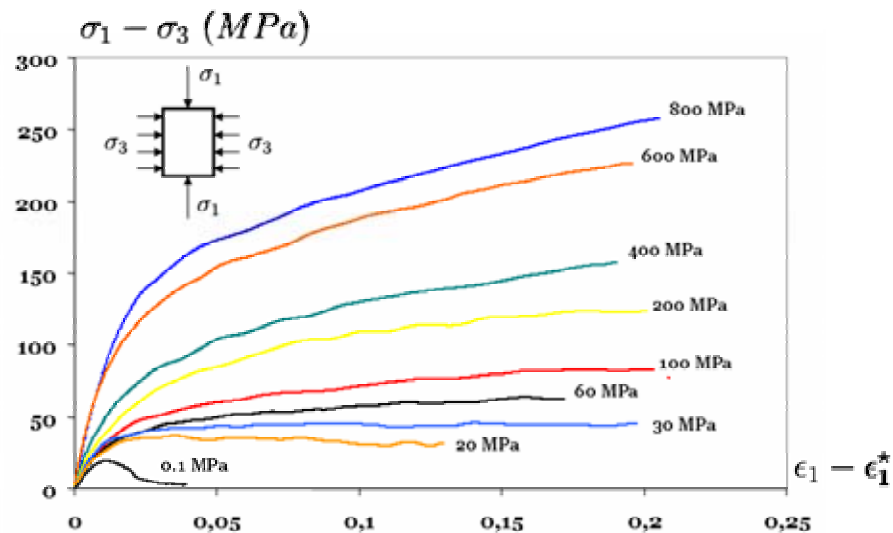


Figure 5 : *High confining pressure quasi-static stress-strain curves.*

At low confining pressure, say below 50 MPa, essentially transgranular microcracking is observed, often associated with irreversible shear displacement of some large grains (see Figure 6 left view) after complete unloading. A low density of small scale reaction spots is

observed throughout the samples. When compared to uniaxial compression samples, lightly confined ones appear less damaged, less reacted and much more homogeneous.

For higher confining pressure, large grains begin to flatten in the direction of maximum compressive strain. High magnification reveals that this is due to a very large increase of twin density. At the highest confining pressure (800 MPa), a huge twin density is observed (see Figure 6 right view), together with a *complete disappearance of microcracking and reacted spots*. Many self-embedded twin families are generally observed in the same (large) grain, sometimes resulting in a fuzzy appearance, as individual twins cannot be resolved anymore under optical microscopy.

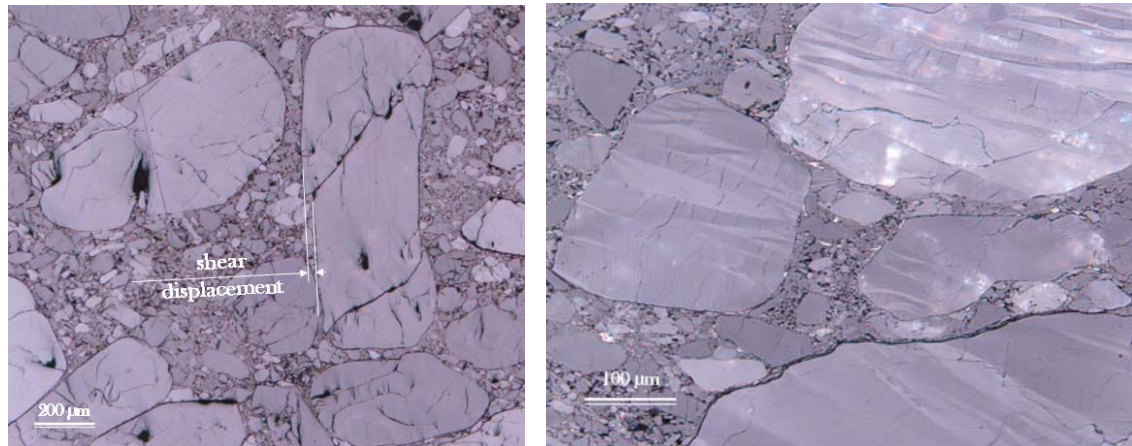


Figure 6 : Typical microstructures after triaxial quasi-static compression experiments
 left : intragranular cracks and shear displacement (50 MPa confining pressure)
 right : strong microtwinning density (800 MPa).

2-4-Conclusion

Summarizing, three major kinds of microstructural evolutions can be observed, namely microcracking, microtwinning, and microreaction. The most striking point is that microreaction is associated with microcracking, but *never with microtwinning*. The competition between cracking and twinning favors the latter at high pressure. It is important to note that intragranular microcracking is randomly oriented at low strain-rate, suggesting a crystallographic controlled process, whereas high strain-rate induces oriented cracks in the direction of principal *tensile strain (mode I fracture)*. At high pressure, microtwinning is clearly oriented in the direction of maximal principal compressive strain, and results in grain flattening.

At the meso-macroscale, a clear tendency to crack coalescence as the result of behaviour instability is noticed, whereas pressure has a strong regularizing effect. Crack coalescence, whether it takes place via mixed intra-intergranular mode or through the matrix, appears systematically oriented according to macroscopic strains.

3-Outline of an ignition model

3-1-Preliminaries : a multi-scale approach

Given the deformation mechanisms as partially clarified above, ignition may occur in two different ways. In the high pressure high strain rate regime, the material behaviour is stable, with no marked tendency to (damage) localization. Damage and thus eventual frictional cracks are homogeneously distributed, and the material can be seen as containing a population of *unconnected hot spots*. In the low pressure zone, the behaviour is much less stable, and localization patterns are likely to appear as, for example, *reactive shear bands*. Hence, a tentative scenario may be outlined as follows. A phase of homogeneous damage first takes place. If pressure and strain rate are high, frictional hot spots may appear and lead to ignition. If not, instabilities and shear bands/cracks are likely to develop, themselves possibly leading to ignition at a larger scale. Both ignition modes are physically plausible, and compatible with experimental evidence available to date.

The model developed here only considers the case of distributed frictional hot spots. Since ignition is a thermally activated process, and since mechanical energy is the input, small scale energy conversion is to be described. Hence, the ignition model must rely on a thermodynamically-based multi-scale approach, in which macroscopic fields are the input data provided by macroscopic finite element-like calculations, the output being local dissipated power, heat flow or temperature fields. Given the material's microstructure, a double scale transition is chosen, as illustrated in Figure 7. At the macroscale, the material is seen as a statistically representative assembly of elementary cells, each of which containing a single (large) grain, referred to as "the inclusion" in the sequel, embedded in the matrix. The macroscopic state of damage is described by a statistical distribution of transgranular cracks. At the mesoscale, damage is described by a probability for an elementary cell to contain a transgranular crack. At the macroscale, the statistical assembly of cells is loaded by the macroscopic stress. Within the assembly, the mesoscopic stress fluctuates from cell to cell.

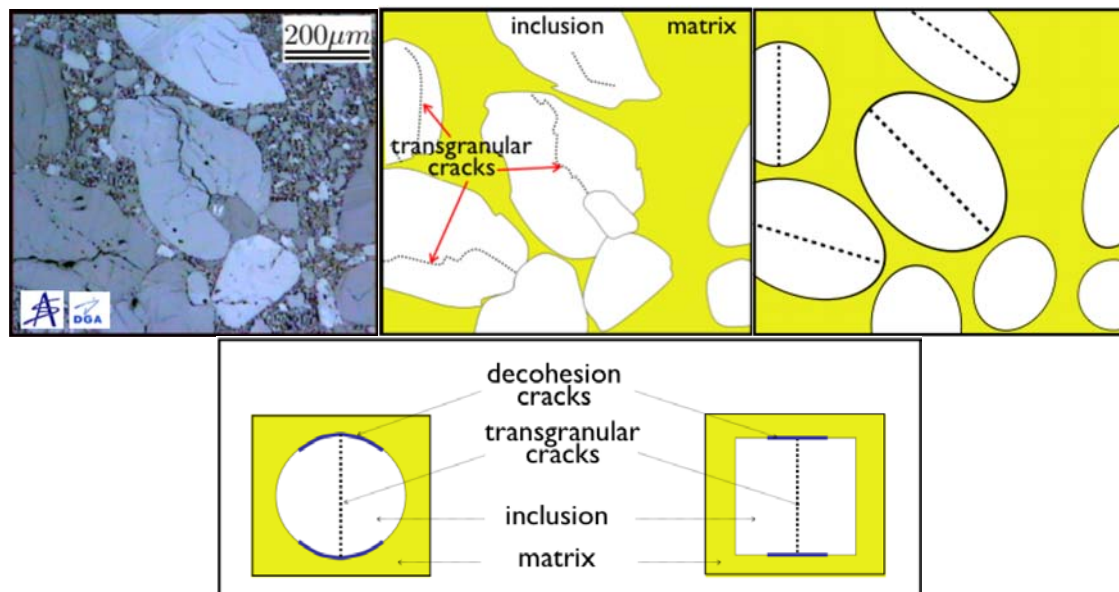


Figure 7 : The scales involved – upper left : the real microstructure – upper center : first simplification, definition of an equivalent homogeneous matrix – upper right : second simplification, grains are replaced for equivalent inclusions. Lower view : ellipsoidal inclusions are replaced by rectangular ones to simplify the analysis.

3-2-The micro-meso transition

The present paper focuses on the micro-meso transition model, i.e. on the mesoscopic cell behaviour. An individual cell, as illustrated in Figure 7 (lower view), contains a single cracked inclusion embedded in the matrix. Since an analytical formulation is sought here, the cell geometry is further simplified¹. If subjected to a tensile load normal to the crack surface, it will open and weaken the cell [Vivier et al., 2007]. However, attention will be restricted here to shear loads, more directly involved in ignition. For simplicity, only the two-dimensional case will be discussed.

In order to evaluate the heat flux dissipated on the frictional microcracks, let the cell be loaded by a uniform (mesoscopic) shear Σ_{xy} under constant normal $\Sigma_{xx} = \Sigma_{yy}$ stresses on its external boundaries (Figure 8), in order to be representative to predominantly compressive impact loads. Both matrix and inclusion are elastic, the only dissipative process being the frictional crack sliding.

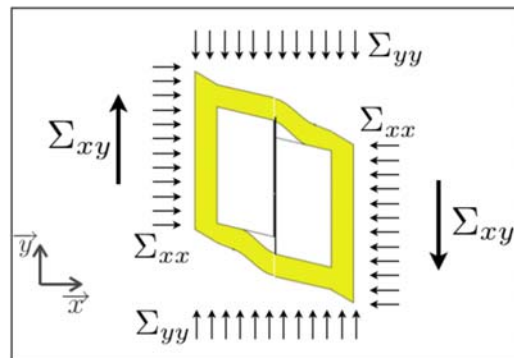


Figure 8 : The case of a sheared individual cell under normal and lateral confinement.

The dissipated energy can be evaluated as follows. At any point B of a stress-strain path shown in Figure 9, the free energy ψ characterizes the *state* of the material. Being a state potential, it depends only on initial and final states, and not on the loading path. Hence, it can be evaluated using any real or virtual path.

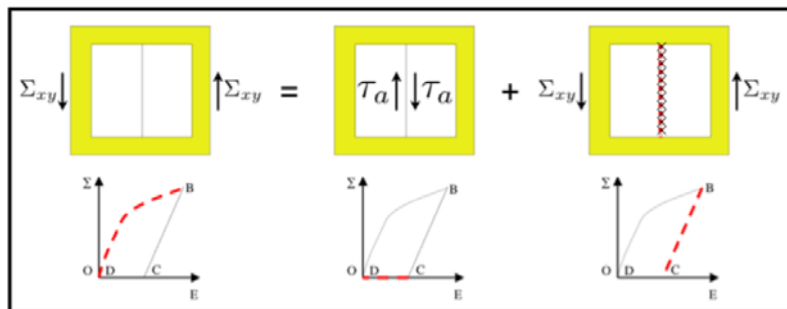


Figure 9 : Virtual loading path used to evaluate the free energy at a given state.

¹ It was verified numerically that this additional simplification does not entail the accuracy of the analytical model [Zambelli, 2007].

The *virtual path* of Figure 9 is decomposed into a first step OC, in which no external load is applied. Instead, an *internal load* τ_a is used to apply a displacement jump on the crack faces, thus inducing a self-balanced stress state σ^r . Then, the path CB is followed by applying the mesoscopic stress Σ_{xy} , thus inducing an additional stress field σ^* , until the shear stress on the crack faces reaches the Mohr-Coulomb friction limit. In this virtual path, dissipation occurs only in the first step, whereas the second one is purely elastic.

This defines a stress-driven thermodynamic-based homogenization problem [Andrieux et al., 1986 ; Arravas et al., 1990], for which the mesoscopic stress is given by the volume average $\Sigma = \langle \sigma \rangle$ and the microscopic one is decomposed into $\sigma = \sigma^r + \sigma^*$. Accordingly, the mesoscopic strain decomposes into $E = E^* + E^i$, and it can be shown that $\psi = W^* + W^r$, where W^* is the immediately recoverable elastic energy, and W^r the stored, i.e. not dissipated, energy. Given the simplified cell geometry, it is relatively straightforward to build microscopic fields [Vivier et al., 2007], and to deduce the mesoscopic response of the cell. Finally, the mesoscopic dissipation is given by $\mathfrak{D} = -\frac{\partial \psi}{\partial E^i} \dot{E}^i$, and can be transformed easily into a dissipated heat flux on the crack faces. The result is illustrated in Figure 10, in which analytical predictions are compared to numerical results performed with ABAQUS Explicit for the same geometry.

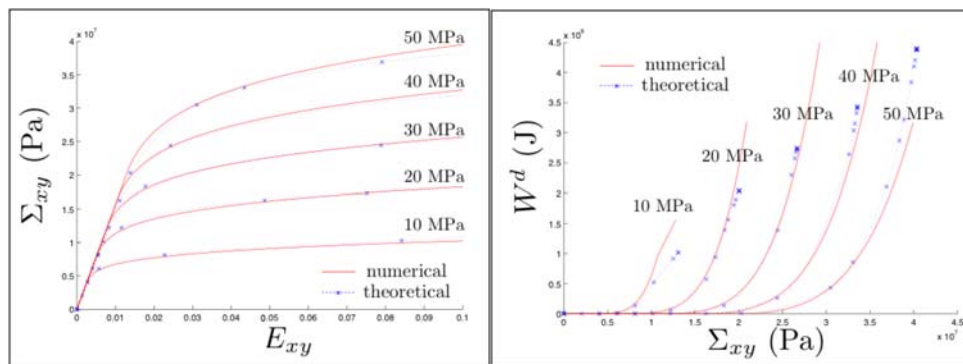


Figure 10 : Cell mesoscopic response – left : stress-strain curves – right : dissipated energy.

3-3-An exploratory application to ignition prediction

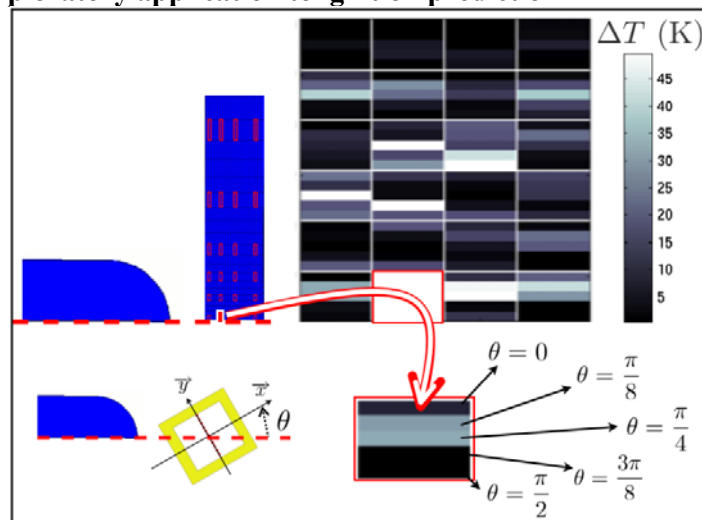


Figure 11 : Coupling between a macroscopic simulation and the mesoscopic cell model.

In order to illustrate the capabilities of the model, the following exploratory application is developed. A Steven test (projectile and target appearing in blue in Figure 11 below) is simulated using ABAQUS Explicit and a Drucker-Prager constitutive law for the macroscopic behaviour of the explosive load. In each cell, the macroscopic stress is applied as input load to the mesoscopic elementary cell model described above. Since local crack orientations are not known, this is done for several crack orientations defined in the Figure. The dissipation power and dissipated heat flux are determined in each case, and temperature computed using the adiabatic assumption.

This is illustrated in Figure 11, where an array of 24 selected cells is chosen (highlighted in red in the target). At a given time, these cells are displayed in the upper right part of Figure 11, each one containing five stripes corresponding to five different crack orientations and grey levels indicate the temperature increase. As a matter of fact, maximum mesoscopic temperatures are limited to a few tens of degrees, indicating clearly that mesoscopic temperature is not the appropriate variable to describe ignition, which rather involves hot spots and local heat conduction. Although this can be accounted for either in a coupled thermomechanical framework or using a thermochemical model (see [Browning and Scammon, 2002] for example), this is not an immediate purpose, and will not be discussed any further in the present paper.

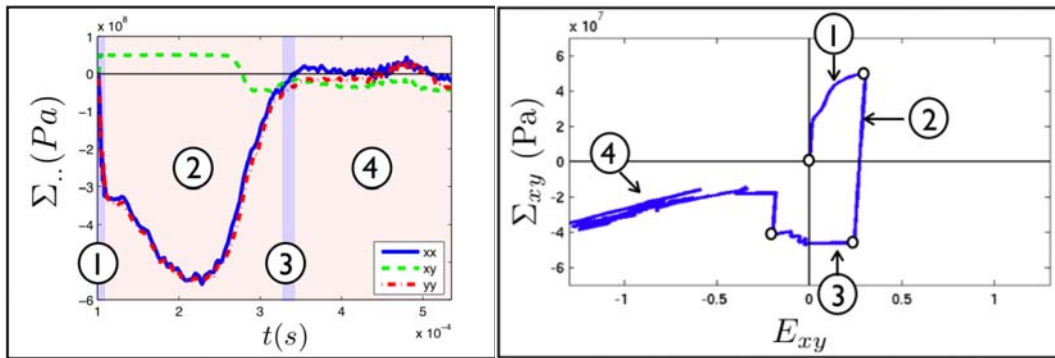


Figure 12 : Stress path for a particular cell.

Figure 12 (left view) shows the macroscopic load, i.e. shear Σ_{xy} and confinement Σ_{xx} and Σ_{yy} stresses, of a particular cell (arrow in Figure 11) in its proper reference frame, with $\theta = \frac{\pi}{4}$. The right view of Figure 12 shows the response predicted by the cell model for this load. Four phases can be distinguished. The first one, immediately after impact, is characterized by a double compression episode, up to a maximum load. When the confining compressive stresses increase sharply, the crack closes, but the shear stress is not sufficient to allow crack friction: the cell response is elastic, with a high stiffness. As the shear stress increases, friction is allowed, and the cell yields. In phase 2, the shear stress reaches a plateau, whereas confining stresses keep growing: crack sliding is hindered, and the behaviour is elastic. It remains so even during global unloading and shear reversion, until the end of phase 2. Phase 3 is characterized by crack reverse sliding, due to low values of confining stresses. In the final phase, the normal component Σ_{yy} becomes tensile, the crack opens, and induces a strong elastic softening.

As can be seen on this example, the overall cell model describes a rich phenomenology, similar to an elastic-plastic damage pressure sensitive behaviour. It appears clearly that the

17th DYMAT Technical Meeting, 2007, Cavendish Laboratory, Cambridge

role of confinement, i.e. pressure, is crucial. It is also worth noticing that friction, i.e. dissipation, can occur during loading and unloading as well, which may reveal important for ignition prediction. Moreover, notice that crack sliding episodes are short, such that heat conduction should not be very effective (low losses). However, this example should not be taken as definite, since the macroscopic load was directly applied to a cell. But the real material is in fact a cell assembly, and mesoscopic stress fluctuations from cell to cell should be accounted for, as well as microstructure evolutions, i.e. grain cracking, during dynamic loading.

5-Future plans

This work is in progress in at least three respects. First, the knowledge of deformation and reaction mechanisms under combined high rate and pressure remains to be established. Second, the meso-macro transition is being undertaken at the present time, together with the development of the microcrack density (and orientation) evolution law. Third, the macroscopic model derived in this way should replace the Drucker-Prager constitutive law mentioned above, rendering the overall approach more consistent.

Acknowledgements

The authors are indebted to Patrick Rey for sample preparation and polishing, and to Denis Rocher for conducting the quasi-static uniaxial compression experiments. The financial support of CEA is gratefully acknowledged.

References

- S. Andrieux, Y. Bamberger, J.-J. Marigo, 1986.**
Un modèle de matériau microfissuré pour les bétons et les roches.
J. Méc. Théor. Appl., **5** (3), 471-513.
- N. Arravas, K.-S. Kim, F. A. Leckie, 1990.**
On the calculation of the stored energy of cold work.
ASME J. Eng. Mat. Technol., **112**, 465-470.
- J. G. Bennett, K. S. Haberman, J. N. Johnson, B. W. Asay, B. F. Henson, 1998.**
A constitutive model for the non-shock ignition and mechanical response of high explosives.
J. Mech. Phys. Solids, **46** (12), 2303-2322.
- F. P. Bowden, A. F. Yoffe, 1952.**
Initiation and growth of explosion in liquids and solids.
Cambridge University Press, Cambridge, UK.
- J. E. Field, N. K. Bourne, S. J. P. Palmer, S. M. Walley, 1992.**
Hot-spot ignition mechanisms for explosives and propellants.
Phil. Trans. R. Soc. Lond. A, **339**, 269-283.
- R. V. Browning, R. J. Scammon, 2002.**
Microstructural model of ignition for time-varying loading conditions.
Shock Compression of Condensed Matter (M. D. Furnish, N. N. Thadhani and Y. Horie eds), American Institute of Physics.

17th DYMAT Technical Meeting, 2007, Cavendish Laboratory, Cambridge

K. S. Vandersall, S. K. Chidester, J. W. Forbes, F. Garcia, D. W. Greenwood, L. L. Switzer, C. M. Tarver, 2002.

Experimental and modelling studies of crush, puncture, and perforation scenarios in the Steven impact test.

12th Int. Symp. on Detonation, San Diego (Cal.), USA.

G. Vivier, H. Trumel, F. Hild, 2007.

On the stored and dissipated energies in cracked systems.

To be submitted to Cont. Mech. Thermodyn.

S. Zambelli, 2007.

Allumage par points chauds d'un explosif comprimé soumis à l'impact d'un projectile.

Mémoire de Master, Ecole Normale Supérieure de Cachan.

Application of the Porter-Gould Model to IM Scenarios

I. G. Cullis*, P. D. Church, R Cornish, P. Gould, V Ingamells, D. Porter

*QinetiQ plc

Fort Halstead,

Sevenoaks, Kent TN14 7BP

UK

email: igcullis@qinetiq.com

INTRODUCTION

Significant UK Ministry of Defence (UK MoD) research funding over many years has been expended in the development of an improved understanding of hazard processes in energetic materials. This is essential research since a weapon system will usually spend only a tiny fraction of its expected lifetime in operational service. For the majority of its life it will be stored. It will also, at various times, be handled, inspected, transported and possibly non-destructively tested. In all these activities it may be exposed to hazards, which could affect its operational readiness, or even cause it to have detrimental effects on personnel, equipment, weapons platforms, facilities and other weapon systems. The capability to assess the risks during all these phases of a weapon's life is necessary to enable appropriate safety regimes to be implemented.

There is thus a requirement for a well-defined risk factor, which requires that the hazard is assessed and understood for which in turn a reliable methodology is needed.

For the past 6 years, UK research into energetic hazard has been undertaken by a QinetiQ led academic-industrial consortium including Fluid Gravity Engineering Ltd, BAESYSTEMS Land Systems and the Defence Academy at Shrivenham.

Significant progress has been made towards the long-term goal of identifying a means for the efficient, cost effective and accurate assessment of safety and its application to life assessment studies. Fundamental to the achievement of this long term aim is the requirement to understand the science and to develop UK capabilities in all three of the technical building blocks that define the hazard problem. Our research builds upon this developing understanding and seeks to integrate the progress made in these building blocks into an improved modelling capability.

The underlying technical strategy recognises that all hazard responses are characterised, to a greater or lesser degree, by the following thermo-mechanical processes:

- Constitutive Response: deformation heating, damage, fracture, cracks, surface area creation.
- Chemical Response: ignition and growth.
- Burning Response: deflagration, detonation.

Modern warfare with the concept of the Balanced Force demands the transport and storage of different mixes of weapon systems and ammunition in forward ammunition dumps. An understanding of the associated hazard would allow this to be achieved with a minimum and well-defined risk factor

The long-term goal of our research is to develop reliable and accurate hazard assessment methodologies that could be applied to life assessment studies to allow the removal of the current conservative approach to lifing of munitions and improve the value from their in-service life.

This paper describes the application of the material science based models developed by D. Porter and P. Gould to describe the equation of state, constitutive response and damage models and their use in IM scenarios.

HAZARD RESPONSES

There are a number of threats to which a munition is likely to be exposed to during its life cycle. Other additional threats may be credible for specific munitions as a result of their operational environments. They have to be taken into account when developing the IM signature. The IM signature is developed using an IM protocol, which in NATO countries is the NATO document 'Guidance on the Assessment and Development of Insensitive Munitions (MURAT)', dated May 2006 [1]. It is the NATO nations agreed guide that forms the basis of the IM protocol to define a weapon system's IM signature. This agreement is recorded in STANAG 4439.

The protocol recognises 5 response types:

- Type I: Detonation characterised by a supersonic decomposition reaction.
- Type II: Partial detonation.
- Type III: Fast combustion of confined material (explosion) with a local pressure build up.
- Type IV: Combustion/deflagration characterised by a non-violent pressure release.
- Type V: Combustion.

Our research to date has concentrated on Shock to Detonation (SDT) phenomena in Polymer Bonded Explosives (PBX) explosives, since this response is that most frequently observed in bullet attack, fragmenting munitions attack, shaped charge jet attack and sympathetic reaction caused by a blast wave.

MATERIAL MODELS

The ability to predict the response of an energetic material under shock wave loading is crucially dependent upon the ability of the material models to reproduce the observed thermo-mechanical and other physical properties of the material. With properly physically based material and ignition and growth models we have an excellent capability with which to describe the response of a munition to bullet, fragment and shaped charge jet attack.

The materials of interest in our studies are the research PBX explosives known as RF-38-22 and RF-38-09, both (88%RDX / 12% HTPB) compositions, which differ in their particle size distributions.

Equation of State

The Porter-Gould EoS developed as part of the UK research programme [2] was used to describe the P-ρ-E-T response space for RF-38-22 and RF-38-09. The EoS surface (P-ρ-E), which also includes the melt phase change, is shown in figure 1.

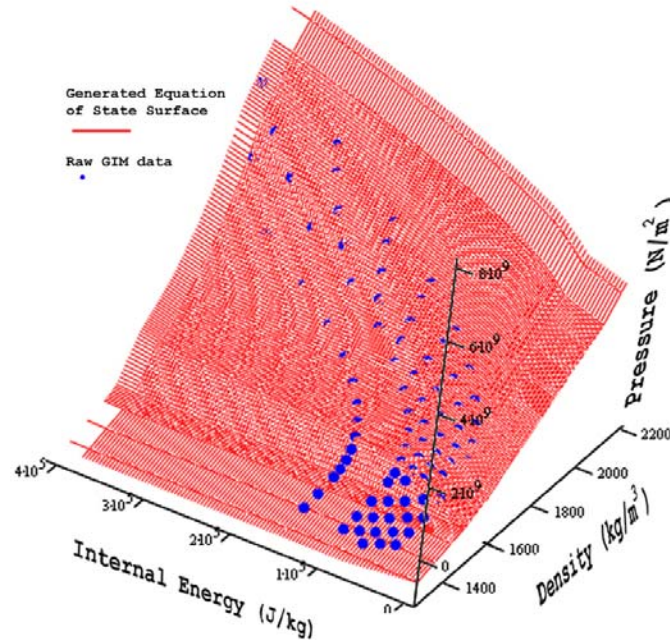


Figure 1: Porter-Gould EoS surface for RF-38-22

This EoS is provided as a table look-up in the Sesame format. The table is generated from the raw data generated by the Group Interaction Modelling (GIM) model due to Porter [3]. As with all table look-up schemes the difficulty lies in properly defining their boundaries and trapping any non physical states that can result when the calculated state moves outside of these boundaries.

Constitutive Response

The constitutive model for a PBX composite developed by Porter and Gould under the Hazard UK research programmes predicts the evolution of the composite modulus as a function of length scale and damage. The method utilises GIM via Molecular Dynamics Modelling (MDM), and by investigating the distribution of particle sizes within the HTPB binder, deduces that the interaction between the particles at each length scale can be neglected for RF-38-22. Thus the modulus can be calculated at each length scale in turn. More recent developments have included a description of particle-particle interaction for compositions with reduced amounts of binder.

A simple compliance model, in terms of volume fractions (f), then predicts the modulus (M) of this local composite, assuming the moduli of the components are known, is as follows :

$$\frac{1}{M_{local}} = \frac{f_{V,particle}}{M_{particle}} + \frac{f_{V,binder}}{M_{binder}} \quad (1)$$

At the next higher length scale the distance between particles is approximately three times larger than the size of particles at the length scale below allowing the smaller particles to fit easily into the space and to remove any particle/particle interactions between length scales. The modulus of the local composite with lower length scale is then taken as the “binder” modulus for a local composite at the next higher length scale. Equation 1 is used once again to produce a local modulus at this length scale. This process is repeated to determine the modulus of the whole composite using only the binder modulus, the particle modulus and the particle size distribution as input parameters.

The composite is thus seen to be an elastic material with known moduli. Mechanical tests show that this elastic behaviour is maintained to stresses of 0.3-0.4MPa, beyond which brittle failure occurs, catastrophically in tension and gradually in compression. There are three potential failure sites: particles, binder and particle/binder interfaces. Of the three, the binder is not only the weakest component but is also where the majority of the mechanical energy is deposited. It therefore dominates the mechanical response.

The constitutive model can be expressed as a simple perfectly elastic model, of the form $\sigma = M\varepsilon$, which is relatively straightforward to implement into hydrocodes. Poisson’s ratio is determined by the shear and bulk moduli of the composite. This also defines the elastic limit, beyond which the material fails. It is assumed that there is no plasticity.

Damage

In the case of shock to detonation transitions (SDT) the constitutive response is not considered as a significant contributor to the ignition process, since the energy in the volumetric component of deformation is significantly greater than that in the shear deformation component. However it has been recognised that a crucial part of predicting hazard is to link material and mechanical damage to the ignition and growth and grain burning algorithms, since damage provides the ignition sites or hot spots known to initiate the burning response. Here the constitutive response has an important role to play.

GIM calculates properties of polymers by considering the separation distance of polymer chains. If the polymer chain separation is increased beyond a certain distance then the weak bond between chains will be broken on one side. This relaxes any constraint on the polymer chain but still allows it to support load via bonds with chains on other sides. On a continuum level we can introduce the concept of a “failed” state – a polymer chain that has been separated from some of its neighbours by a cavitation event. As crazing is a general nucleation of cavitation sites then in any particular volume, there will be a fraction of “failed” states that do not contribute to constraint – although they will contribute to modulus. Thus for conditions of hydrostatic tension the number of failed states is:

$$f_f = \frac{2 * \exp\left(-\frac{E_0}{E}\right)}{1 + \exp\left(-\frac{E_0}{E}\right)} \quad (2)$$

In the model we only evaluate this expression if there is a positive change in mechanical energy in the numerical cell and if the hydrostatic stress state is tensile. The value of E_0 is currently empirical and takes a value of 40kJ, but should be able to be derived, since it

is the failure energy density in the binder on the smallest length scale with an appropriate magnification factor. This strain magnification factor is required to convert global strain to the local strain experienced by the binder. This factor has yet to be defined and the current work to implement the new multi-rate polymer model is addressing this. Until this work is complete the value of E_0 is determined from experiment. In this equation it should be noted that f_f can never be greater than 1.

This damage factor then modifies the binder modulus via the equation:

$$M_b = 2.5 - 1.9 * f_f \quad (3)$$

The damage model described here interprets the theory on the molecular scale to give its effect on the modulus of the material. As discussed below, however we also require an interpretation of damage that can yield numbers and sizes of real microstructural features for direct input into hazard calculations.

Fracture

In addition to the damage model the material description also includes a volumetric strain failure model. The failure model calculates the volumetric strain and compares it against a defined failure strain. Once the material in the numerical cell has been flagged as having failed, the fracture algorithm returns the material to ambient density and inserts either void or gas into the resultant void created in the material. The failure algorithm therefore generates voids in the material, which can thus mimic hot spots although the microstructure of the material needs to be borne in mind.

In the case of the RF-38-22 the volumetric failure strain is the strain at which the potential function, that defines the equation of state, in tension reaches a pressure at which it is considered that the material can no longer support load. In this case the limiting value of V/V_0 in tension is 1.2. We have to include this limit since further expansion beyond this point results in non-physical behaviour; the material has failed.

The failure model, however, in this instance acts on the equation of state and therefore does not change the modulus, in the way that the damage model does, which implies that we have two independent processes in operation.

Our research into ductile fracture model for metals [4] recognised that void growth is driven by the hydrostatic pressure. The metal surrounding the voids work hardens as they grow and this is fed back into the calculation of damage via the constitutive model. The crucial development in this approach was the recognition that the algorithm provided a direct link between the volumetric strain and the number of voids in the element at its failure. The failure of the element was therefore due to damage in the material rather than a direct artefact of the equation of state.

In the case of an explosive, such as a PBX, damage occurs through the creation of many small cracks which grow and coalesce. Around an energetic particle, these cracks will drive the debonding process and on coalescence form the voids seen in images of the damaged material. In principle we can consider these cracks as voids and follow a similar approach to metals to couple the volumetric strain to the damage model. However we then need experimental data to be able to calibrate the predicted levels of damage with those predicted by the damage model.

Ignition Mechanisms

It is well known that there is a broad spread in ignition levels in the same energetic material. Whilst this is due to a range of effects and environmental factors, it is reasonable to suppose that morphology and mechanical response are two important ones. The morphology defines the constitutive response and the constitutive response controls the response to the loading history of the system, i.e. damage, fracture, deformation heating. Damage can also result from other processes, e.g. chemical degradation in the binder and other ageing effects.

The link between the constitutive and ignition algorithms is, therefore, an important element of any model to be capable of describing the response of an energetic material to a range of stimuli. This is important, because the number and evolution of ignition sites is directly related to the constitutive response and in particular the level of damage in the material. The damage and fracture processes lead to the creation of free surfaces with obvious influence on the sensitiveness and explosiveness of the energetic material.

In other explosives microstructural features such as voids and shear sites have been shown to form hotspots (i.e. void collapse) and the current generation of ignition and growth models assume an initial population of these features in an explosive. Both the Cook-Haskins Arrhenius Reaction Model (CHARM) [5] and the ignition and grain burning model developed by Milne [6] estimate this population via the equation:

$$\phi = N_0 \frac{4}{3} \pi r_a^3 \quad (4)$$

Here N_0 is the number of pores of radius, r_a , which can be either a free parameter or based upon image analysis of the specimen. The porosity is estimated from a measurement of the density of the specimen and the Theoretical Maximum Density (TMD) of the material as shown in equation 5.

$$\phi = 1 - \frac{\rho_{specimen}}{\rho_{TMD}} \quad (5)$$

It is an important parameter for an explosive and improved methods to determine it need to be developed.

Whilst the strategy of using this initial population as a constant or for fitting purposes works well in many SDT scenarios, e.g. fragment attack, Pop-Plot prediction, large scale gap tests etc, a good understanding of the material science of PBX composites together with the available microstructural information can be used to determine a realistic initial population, based on the number of voids in the crystals, which is constant, and more important the evolution of this population in response to thermal and mechanical stimuli.

To assess the hazard response of any damage to the PBX a link between the microstructural (rather than mechanical) response and these two parameters is needed. The damage model described above was further developed when it was recognised that since the damage mechanism is the deformation energy it is this quantity that should be the damage criterion for PBXs. It could also be linked to the size/distribution of voids. This reformatted criterion equated the mechanical work done, W , to a function of the

surface energy, length-scale and fraction of total surface area of cavity in order to show how the modulus of the composite material changed with damage. The equation used is:

$$W = \frac{6\Gamma}{d} \Delta f \quad (6)$$

Here Γ is the surface energy (usually $0.15\text{J}\cdot\text{m}^{-2}$ for polymers), d is the length-scale and Δf is the fraction of total surface area.

The quasi-static testing of the material showed that debonding was the principal damage mechanism. If we therefore assume the damage is taken to be debonding of particles to form a void at or near the particle/binder interface then the above formula (equation 6) can be used to monitor the increase in void number with damage. Additional modelling simulations of the shock response of these ‘debonding voids’ on the surface of a crystal showed that they acted in a similar way to the CHARM void collapse mechanism or the visco-plastic collapse used in the FGE model.

The theory of brittle failure implies that the damage will accumulate around the largest particles at low stress and as mechanical work is done to the composite, debonding of smaller particles will occur. The particle size distribution for RF-38-22 enables the fraction of surface area to be related to cumulative number of debonded particles by taking each size in turn. The shape of the particles does not matter so long as they are all similar. For particles precipitated from solution this should be a reasonable assumption. Figure 2 shows a graph of the relation.

On this basis we can therefore construct a damage model that can provide a variable value of N_0 the number of ignition sites due to void collapse, that locally evolves with mechanical damage on the basis of the energy deposited in the energetic material. This has yet to be completed but is part of our future research plan.

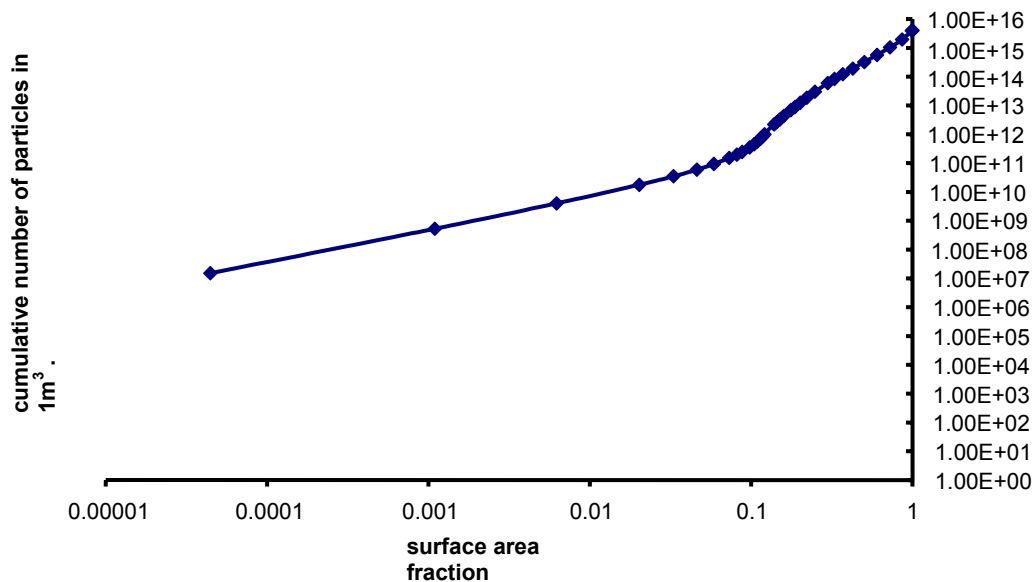


Figure 2: Number of debonded particles as a function of increasing surface area fraction

We thus have a model that can be initially used to understand how damage might evolve in a munition during an insult, deformation and/or shock, that would then increase the void distribution in the explosive and hence its sensitivity. It can also be used to define an initial void population density, based on an assumed level of initial strain, for the ignition and growth models.

APPLICATIONS

The paper concludes with some examples of the application of the Porter-Gould material models in a number of IM related simulations using the GRIM2D hydrocode. Work is planned to validate these predictions in a future experimental programme.

Taylor Test

The Taylor test is a classic test [7] that has been used over many years to test a range of materials. It can be used to characterise elastic perfectly plastic constitutive models for a range of materials. It has also been used to identify damage and failure mechanisms in metals [8,9] and energetic polymer composites, more recently for example [10,11,12]. The recovered specimens are ideally suited to tomographic analysis [9] to identify damage distributions.

In its simplest form a rod of the material under test is fired at velocities up to about 200-300m.s⁻¹ at a rigid boundary and the specimen recovered. The deformation of the specimen can then be used to characterise simple constitutive models and internal damage models. Figure 3 shows the results of a simulation at 5 μ s and 24 μ s for RF-38-22 at an impact velocity of 150m.s⁻¹.

The damage at 5 μ s reflects the radial flow field that is established in the material. The vertical cracks that establish in a polymer composite such as a PBX are visible in this figure, driven by the volumetric failure model. Regions of damage along the centreline are very similar to sites of void nucleation observed in tomographic examination of copper Taylor test specimens [7]. The damage is seen to be evolving from the edge of the specimen as one would expect. By 24 μ s the damage has reached its maximum within a conical section of the specimen. Physically this implies that the energetic crystals have completely debonded from the material. It is interesting to note the region of less damaged material about 3cm from the impact face, which is created as a result of the wave interactions within the specimen.

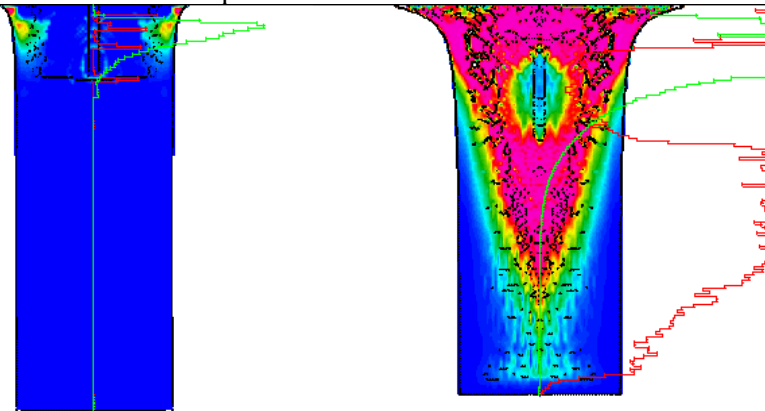


Figure 3: Taylor test – damage at 5 μ s (left) and 24 μ s (right)

experiment. A series of simulations using GRIM2D with the CHARM heterogeneous model therefore explored their ability to reproduce these experiments. As in the experiments a number of simulations were run at different impact velocities in order to determine the NO-GO/GO velocity threshold for each barrier thickness.

As there was no One Dimensional Time To Detonation (ODTX) data for RF-38-22 available at the time the CHARM reaction chemistry was fitted to 5mm thick aluminium barrier impact data. The predicted NO-GO velocity was 1300m.s^{-1} compared to an experimental value of 1405m.s^{-1} and the predicted GO velocity was 1500m.s^{-1} compared to 1499m.s^{-1} in the experiment.

Figure 5 shows the sequence of events in a typical fragment impact. The plots show the 13.15mm steel projectile impacting the explosive sample, covered by a 3mm steel barrier, at 1550m.s^{-1} . The plots show contours of the internal energy (left) and pressure (right) in the inert explosive i.e. modelled without the CHARM reaction chemistry. The fragment and barrier are shown as interface plots to indicate the fracture in the materials.

The barrier plate begins to show signs of fracture at $1.5\mu\text{s}$ after impact, at which time the shock wave has travelled into the explosive material. At later times, as the fragment moves further into the barrier, the shock wave spreads out into the material. The internal energy shows a peak value just behind the barrier, close to the central axis of the sample.

A sufficient build-up of pressure and heat in the explosive can lead to a detonation. When the fragment experiment is modelled with the CHARM reaction chemistry, the method of determining whether any reaction has occurred which could lead to detonation in the explosive, is to examine the fraction of reacted gas in the material, since the final reaction products in CHARM are gaseous.

The NO-GO and GO impact velocities determined for steel and aluminium barrier plate tests using the 13.15mm projectile are compared against the experimental data in Figure 6, where it may be observed that the agreement with the experimental data is variable over the range of aluminium barrier plate thicknesses. For example for the bare explosive the NO-GO and GO velocities are both higher than those predicted by the experiment. In contrast when a 1mm barrier is placed in front of the explosive, the predicted GO and NO-GO velocities are very close to the experimental values; similarly good agreement is shown for the 3mm aluminium barrier. The poorest agreement between the predicted and experimental velocities is observed for the 4mm barrier thickness, where the predicted GO velocity is 100m.s^{-1} below that observed in the experiment. It is interesting that the experimental data shows a large jump in velocity when the barrier is increased from 3mm to 4mm but then reduces again at 5mm. This behaviour is not captured in the modelling results presented here. It clearly requires further investigation.

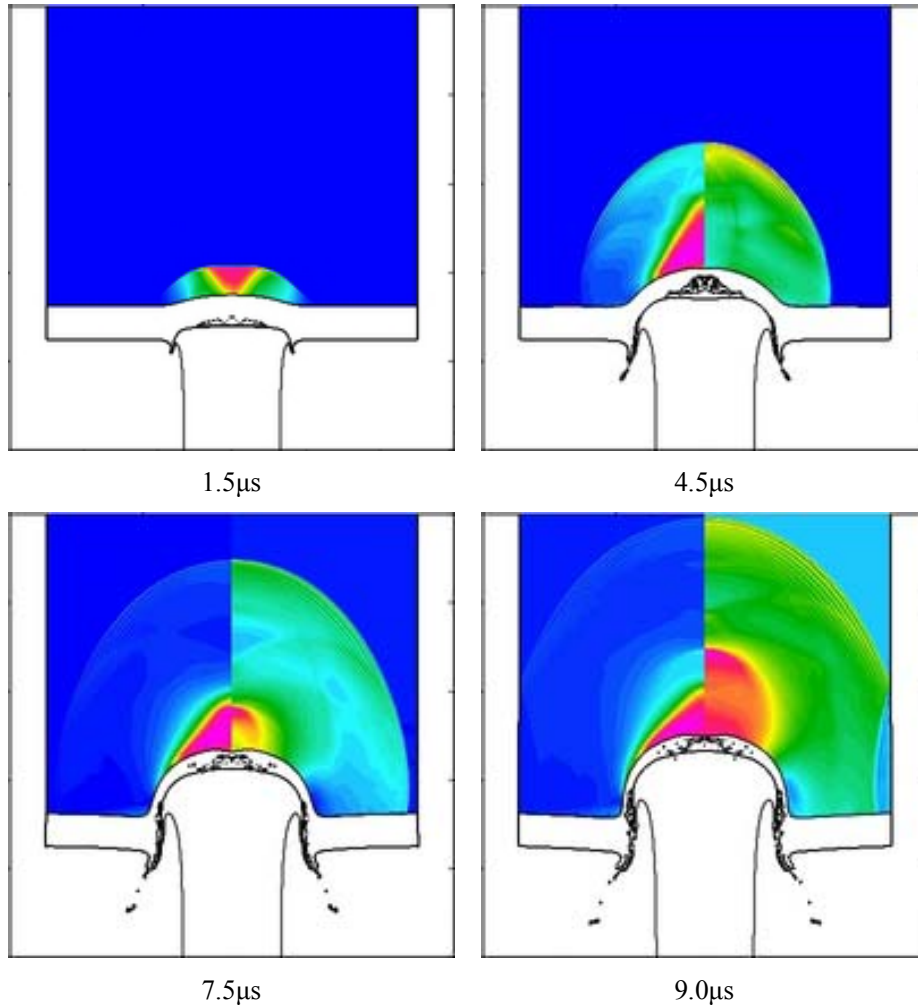


Figure 5: Internal energy (left) and pressure (right) profiles in an explosive during a fragment impact

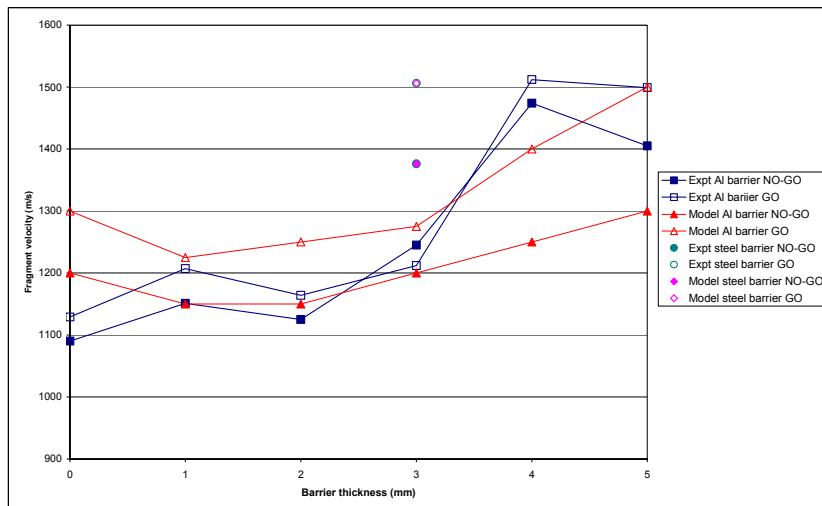


Figure 6: Comparison of the predicted GO and NO-GO velocities with the experimental data.

A key experimental requirement is to identify where and when ignition occurs to provide a more rigorous validation of the material and ignition and growth models. Future research will address the design of suitable experiments.

CONCLUSIONS

This paper has described the application of physically based equation of state, constitutive and damage models to predict the response of a PBX polymer composite. The numerical simulations have demonstrated that the models can produce physically realistic descriptions of the generation and evolution of damage within the PBX material. These models can also be used in simulations to design suitable experiments to provide more detailed information on damage type and distribution and hence rigorously validate the models and identify missing physics.

In combination with the CHARM ignition and growth model the Porter-Gould material models have been shown to be capable of predicting the experimentally observed fragment velocities that define the detonation threshold. Further work to formally integrate the damage model into CHARM as a hot spot source is required together with experiments to identify the point and time of first ignition.

The progress to date has provided the encouragement to begin work on the more complex Burn to Violent Reaction regime.

ACKNOWLEDGEMENTS

The authors acknowledge the support of WPE of MOD for funding the research described in this paper.

REFERENCES

1. 'Guidance on the Assessment and Development of Insensitive Munitions (MURAT)'. Allied Ordnance Publication (AOP) -39 edn. 2 May 2006.
2. 'A General Equation of State for Polymeric Materials', D Porter, P Gould, Jnl Phys IV, DYMAT 2006, pp 373-378
3. 'Group Interaction Modelling of Polymer Properties', D Porter, Marcel Dekker 1995.
4. B. Goldthorpe; A path dependent model for ductile fracture, J PHYS IV 7: (C3) 705-710, (1997).
5. M D Cook, P J Haskins, C Stennet. "Development and Implementation of an Ignition and Growth Model for Homogeneous and Heterogeneous 'Explosives'". 11th Detonation Symposium, 1998, pp589-598
6. 'Advances in the Understanding of the Large Scale Gap Test', S. J. Burley, N. K. Bourne, V. Fung, R. Hollands, J. C. F. Millett, A. M. Milne, A. Wood, APS Shock Compression of Condensed Matter, 2005, pp944-947.
7. G I Taylor. "The testing of materials at high rates of loading". J. Inst. Civil Eng. 26, 1946, p486-519.
8. D D Radford, P D Church, P J Gould, E Eadington. "Deformation and failure during 'symmetric' Taylor impact tests". Plasticity, Damage and Fracture at Macro, Micro and Nano Scales, ed. A. S. Khan and O Lopez-Pamies, pp 663-665, publ.Fulton, Maryland, Neat Press.
9. Chapman D. J, Radford D D, Reynolds M, Church P D. "Shock Induced Void Nucleation During Taylor Impact". Int. J. Fract. 134 41-57.
10. Quidot M, Racimor P, Chabin P. "Constitutive Models for PBX at high strain rate". Shock Compression of Condensed Matter – 1999, ed. M D Furnish, L C Chhabildas, R S Hixson, pp. 687-690, publ. Melville, New York, American Institute of Physics.
11. Matehson E R, Rosenberg J T. "A mechanistic study of delayed detonation in impact damaged solid rocket propellant". Shock Compression of Condensed Matter – 2001, ed. M D Furnish, N N Thadhani, Y hoire, pp. 464-467, publ. Melville, NY, American Institute of Physics.
12. Scholtes G, Bourma R, Weterings F P, van der Steen A. "Thermal and mechanical damage of PBX's."

BEHAVIOUR OF PBX BASED ON RDX AND HMX PARTICLES, UNDER HIGH DYNAMIC SHOCK

J. Campos, J. Ribeiro, R. Mendes, I. Plaksin, J. Gois, L. Pedroso and J. Cirne

LEDAP – Laboratory of Energetics and Detonics

Mech. Eng. Dept. of Faculty of Sciences and Technology
University of Coimbra – Polo II, 3030-788 Coimbra, PORTUGAL

Abstract

Most shock experiments with energetic particles are related to studies of shock to detonation transition of PBX, and not to analyse its behaviour under high shock loads. The typical shock experiments are described, showing its application in non-reactive syntactic foam. The use of Multi-Fiber Optical Analyzer allows simultaneous registration of the dynamic and profile characteristics of induced shock wave, by the registration of self-radiation of shocked materials. An experimental case study of single HMX particles, inside different binders, was tested. PBX samples, fabricated from RDX and HMX particles, were studied in Shock-to-Detonation Transition experiments, respectively generated from a flyer impact and under the wedge test configuration. The simultaneous probing of radiation field, emitted from the shock front and the Chemical Reaction Zone structure, when occurs, allows the precise study of energetic particles and its derivate PBX behaviour under shock conditions.

1. INTRODUCTION - SHOCK EXPERIMENTS

1.1. **Most existing experiments** with energetic particles are related to studies of shock to detonation transition, or detonation initiation, and not just to analyze energetic materials behavior under high shock loads. Most of the studies are related to evaluate the shock sensitivity of PBX samples, fabricated from nitramine particles, in order to determine conditions and delays of Shock-to-Detonation Transition (SDT), with simultaneous registration of dynamic and kinetic characteristics of reaction growth. The development of new insensitive energetic materials also implies the existence of strong shock initiating devices, precise and reliable, and new accurate experimental measurement methods, in order to characterise the behaviour of this kind of explosives under high intense shock loads.

Two ways are generally considered to generate intense shock waves in materials: the plate shock impact and shock transmission from a plane wave generator, or from an explosive donor. Many authors are proposing experimental and numeral approaches to predict and design shock generators. Most of them are also proposing simple numeral codes in order to determine the level of induced shock, and the selected materials and dimensions for obtaining this levels (vd. <http://teos.ficp.ac.ru/>). They are always based in the shock data of materials and experimental results.

One of the ways to generate shock load in a sample of acceptor explosive, is to transmit a shock pulse from a detonation wave from an explosive donor, having known detonation properties, through a barrier of a perfect known material (Mylar, Kapton or PVC), placed between the explosives donor and acceptor.

Another and most precise way to generate shock loads is using a flyer plate impact from an electric gun. When the flyer plate strikes the target, the collision process generates a pressure pulse of high intensity, having its amplitude and time duration controlled respectively by the velocity and thickness of the flyer plate. When a pressure pulse has an enough intensity to initiate the PBX, the shock wave, inside the explosive, accelerates continuously until to be converted in a detonation wave (DW). It was also verified that a strong pressure pulse, generating a short shock to detonation transition (SDT) in the explosive, allows the use of small and thin samples.

1.2. **The registration optical method**, developed in LEDAP since 1996, based on 64 optical fibers ribbon (250 μ m of diameter each fiber), connected to a fast electronic streak camera (vd. Mendes, R. et al., 1996, and Plaksin, I. et. al., 1997) allows the simultaneous registration of several detonation parameters in one experiment. It is always used to characterise the DW velocity, detonation pressure, detonation front curvature, shock to detonation transition SDT and collisions of DW (Mach wave formation/ and relaxation process) (vd. Mendes, R., et al., 1997 and 1998 and Plaksin, I. et. al., 2000).

More recently the registration optical method based in those optical fibers ribbon, was enhanced to characterise, by radiation oscillations in a mesoscale level, the kinetics instabilities in chemical reaction zone related also to the initial heterogeneities of the explosive, that are a function of the explosive particle sizes in PBX, (vd. Plaksin, I. et. al., 1997, 1999, 2001). Experiments were always conducted with application of the LEDAP's multi-fiber optical analyzer (MCOA) combined with the fast electronic streak camera Thomson TSN 506 N. The metrology allows measuring, in real time, the shock wave motion and shock front structure inside materials (inert and energetic) at different run distances. Figures 1 and 2 illustrate the schematic of the MCOA facility and its application for simultaneous measurements of detonation velocity, D , and velocity of shock front motion, U_s , in standard optical monitor. Six 125- μ m Kapton films separated from each other by five μ m-argon gaps form the optical monitor. The photo-chronogram presented in Figure 2 illustrates both records: the DW motion across the strip of sixteen 250 μ m-optical fibers integrated to the multi-fiber optical probe "MFOP-D" and the SW propagation through the Kapton films. Forty-eight fibers integrated to the "MFOP-Us" record light flashes that are arisen when the SW front crosses the argon micro-gaps.

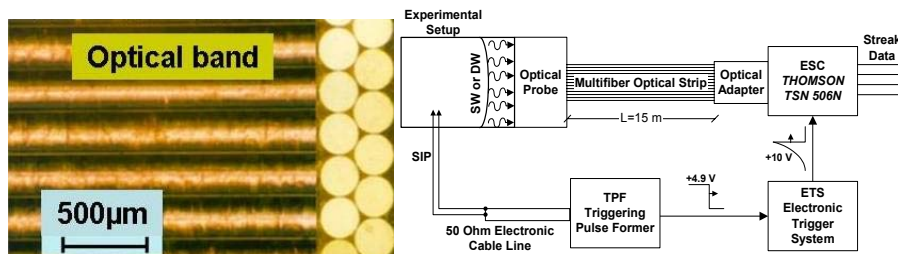
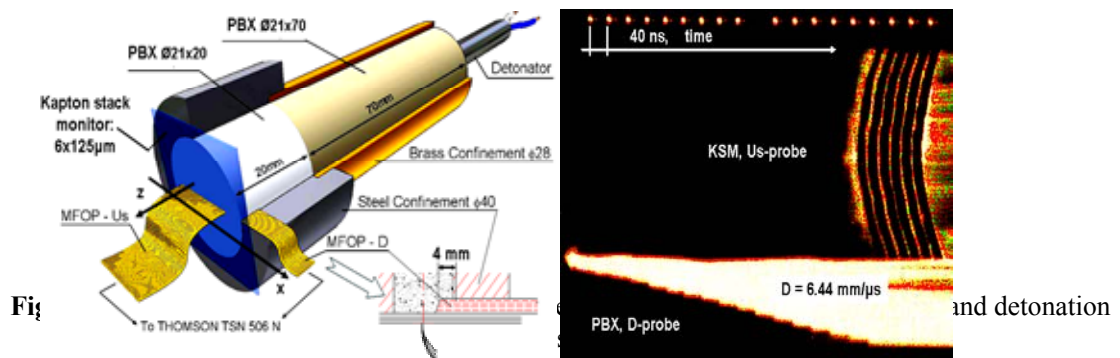


Figure 1. - Schematic representation of optical recording system.



1.3. Generally it is assumed **explosives always present voids** that generate hot spots during compaction process, when they are submitted to intense shock loads. J. Ribeiro et al. (2000, 2003) presented an intensive work, **using syntactic foams based in epoxy resin and Hollow Glass Micro Spheres (HGMS)**, instead of PBX based on nitramine particles, allowing the study of shock compression and Hugoniot curve evolution, **without the possibility of a further initiation**. The use of syntactic foams,

obtained from the mixture of a thermoset resin with HGMS, presents as an essential feature the possibility to control, in wide limits, the size, the amount, the shape and even the relative position of the pores. The macroscale equilibrium models show the relation between porous and non porous Hugoniot curves. Among them, the Mie-Grüneisen method proposed by Jacques Thouvenin, in the Fourth International Symposium on Detonation (*vd.* Thouvenin, 1965) proves to be verified in this kind of porous materials. The HGMS used in the sample preparation were silicate glass shells of small dimension, with the thickness of the shell equal to a fraction of its diameter, that are presented as a fine, light and loose white powder. According to the manufacturer its effective specific mass is 0.21 g/cm³ with 80 % of the volume being occupied by spheres with diameters ranging from 30 to 167 μm , having a characteristic diameter of 92 μm . Four compositions were used in those experiments, with increasing mass concentrations of HGMS from 0, to 5, 10 and 25 %. The obtained values of effective density (ED) are shown in Table 1.

Table.1 – Values of the mass and volume ratios, between the HGMS and the polyester resin, and theoretical value (maximum) and experimental (effective) values of the specific mass, values of the volume of the HGMS add to the resin.

Short designation	Mass ratio HGMS/PR	TMD [g/cm ³]	ED [g/cm ³]	$\frac{\text{TMD}}{\text{ED}}$	Vol. HGMS [%]
RP0	0	-	1.161	-	-
RP5	0.05	0.987	0.970	0.983	18.758
RP10	0.10	0.868	0.849	0.978	31.334
RP25	0.25	0.666	0.642	0.964	52.145

Two kinds of **explosive shock generators** have been used in these experiments. The one used for the low pressures range is based on a configuration first proposed by Chen *et al.*, 1993, designated as an inert material Plane Wave Generator [PWG], whose working principle is based on the differences in the propagation velocities in a reactive and in an inert material and on the shock and detonation waves optical properties. A schematic representation of the particular configuration used in this case was presented previously (*vd.* J. Ribeiro *et al.*, 2003). Different pressure values are obtained using the wave generator, without intermediate shock absorber(IM0), or using it to accelerate a 5 (IM5) or a 10 mm (IM10) copper plate that will hit a 5 mm thick PMMA plate after which is placed the sample. For the high-pressure range experiments it was used of a simple cylindrical PBX (based on RDX) explosive charge, confined in a 70 mm long and 25 mm internal diameter PVC tube, as shock generator. This configuration, shown in Figure 3, allows the simultaneous experiment of different samples under the same (initial) shock conditions, avoiding differences from one explosive donor to another.

Flyer plate impact experiments, using an electrical gun, were also made for the determination of the Hugoniot curve of the samples, using a flyer plate of polyester, 0.25 mm and 0.350mm, under two levels of the initial tension in the electrical gun capacitors (25 kV (FP25) and 30 kV (FP30)). In both plate impact and high-pressure explosively shock loaded experiments the thickness of the samples was between 0.500 and 1 mm. The intensity of the shock wave, induced by each one of the used generators in standard materials samples is shown in Table 2.

The values of the propagation velocity the determination of the Hugoniot Curves is made by calculating first the value of u_p , then the corresponding value of P and finally using the mass conservation equation, the value of the specific volume.

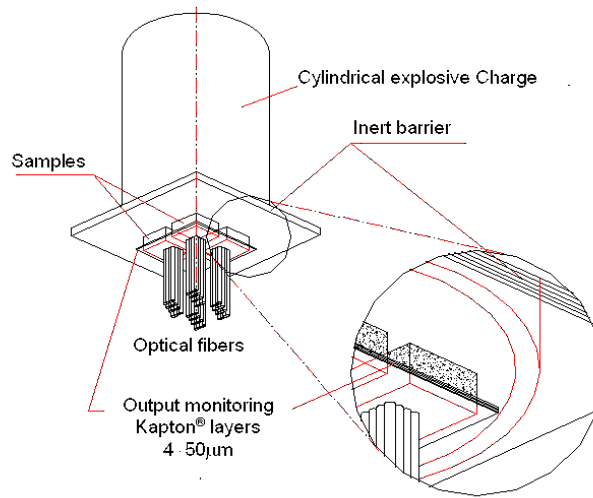


Figure 3- Schematic representation of the tested samples, and its optical probe position over them, used for the evaluation of the shock wave propagation velocity in thin samples.

Table 2 – Shock generator type and intensity of shock

Generator type	IM0	IM5	IM10	PBX	FP-25	FP-30
Reference material	PMMA	PMMA	PMMA	Kapton [®]	Mylar [®]	Mylar [®]
Intensity of the SW [GPa]	4.04	0.48	0.20	17.7	≈26	≈31

The results of those calculations, performed with data from all the described experiments (vd. J. Ribeiro, 2000, 2003) are presented in the graphics of Figure 4 in P - v planes. Together with the experimental data, in the P - v graphics, are also shown the Hugoniot curves of Glass, Polyester (vd. LASL, 1980, p. 394 and 436-437), and a hypothetic solid, designated as RP25 – non porous, that should be considered resulting from the mixture of polyester and glass in a mass ratio of 100 to 25, respectively. In those graphics are also shown the Hugoniot curves predicted by the Grüneisen and by the Thouvenin/Hofmann models. Data description by the Thouvenin/Hofmann model can be considered good but data description by Grüneisen cannot be at same level. It is observed that there is an extreme dependence of the results obtained with this model on the values assumed for the Grüneisen coefficient. Small variations in that coefficient can result in large variations in the calculated pressure. In this case it was considered that $\Gamma/v = \Gamma_0/v_0$, where Γ is the Grüneisen coefficient, v is the specific volume and the index 0 the initial conditions of the non-porous material. corresponding to each one of the tested samples.

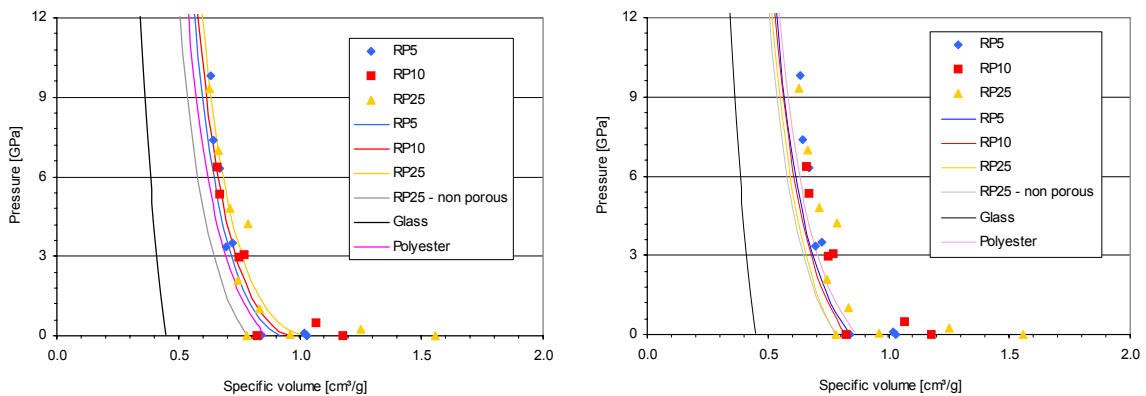


Figure 4 – Hugoniot Curve in the plane P - v (with results from Thouvenin model and Mie-Grüneisen model) for the samples RP5, RP10 e RP25

1.4. Recently I. Plaksin and C. S. Coffey (2007) presented results containing information about the **genesis and evolution of reaction field** in the HMX-based PBX submitted to shock. Different aspects seemed to be considered in shock behavior:

- reaction localization and dissipation caused by the shear stress,
- driven plastic deformation, in explosive crystals, effect of the HMX grain size upon the genesis and scale of localized reaction sites,
- reaction spots and origination of oscillating/galloping regimes of detonation front motion, and
- application of the spatially resolved shock front speed and pressure (complete vector values), contributing to a more precise equation of state (EoS) related to the initial phase of front motion.

1.5. The **following text** concerns the development of a precise technique, where the shock is generated by LEDAP electric gun, to determine the Hugoniot curve and its related equation, in the case study of PBX based on RDX particles, developed by R. Mendes et al., since 2001, and the most recent results obtained mainly by I. Plaksin et al., 2005, 2006, 2007, cited before, of the shock behaviour of single HMX particles immersed in different binders and a PBX based on HMX particles.

2. BEHAVIOUR OF A PBX, BASED ON RDX, UNDER INDUCED SHOCK FROM THIN POLYMERIC FLYER.

2.1. The LEDAP slapper. Thin polymeric flyer plates were accelerated by a high voltage discharge across the metal bridge foil, placed under the flyer plate. Depending on the bridge dimensions, the bridge vaporises in a very short time and generates a very high pressure. The generated metallic plasma, confined by the barrel and tamper material pushes out a section of the polymeric film, above the bridge, to form the flyer plate. The pressure into the target depends on the flyer plate velocity and the shock properties of both the flyer plate and target material. The duration of the pressure pulse into the target is mainly a function of the flyer plate thickness and of the shock velocity in the flyer plate material. Figure 5 presents a typical arrangement scheme of our electric gun, called slapper and designated by LED-MAP.

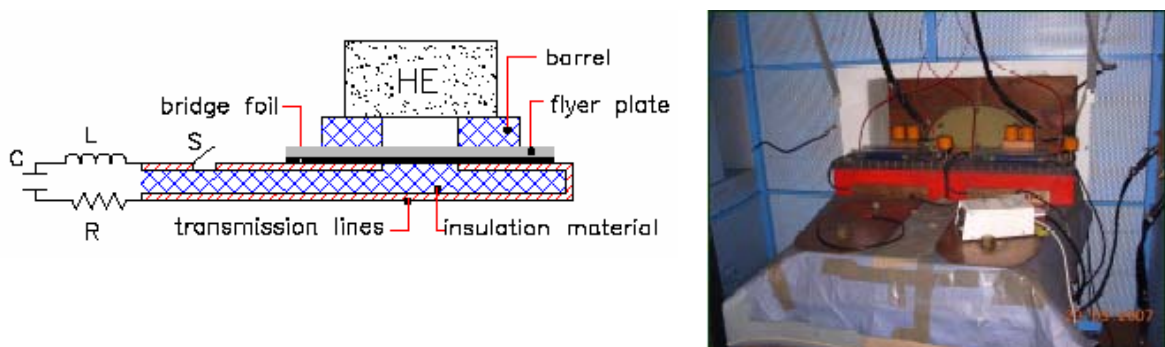


Figure 5. Typical scheme of electric gun, slapper, arrangement and view of capacitor bank.

The main properties of the LED-MAP and flyer plate are presented in Table 3 and Table 4.

Table 3. Electric parameters of the capacitor bank.

C	R	L	V_{\max}	ω	$(dI/dt)_{\max}$
[μF]	[$\text{m}\Omega$]	[nH]	[kV]	[Mrad/s]	[TA/s]
25.4	4.2	31.5	40	1.1	1.3

Table 4. Main characteristics of the Flyer Plate.

Material	Kapton; Mylar
Thickness	50 – 700 μm
Diameter	5 – 35 mm
Velocity	9 – 2.5 km/s
Pressure ¹	53 – 7.9 GPa

¹ Pressure induced on a kapton target induced by a Kapton flyer

2.2. Flyer plate velocity. The optical fiber ribbon is placed inside the barrel and the top of the optical fibers is cut with a known wedge (vd. Figure 6). Then, when the flyer plate crosses the barrel, it will impact successively each optic fiber, generating a light pulse, which is recorded with a fast electronic streak camera. On the top the fibers are isolated also with an air gap, with 0.1mm of thickness between the top of fibers and the cover (vd. Mendes, R. et. al. 1996, 2001). A typical record is presented in Figure 6. Knowing the wedge angle between the fibers top and the flyer surface, the (Z,t) diagram of the flyer movement inside the barrel can be estimated. To find the flyer velocity the same procedure as described for the single fiber method was used. A typical (Z,t) diagram of the displacement curve, fitted to the experimental points, and the flyer velocity curve are presented in Figure 7.

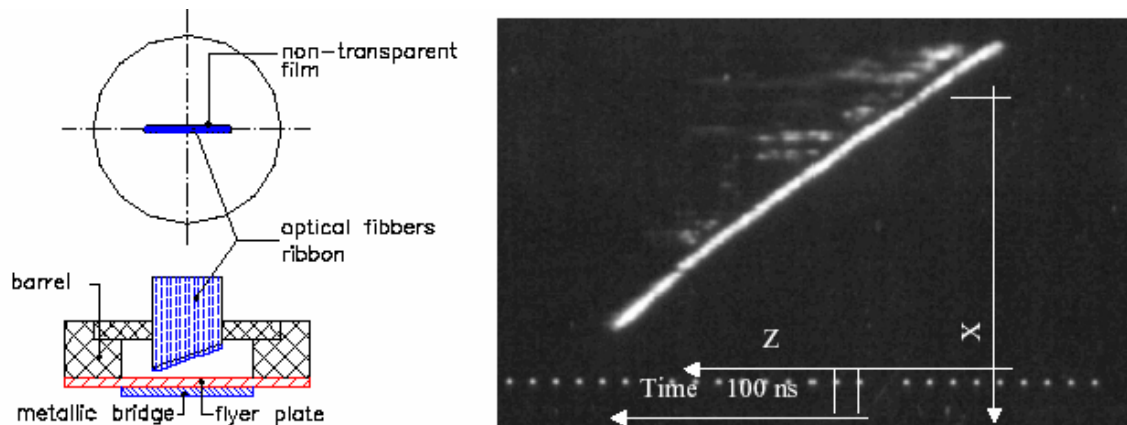


Figure 6. Experimental set-up and typical recorded signal of the flyer plate evolution inside the barrel.

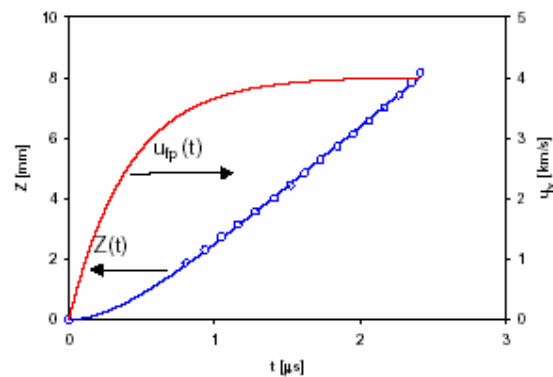


Figure 7. Experimental points (Z,t) ; curve fitting of displacement $Z(t)$ and velocity $u_{fp}(t)$.

2.3. Explosive characteristics. The PBX used (85% wt RDX, 11.5% HTPB and 3.5% DOS) has a density of 1.574 g/cm^3 , which corresponds to more than 99% TMD. The RDX has a bimodal particle distribution (75 wt% of $d_{50} = 96\mu\text{m}$ and 25 wt% of $d_{50} = 22\mu\text{m}$). The detonation velocity is 7.90 km/s , measured in cylindrical charges of 25 mm of diameter initiated by flyer plate impact. The detonation pressure is 24.4 GPa , measured by the shock attenuation method in PMMA barrier. The measured critical diameter, ϕ_c , in PVC confinement, is between 3.5 and 3.75 mm .

2.4. Shock to Detonation Transition Experiments. The experimental effort of the SDT work is to characterise the input pressure pulse, the shock to detonation distance Z_{SDT} and the detonation induction time t_d . To measure the initiation distance the optical fiber ribbon is placed, normal to the detonation wave propagation, inside the explosive. The experimental arrangement is presented in **Figure 8**. As the front of the shock/detonation waves cross the optical fiber a light pulse is generated and is recorded with a fast electronic streak camera. A cylindrical PVC tube, with 10 or 20 mm of height and 25 mm of internal diameter, confines the explosive samples. In the explosive top a PMMA barrier was attached, inside of which was also put the optical fiber ribbon. The fibers inside the PMMA barrier measure the velocity of the shock wave induced by the detonation wave. The flyer plate is Mylar with 0.350 mm thickness and 25 mm diameter.

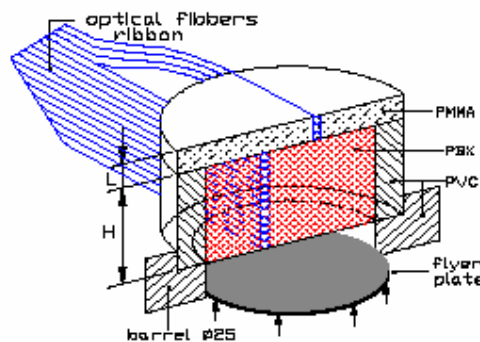


Figure 8. Experimental set-up to characterise the SDT.

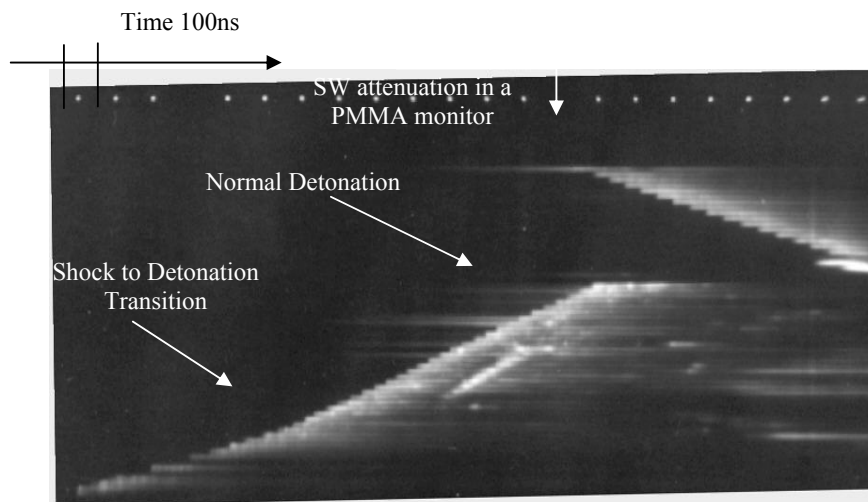


Figure 9. Typical photo-chronogram of the SDT, and the SW attenuation in an inert monitor.

A typical recorded photo-chronogram is presented in **Figure 9**. In that figure the initial shock wave velocity, the transition to the detonation wave and the normal detonation wave can be seen. Also visible is the shock wave attenuation inside the PMMA barrier. With this experimental method the evolution of the detonation wave front in a space-time diagram can be recorded “continuously”. In **Figure 10** the (Z,t)

diagram for two experiments in presented showing clearly the effect of different flyer plate velocities in the initiation process of our PBX.

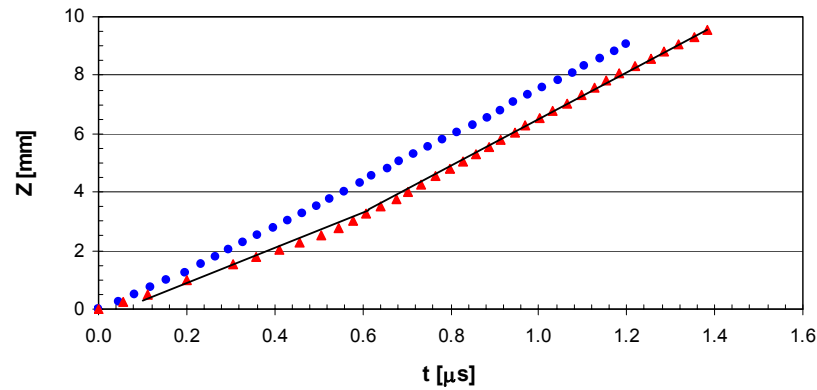


Figure 10. Diagram (Z,t) of the DW front propagation.

Considering the Hugoniot characteristics of the flyer plate material (Mylar) given by equation (2) (vd. LASL, 1980 (1)) and the shock impedance of the PBX in the initial zone of the shock wave propagation, it was possible to build up the Hugoniot characteristics of the PBX by the generally used mismatch method. Using four experimental points, the U_s-u_p relationship for our explosive is presented in equation (3). The measured initiation distance, as a function of the flyer plate velocity is presented in Table 5.

$$U_s = 2.356 + 1.601 u_p \text{ [km/s]} \quad \text{for } u_p < 2.62 \text{ km/s} \quad (1)$$

$$U_s = 2.070 + 2.081 u_p \text{ [km/s]} \quad \text{for } u_p < 1.70 \text{ km/s} \quad (2)$$

Table 5. Flyer plate velocity and detonation distance Z_{SDT} .

u_{fp} [km/s]	P_{ind} [GPa]	Z_{SDT} [mm]
2.71	9.1	3.25
2.84	10.3	2.25
2.84	10.3	3.00
2.94	10.8	2.50
3.64	14.9	1.50

The correlation of the sensitivity between our explosive and other PBXs based on RDX, obtained from the literature, is presented in Figure 11 showing the pressure values as a function of SDT distance on a logarithmic scale. The results of the explosive 84-16 (84% RDX-16% binder based on HTPB) with a density of 1.55 g/cm³ were obtained by C. Bélanger et. al., 1985, using an aluminium flyer plates to initiate their explosive samples. The experimental data for the PBX 9407 (density 1.60 g/cm³) 9405 (density 1.761 g/cm³) and 95-05 (density 1.711 g/cm³) were obtained from LASL, 1980. The sensitivity tests for those explosives were obtained by the Gap test, which induces in explosive samples a different pressure pulse profile compared to the flyer plate test.

Observing the results in Figure 11 the difference between our explosive 85-15 and the 84-16 explosive may be due to the experimental method used by Belanger et. al. 1985, to find the Z_{SDT} , that monitored only two events. Also the coarse particles (d_{50} about 650 μ m) used in the explosive 84-16 can explain the lower sensitivity of this explosive compared to the 85-15. The explosive PBX 9407, formed by fine particles (between 10-50 μ m) and the high porosity of that explosive, compared to the others, can also explain its high sensitivity. At last, our experimental results seems to be in agreement with the results of PBX 9407 and PBX 9405 due to the less mass content of RDX that induces less sensitivity.

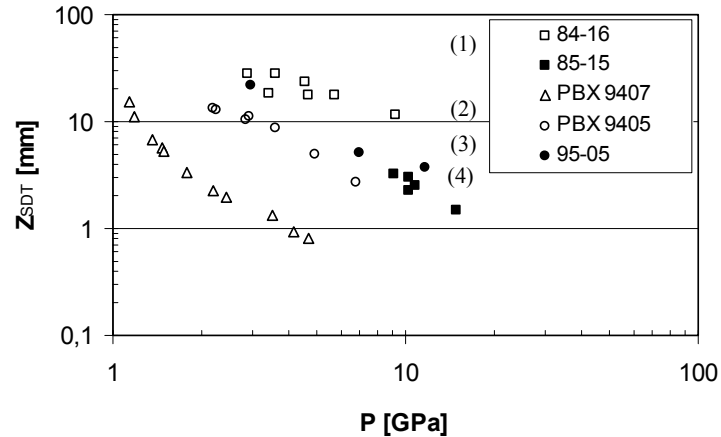


Figure 11. Correlation of the shock to detonation distance as a function of pressure pulse intensity for several PBX based on RDX, (1- Bélanger, C. et. al., 1985 and 2, 3, 4 - LASL, 1980-(2)).

3. SHOCK BEHAVIOUR OF THE SINGLE HMX-PARTICLES INSIDE DIFFERENT BINDERS AND PBX BASED ON HMX PARTICLES.

3.1. Shock behaviour of elementary PBX cells -“HMX crystal in binder”. L. Pedroso et al, 2005, tested micro-samples of three uncured energetic binders: a prepolymer designated PC13A (1,3,5-s-triazine ring with lateral chains derived from the opening epichlorohydrin ring), GAP and HTPB. They were encapsulated into cylindrical cells with 6 mm diameter, preliminary drilled in 1.8 mm thick lead plate. The cells with the prepolymers were then closed in the top and bottom with Kapton stack attenuator (KSA) and a Kapton stack monitor (KSM). KSA and KSM consisted of five 132.5 μm thick and six 62.4 μm thick Kapton films, respectively. For better optical resolution of the SW run in KSA and KSM, the micro-gaps between kapton films were filled with argon. The MFOPs, with two or three parallel rows and 10-12 optical fibers per row, were placed in contact with KSM for observation of the 6 central zone of the cells. A shock wave generator was applied for simultaneous shock loading of the three micro-samples. The characterization of the shock behaviour of the prepolymers in the vicinity of a HMX crystal was performed with the crystals, experimental setup and view of the micro-samples shown in Figure 12. The booster, KSA, KSM and confinement of the cells were similar to those used in the classic described experiment. Three single HMX large crystals were selected from a HMX-Class-3 particles, produced by DYNO Nobel, Norway. The crystals were fixed on the KSA surface by one of the rhomb planes using a microscopic amount of epoxy resin, as shown in Figure 12.

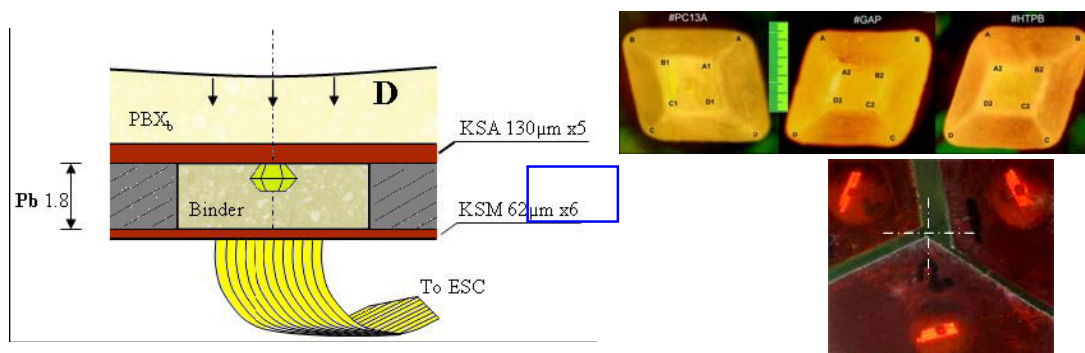


Figure 12 - Experiment with the micro-samples “HMX crystal in binder”, HMX crystals and experiment configuration.

The heights of the crystals in the z-axis, that is normal to A1B1C1D1 planes were 586, 617 and 546 μm for PC13A, GAP and HTPB micro-samples, respectively. The cells were then filled with the binders (prepolymers). The procedure of filling included vacuum treatment as in the previous experiment to avoid air bubbles. The streak record obtained shows the SW inputs to the cells identified by the light irradiation when SW crosses the interfaces KSA/crystals. The SW output from the prepolymers to KSM was clearly identified for GAP and HTPB. For PC13A, an extrapolation was made for the first Kapton film of KSM. The outputs of the reaction fronts from the crystals were identified by the local extinction of strong light recorded by fibers located in the projection of the terminal rhomb planes of the crystals. These results permit to calculate the mean velocities of SW run through the crystals and in the prepolymers, from the crystals up to KSM, as well as the pressure history $P_k(t)$ of shock field in KSM. The history $U_s(t)$ of shock fields in KSM is shown in Figure 13.

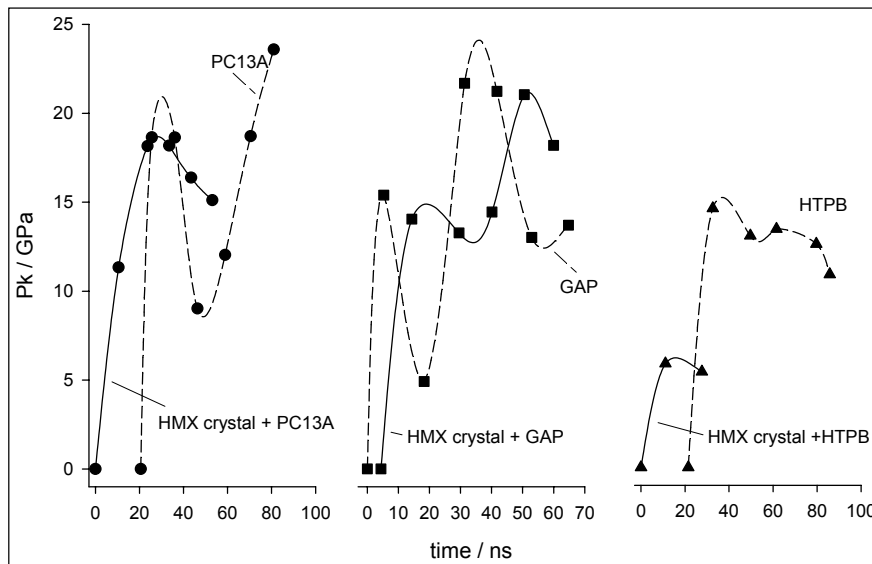


Figure 13 - $P_k(t)$ -diagrams of SW run in KSM obtained in the experiments with pure binders and “HMX crystal in binder”

Shock Hugoniot characteristics of HMX single crystals $\rho_0 = 1.9 \text{ g cm}^{-3}$, $U_s = 5.80 + 0.59 U_p$, were applied for the characterization of SW parameters in the initial phase of the crystal’s shock compression. When the initial SW (that in the terminal zone of the KSA has velocity and pressure of $4.89 \mu\text{m ns}^{-1}$ and 9.97 GPa , respectively) enters the single crystal, the transmitted shock front runs inside the crystal with velocity and pressure in the front of $4.46 \mu\text{m ns}^{-1}$ and 11 GPa , respectively.

3.2. Wedge Test of the PBX based on HMX

3.2.1. HMX particles and PBX formation

HMX-Class-3 particles, produced by DYNOL Nobel, Norway, were sieved to obtain numerous fractions of mono-modal particle size distribution. The pore-free PBX samples were composed of the formula “HMX 77/23 Epoxy”. The epoxy resin Araldite[®] was a binder of HMX particles. For elimination of probable micro-voids, the finished samples were subjected to vacuum treatment inside the chamber. Two PBXs, “#45” and “#420”, were composed of HMX crystals of narrow-size fractions $45 \mu\text{m} < d < 53 \mu\text{m}$ and $420 \mu\text{m} < d < 595 \mu\text{m}$, with mean sizes $d_{50} = 49 \mu\text{m}$ and $d_{50} = 508 \mu\text{m}$ respectively. The third explosive material “#420 & 45” was composed of a mixture of the $508 \mu\text{m}$ - and $49 \mu\text{m}$ -crystals in the mass ratio 3/1. Figure 14 illustrates the configuration of the finished test setup, developed by I. Plaksin et al, 2006, 2007. The acceptor samples have a prismatic configuration with the actual angle $\alpha \approx 16^\circ \pm 1^\circ$. Samples are encapsulated into the cells that were previously drilled out in the PVC wedge. From two actual sides, acceptor samples have been covered with the stacks of four $80\text{-}\mu\text{m}$ -PVC films, PVC stack attenuator (PVC SA) from one side and with the PVC stack monitor (PVC SM) from the other. In both SA and SM,

the PVC films were separated from each other by 5- μ m-air gaps. Both acceptors were separated from each other with a \sim 1.5-mm-wall composed of two PVC layers and one layer of 0.5-mm-lead. Such a wall configuration prevents interference between the reaction fields, within two samples, at actual tracking times.

3.2.2. Shock Hugoniot Characteristics of PVC and HMX Single Crystals

For both the Stack Attenuator (SA) and Stack Monitor (SM) standard 80- μ m PVC films of density $\rho_0 = 1.376 \text{ g/cm}^3$ produced by "Schwan STABILO" were selected. Figures 14, 15 illustrate the basic Shock Hugoniot characteristics "Shock Pressure vs. Shock Speed U_s " (LASL, 1980) of the PVC and the HMX single crystal mainly used for the experiments. Based on the linear approximations $U_p = a \cdot U_s - b$, we then described the functions $P(U_p)$ and $P(U_s)$ with application of the basic equation for shocked PVC, $P = \rho_0 \cdot U_s \cdot U_p$.

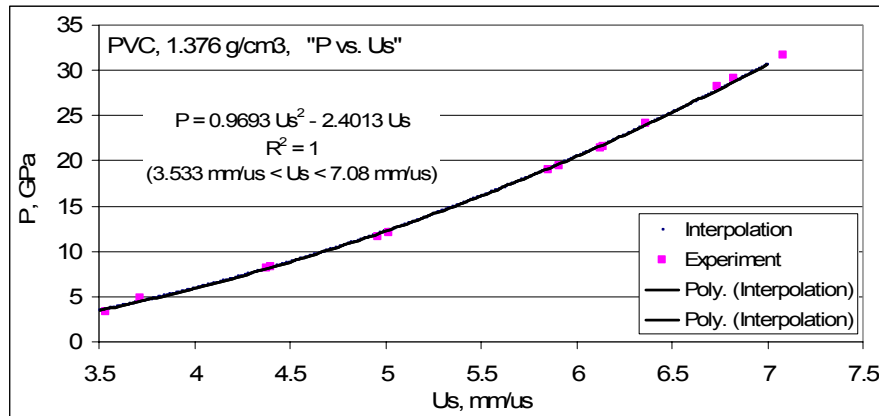


Figure 14 - Shock Pressure vs. Shock Front Speed, $P(U_s)$ for PVC.

For describing shocked HMX crystals, the experimental data (LASL, 1980, Hooks and Ramos, 2006) obtained in experiments with single β -HMX crystals of density $\rho_0 = 1.891 - 1.901 \text{ g/cm}^3$ was applied. The experimental points U_s - U_p have been approximated by the linear relationship $U_p = -2.0934 + 0.6349 \cdot U_s$ and then the functions $P(U_p)$ and $P(U_s)$ were obtained in the same way as for the PVC above. Figure 15 illustrate the approximation functions $P(U_p)$ and $P(U_s)$ applied for characterization of the initial shock state of HMX crystals when the crystalline HMX composite is subjected to shock entering from the stack attenuator.

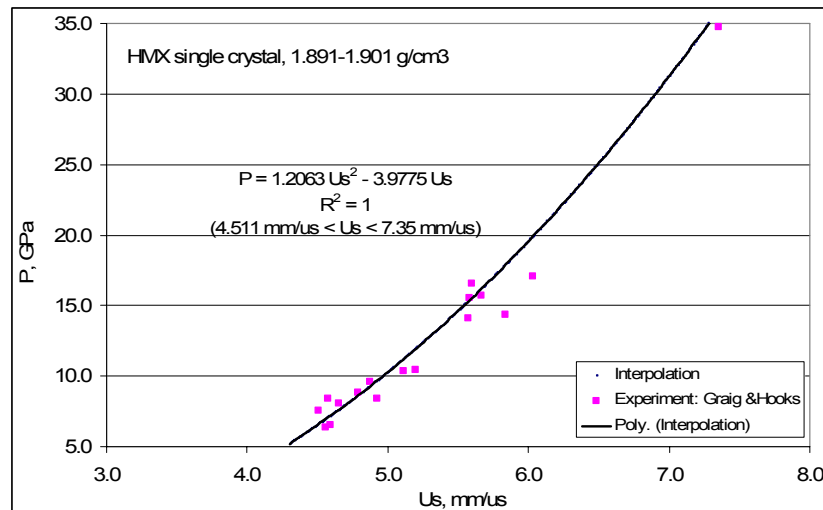


Figure 15 - Shock Pressure vs. Shock Front Velocity for single HMX crystal.

3.2.3. Wedge test configuration. Figure 16 illustrates the wedge test configuration used (I. Plaksin et al., 2006, 2007). Two acceptor samples of wedge configuration were placed between the stacks of four 80- μm -thick PVC films, PVC SA and PVC SM. The Multi-Fiber Optical Probes (MFOP) connected to the PVC SM provided tracking of reaction radiation, from the SW input up to the reaction or detonation front output from acceptor, and then the SW motion in the PVC SM. Acceptors were subjected to the shock caused by detonation of the 30-mm-long PBX charge of 20-mm x 30-mm cross-section. According to the calibration test, the $\sim 350\text{-}\mu\text{m}$ -PVC SA attenuates the induced shock up to 15.5 GPa. The shock begins to move in the HMX crystals with the initial speed $U_{S00} = 6.01 \text{ mm}/\mu\text{s}$ having the 19.7 GPa amplitude.

The shock induced processes inside the acceptor samples is analysed in coordinates “ z ”, “ x ” and “ t ” whereas the SW motion within the PVC stack monitor is considered in coordinates “ λ ”, “ δ ” and “ t ”. Here, “ λ ” is a hypotenuse of the wedge sample, “ δ ” refers to a run distance, “ t ” is a time taken from the initiation onset, and $z = \lambda \cdot \sin(\alpha)$ (vd. Figure 16).

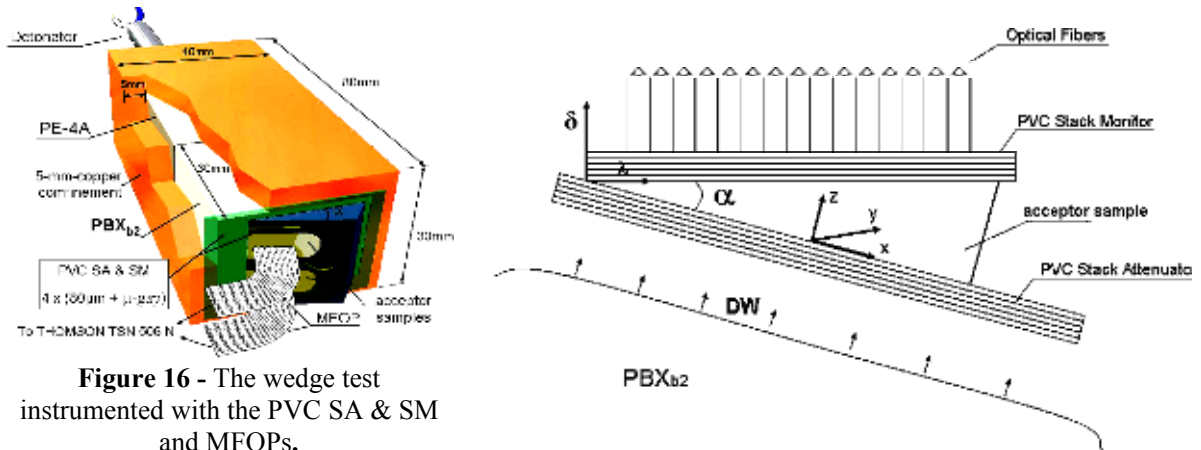


Figure 16 - The wedge test instrumented with the PVC SA & SM and MFOPs.

3.2.4. Wedge Test of the PBX “#45”, “#420” and “#420 & 45” based in HMX-particles.

Figures 17-19 illustrate streak camera records and the examples of the $\lambda(t)$ diagrams of shock propagation in PVC SM and the $z(t)$ diagram of reaction front motion in PBX respectively. Distance “ z^* ” ($z = \lambda \cdot \sin(\alpha)$) and time “ t^* ” to detonation, are identified on the change of slope in the $z(t)$ diagram. Local velocities of shock front motion through the samples, $D = dz / dt$, are presented in Figure 20 as a function of time. The oscillating mode of $D(t)$ curves is evidence for the existence of “galloping” regime of front motion that takes place independently on HMX grain sizes.

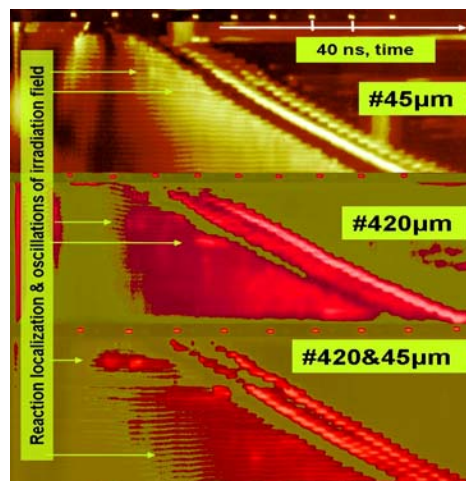


Figure 17 - The camera streak records of the shock induced process in three PBX based in HMX.

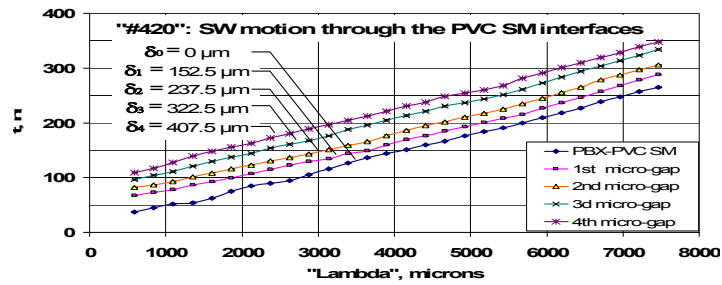


Figure 18 - The $\lambda(t)$ diagrams of shock front output from the acceptor sample (“ δ_0 ”) and its following motion through the micro-gaps of PVC SM; obtained in experiment with PBX “#420”.

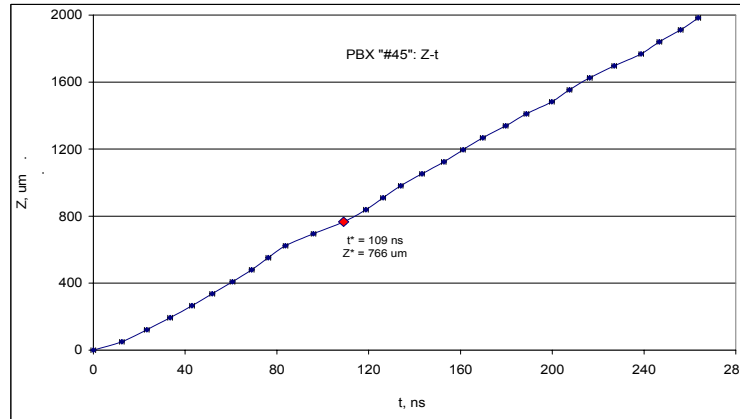


Figure 19 - The $(z-t)$ -diagram of the reaction front motion in PBX “#45”. The symbols “ t^* ” and “ Z^* ” mean time and distance to detonation.

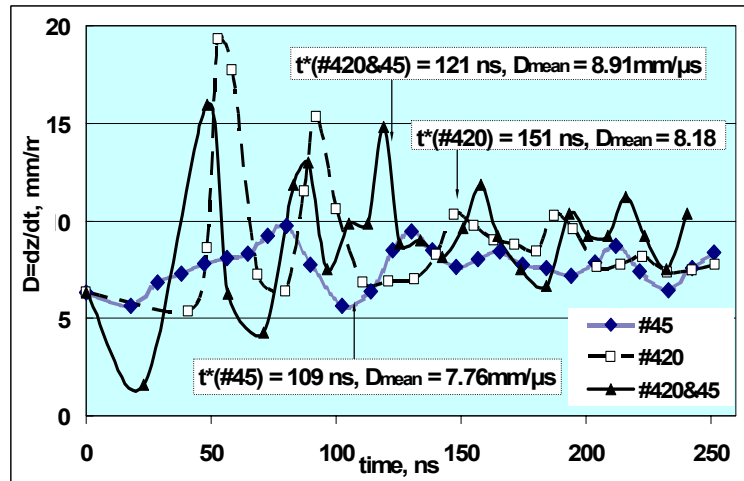


Figure 20 - The local velocity of front motion within the PBX-acceptors as a function of time. The symbols “ t^* ” and “ D_{mean} ” mean time to detonation and mean detonation velocity in “ $mm/\mu s$ ”.

The SDT includes 2 – 3 giant oscillations followed, at $t > t^*$, by series of less intense and more regular oscillations, where $D_{mean} = const$. The $D(t)$ oscillations are attended by oscillations of the reaction light intensity that are clearly indicated in streaks (see Figure 17). The smaller the HMX grains, the smaller are the amplitudes of oscillations and the localization scale in the DRZ.

The $\lambda(t)$ diagrams allow determination of the shock front isochrones in coordinates “ λ ” and “ δ ” and then building up of stream lines, or directions of the shock’s local path in the PVC SM. Figure 21 illustrates a series of shock front isochrones corresponding to 10-ns-intervals of shock front motion within the PVC SM. The patterns of isochrones demonstrate a change of the geometrical shape of shock front at the SDT.

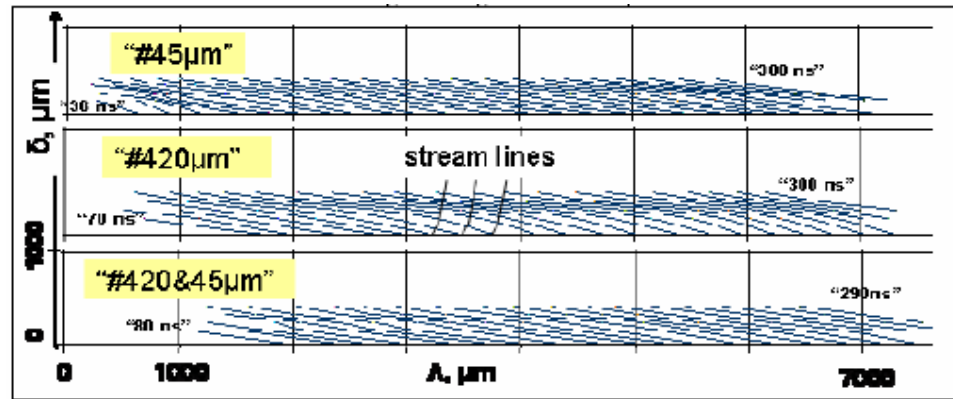


Figure 21. Patterns of shock front isochrones corresponding to the 10 ns intervals of shock front motion within the PVC SM.

These results prove the capability to measure of the shock front run along stream lines precisely allowing the establishment of the vector field of shock velocities $\{Us(\lambda, \delta, t)\}$. Then the stress vector field $\{P(\lambda, \delta, t)\}$ can be simply determined through the shock Hugoniot polynomial $P(Us)$. Fragments of the shock velocity vector field $\{Us(\lambda, \delta, t)\}$ and the shock stress vector field $\{P(\lambda, \delta, t)\}$ are presented, as an example, in Figure 21. The points in the $Us(t)$ and $P(t)$ profiles refer to the mean speed and mean shock pressure at each 10-ns-interval of shock front motion; the front local motion is considered along the stream line crossing two adjacent isochrones.

3.2.5. Discussion

In previous papers, the effect of reaction front radiation (or “Radiation Impact”) was reported (I. Plaksin et al., 2004, 2005, 2006, 2007). This plays an important role in the SDT mechanism. The radiation impact implies radiation heating of the PBX layer, ahead of the reaction spot, through the absorption of the reaction photons. The effect of the reaction spots radiation upon the DRZ structure is illustrated by the dependence of radiation absorption on the HMX grains sizes. In the present experiments, the effect of the radiation absorption emerges in histories of the $\{Us\}$ and $\{P\}$ fields. This can be best illustrated by the $Us(t)$ and $P(t)$ profiles obtained in the fine-grained PBX “#45”. Beyond the SDT, the classic chemical spike (P (“ $t_0=130$ ns”) rapidly converts into a double-wave configuration such as “*ramp precursor + major wave*”. The ramp precursor points to formation of the preheated layer ahead the major front caused by front radiation, wherein the HMX crystals suffer thermal expansion, phase transformations, melting and partial reaction.

4. CONCLUSIONS

The use of Multi-Fiber Optical Analyzer allows simultaneous registration of the dynamic and profile characteristics of the induced shock wave, by the registration of self-radiation of shocked materials. An experimental case study of single HMX particles, inside different binders, was tested. PBX samples, fabricated from RDX and HMX particles, were studied in Shock-to-Detonation Transition (SDT) experiments, respectively generated from a flyer impact and under the wedge test configuration. The simultaneous probing of radiation field, emitted from the shock front and the Chemical Reaction Zone (CRZ) structure, when occurs, allows the precise study of energetic particles and its derivate PBX behaviour under shock conditions.

Acknowledgements

Portuguese MoD, allowing the participation in the WEAG CEPA-14 Project “*ERG-114.009: Particle Processing and Characterization*”, mainly supported this work. Authors gratefully acknowledge the technical support of research groups from the ICT - Fraunhofer Institute of Chemical Technology (Germany) and TNO Prins Maurits Laboratory (the Netherlands) who delivered the processed HMX and RDX particles. The authors want also to acknowledge *ADAI-Ass. para o Desenv. da Aerodinâmica Industrial* for the support of this research area.

REFERENCES

- BELANGER, C., PELLETIER, P. e DROLET, J.F., 1985. “Shock sensitivity study of the curable plastic bonded explosives”, in *8th International Symposium on Detonation*, pp. 361-368, Albuquerque, NM, USA, 15-19 July.
- CHEN, C., SHUAN, J. and FENG, I., 1993. “Design of an inert material type plane wave generator”, *Propellants, Explosives and Pyrotechnics*, vol. 18, pp. 139-145.
- CIBA SPECIALTY CHEMICALS, 1997 a). “*Araldite AY 103*”, Ficha de segurança nº 0092795, Ciba especialidades químicas, Porto, Portugal.
- Hooks, D. E. and Ramos, K. J., 2006. “Initiation Mechanisms in Single Crystal Explosives: Dislocations, Elastic Limits and Initiation Thresholds”, in *Proc. of 13th Symp. (Int.) on Detonation*, Norfolk, VA, 23-28 July, Paper IDS 067.
- LASL, Shock Hugoniot Data, 1980 (1), ed. by S. P. Marsh, Univ. California Press, Berkley.
- LASL, Explosive Property Data, 1980 (2), ed. by T.R. Gibbs and A. Popolato, Univ. California Press, Berkley.
- MENDES, R., PŁAKSIN, I., RIBEIRO, J., AND CAMPOS, J., 1996 “Electrical explosion of the aluminium foil behaviour of explosions products in the process of flyer plate launch,” in *Shock Waves in Condensed Matter*, St Petersburg, Russia, Set. 2-6.
- MENDES, R., PŁAKSIN, I. AND CAMPOS, J., 1997, “Single and two initiation points of PBX,” *10th Biennial International Conference of the American Physical Society Topical Group on Shock Compression in Condensed Matter*, edited by S. C. Schmidt et al., AIP CP 429, NY, 1998, pp. 715-718.
- MENDES, R., CAMPOS, J. AND PŁAKSIN, I., 1998 “Double initiation and Mach formation in PBX,” in *eleventh International Symposium on Detonation*, Aspen, CO, Aug 29- Set 4.
- MENDES, R., 2000, “Iniciação e detonação de explosivo plástico de RDX”, Phd. thesis, DEM-FCTUC, Coimbra.
- MENDES, R., CAMPOS, J., PŁAKSIN, I. AND RIBEIRO, J., 2001. “Shock to detonation transition in a PBX based on RDX”, *Proceedings of the 32th ICT-Conference*, Karlsruhe, Federal Republic of Germany.
- PEDROSO, L. M., PŁAKSIN, I., SIMÕES, P., DIREITO, J., CAMPOS, J. AND PORTUGAL, 2005 . “A Triazine Prepolymer Energetic Binder - Shock Behaviour and Detonation Performance in the Scale of HMX Grain Size”, *Proceedings of the 36th ICT-Conference*, Karlsruhe, Federal Republic of Germany, P-169.
- PŁAKSIN, I., MENDES, R., CAMPOS, J. AND GOIS, J., 1997 “Interaction of double corner turning effect in PBX,” *10th Biennial International Conference of the American Physical Society Topical Group on Shock Compression of Condensed Matter*, edited by S. C. Schmidt et al., AIP CP 429, NY, 1998, pp. 755-758.
- PŁAKSIN, I., CAMPOS, J., MENDES, R., RIBEIRO, J. AND GÓIS, J., 1999, “Mechanism of detonation wave propagation in PBX with energetic binder”, *11th Biennial International Conference of the American Physical Society Topical Group on Shock Compression of Condensed Matter, Co, USA*, edited by M. D. Furnish et al., AIP CP 505, NY, 2000, pg. 817-820.

- PLAKSIN, I., CAMPOS, J., RIBEIRO, J., MENDES, R. AND PORTUGAL, A., 2000, "Detonation Study of PBX Micro-samples", in *Shock Waves in Condensed Matter*, St Petersburg, Russia, Oct. 2-6.
- PLAKSIN, I., CAMPOS, J., RIBEIRO, J., AND MENDES, R., 2001, "Irregularities of Detonation Wave Structure and propagation in PBX", *Proceedings of the 32th ICT-Conference*, Karlsruhe, Federal Republic of Germany.
- PLAKSIN, I., DIREITO, J., CAMPOS, J. AND COFFEY, C.S., 2004 "Kinetics Diagrams at Shock Ignition of PBX and Non-Ideal Explosives". *International Conference on New Models and Hydro-codes for Shock Wave Processes*. Maryland University, May 16-21, MD, USA.
- PLAKSIN, I., CAMPOS, J., RIBEIRO, J., MENDES, R., GOIS, J. AND DIREITO, J., 2004. "Birth and Death of the PBX' Detonation in a Mezzo-Scale. Effect of the Grain Sizes and Binder' Nature in Ignition and Failure of Detonation". *Proceedings of the 35th ICT-Conference*, Karlsruhe, Federal Republic of Germany, June 29 – July 2, Paper "V24".
- PLAKSIN, I., DIREITO, J., COFFEY, C. S., CAMPOS, J., RIBEIRO, J., MENDES, R., KENNEDY, J., 2005. "Meso-scale Probing of CRZ Structure in PBX: DW Oscillations from Ignition up to Failure", in *Shock Compression of Condensed Matter-2005*. AIP Conference Proceedings 845, edited by M.D. Furnish, M. Elert, T.P. Russel and C. White, pp.1102 - 1105.
- PLAKSIN, I. AND DIREITO, J., 2006. "Relationship of Grain Size to the Shock initiation Process in the HMX-based Granular Explosives". *1st Report on Statement of Work under the Contract SC-IP 050303, NSWIH's Purchase Order N00174-05-M-0085*. University of Coimbra, August.
- Plaksin, I., 2006. "Interrelation between the Grain Size and the Shock Initiation Process in the HMX Based Granular Explosives". *2nd Report on Statement of Work under the Contract SC-IP 050303, NSWIH's Purchase Order N00174-05-M-0085*. University of Coimbra, January 2006.
- PLAKSIN, I., C. S. COFFEY, R. MENDES, J. RIBEIRO, J. CAMPOS AND J. DIREITO, 2006. "Formation of CRZ 3D Structure at SDT and at Shear Initiation of PBX: Effects of Front Irradiation and Reaction Localization in HMX Crystals" in *Proc. of 13th Symp. (Int.) on Detonation*, Norfolk, VA, 23-28 July, pp 319-330.
- PLAKSIN, I., RIBEIRO, J., MENDES, R. , CAMPOS, J., ALMADA, S. AND GOIS, J., 2007. "Determination of Shock Sensitivity of PBXs through Measurements of Radiation Intensity from the Reaction Front Surface", in *Proceedings of the 38th International Annual Conference of ICT "Energetic Materials: Characterization & Performance of Advanced Systems"*, June 26-29, Karlsruhe, Federal Republic of Germany, P-145.
- PLAKSIN, I., C. S. COFFEY, 2007 (2). "Shock initiation process of PBX", to be published in *Proc. of International Conference of the American Physical Society Topical Group on Shock Compression of Condensed Matter*.
- RIBEIRO, J., PLAKSIN, I., CAMPOS J., MENDES, R. and GÓIS, J., 2000. "Process of shock attenuation inside a hollow glass microsphere/polymeric composite material", *Shock Compression in Condensed Matter-1999*, edition M. Furnish, L. Chhabildas e R. Hixson, AIP Conference Proceedings 505, New York, USA, pp. 559-562.
- RIBEIRO, J., CAMPOS, J, 2003. "Shock behavior of syntactic foams", *Proc. of 1st Light -Weight Armour Group Workshop - Manufacture, testing and utilization of light-weight armour materials*, University of Aveiro, 5th of September
- THOUVENIN, J., 1965. "Effect of a shock wave on a porous solid", *Fourth International Symposium on Detonation*, ACR-126, Office of Naval Research, Department of the Navy, Washington DC, USA pp. 258-265.

17th DYMAT Technical Meeting, 2007, Cavendish Laboratory, Cambridge

Mechanical Properties and Their Effect on Energetic Material Sensitivity

W.G. Proud, D.M. Williamson, D.J. Chapman, H. Czerski and J.E. Field
*Fracture and Shock Physics, SMF Group, Cavendish Laboratory, J.J. Thomson Avenue,
Cambridge, CB3 0HE, United Kingdom.*

Polymer-bonded explosives (PBXs) are being increasingly used as energetic fillings and components in many systems. They are perceived as more chemically and mechanically stable than traditional fillings such as RDX/TNT. They are castable into predetermined shapes, machinable and can be used as structural components. These materials are now undergoing extensive characterisation to ensure they comply with both the legal and technical requirements in energetic systems.

It is well known that polymers display complex non-linear behaviour. The understanding of PBX systems involves areas as diverse as polymer chemistry, chemical compatibility, mechanical properties, impact tests, and thermal stability. In this paper aspects of energetic material response are outlined which are relevant to the understanding of materials sensitivity.

INTRODUCTION

For many years, the ignition and growth of reaction in energetic materials has been the subject of sustained research effort[1-13]. In the past decade, an increasing driver for these studies has been the safe handling and transport of energetic systems. One aspect that has received much attention is the formation of hot-spots, regions where the stimulus supplied to the energetic material causes a local heating sufficient to produce chemical reaction. Once formed the hot-spot can grow, link to other hot-spots, and cause a general deflagration which can then lead to detonation. However, if the thermal losses from a hot-spot exceed the heat production from reaction then the hot-spot is thermally quenched. The hot-spots that lead to sustained reaction are termed critical and those which are thermally quenched are termed sub-critical.

Many mechanisms have been proposed for the formation of hot-spots. The mechanisms for which a wide range of empirical evidence exists are relatively few. These include bubble or void collapse[14], shear band formation[15], friction[16], fracture[17], electrical discharge[18] and viscous flow. It is rare that any one of these processes occurs alone, generally several mechanisms will operate at once, the overall effect being additive. Of these mechanisms viscous flow generally tends to operate in a subsidiary role, as the material heats up and is more likely to react, the resistance to flow, hence energy deposition rate, tends to fall off[19]. Electrical discharge is a well-defined mechanism in terms of the energy requirements and safety limits for this have long been established; this paper will make no further reference to this mechanism,

Of the remaining main mechanisms, fracture is interesting as the release of stored mechanical energy at a crack tip can cause substantial local heating. However, there is much evidence to show that splitting or even extensive fragmentation of a single crystal of a sensitive primary explosive does not deposit enough energy to cause reaction. However, if a polymer-bonded explosive (PBX) is considered then, if a tough polymer is used the fracture energy is much higher and may result in hot-spot formation. Similarly if the PBX is taken below the glass transition temperature of the binder then this may result in the sensitisation of the material as the stored energy before fracture can be much higher. In addition, fracture is accompanied by the production of gases from the new surfaces and also creates new surfaces that can rub together.

Void or bubble collapse is a very important mechanism as the gas in the void can heat rapidly when collapsed. As well as the adiabatic heating of the gas trapped in the void, material can also jet across and strike the opposite side of the void. Additionally the materials around a collapsing void is heated due to elastic-plastic effects.

Friction is an obvious mechanism, but again it must be pointed out that as the rubbing surfaces become hot, generally they become softer and flow more easily, thus reducing the rate of energy deposition. This effectively produces a plateau in the energy deposition rate. However, if gas or voids become entrained in the flowing material this can again form local regions for energy deposition. The same phenomena may happen for ignition from shear bands.

All these mechanisms rely on structural inhomogeneities at which the energy can concentrate. The early research of Bowden and Yoffe defined the typical size of the inhomogeneities required for the formation of hot-spots. These limits are 0.1 - 10 μm for a stimulus of time duration 10 μs - 1 ms, giving a temperature of 700 K[2, 20, 21]. It must be emphasised that these are the typical sizes, other scales may be important in particular circumstances; if, for example the temperature is high, the size and time can be lower.

Thus the feed stock and the processes used in produced a practical energetic material are critical in determining the material sensitivity. In figure 1, a micrograph of a polymer bonded system is shown. The exact material is not important, the image shows in a small field of view a variety of structural features that are responsible for hot-spot formation. In the figure large angular crystals can be seen which have inclusions and cracks. In several places crystals are in close proximity and are indenting into one another.

The polymer binder itself may not be homogeneous. Atomic force microscopy studies[22] have shown that polymers in some systems may have inclusions of fine-grained energetic material as well as softer regions where polymerisation initiators are concentrated or incomplete polymerisation has occurred.

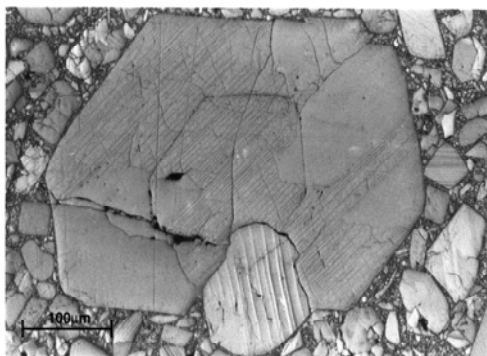


Figure 1. Optical micrograph of a polymer bonded explosive

This is sometimes referred to as ‘dirty’ binder, implying that the fine material should not be present. However, this material is either part of the energetic feed-stock or ground from the larger crystals during the mixing and pressing associated with the production process. Indeed, scanning electron microscope (SEM) images of raw RDX crystals show significant quantities of fine-grained material adhering to the surface of larger crystals. After sieving, some large ‘crystals’ have been observed which are agglomerations of finer particles.

It has been noted many times that the “fines” can influence both mechanical and ignition properties. In this paper, recent results are presented showing behaviour which emphasises the sometimes subtle interplay of the hot-spot mechanisms applicable to PBX systems.

THE EFFECT OF CRYSTAL STRUCTURE

Polymer-bonded explosives have explosive loading in the range 66-95%. Studies on the crystals reveal the timescales and synergies involved. Research has indicated that the presence of defects in the explosive feed stock can be related to the sensitivity of the full PBX system.

The grain size of a material is intimately linked to its sensitivity[23, 24]. Gap tests are widely used as a measure of shock sensitivity. Samples of pentaerythritol tetranitrate (PETN), either submicron or of conventional grain size, were supplied by ICI Nobel Enterprises of Ardeer, Scotland. The fine-grained material had a primary particle size of $\sim 1 \mu\text{m}$ and was prepared by a proprietary process. The conventional grain sized material was $180 \mu\text{m}$. The materials were pressed into polymethylmethacrylate (PMMA) holders, 25 mm long, 25 mm in diameter with a central bore of 5 mm. The incremental pressing used a step height of 0.5 mm resulting in a very homogeneous column. The experimental arrangement is shown in figure 3(a). A PMMA gap is placed between the column and a C8 detonator placed on top[25]. All contacting surfaces were coated in a thin layer of silicone grease in order to allow good acoustic transmission between the layers. The length of the pressed column was observed using a Hadland 790 with a streak speed of $10 \text{ mm} / \mu\text{s}$.

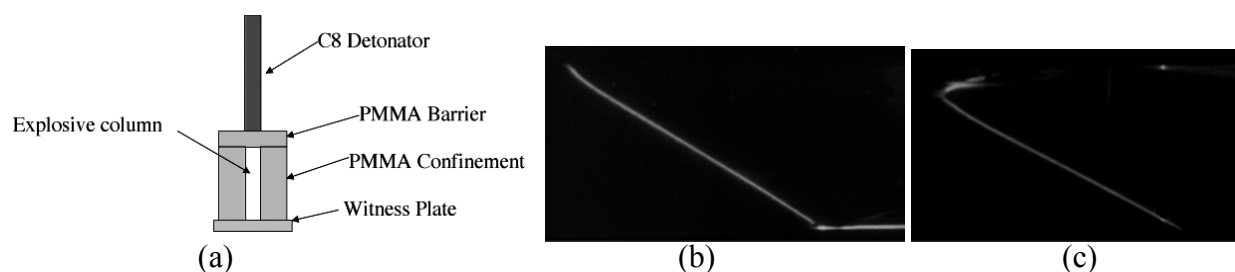


Figure 3. Gap testing (a) Experimental arrangement. Streak records of fine-grained PETN 90% TMD (b) 3.53 mm gap (c) 3.67 mm gap,

Selected streak records from experiments on 90% TMD PETN fine-grain size are shown in figure 3 (b) and (c). The gaps were 3.51, 3.67 mm. It can be seen in 3(b) that the detonation was prompt and slightly overdriven. The detonation velocity became steady within 5 mm of column length. In the second image, there is hooking due to the detonation starting a short distance down the column indicating that the detonation almost failed. For a gap 3.71 mm thick, no detonation occurred.

A similar series were conducted for conventional grain size material where the gap thickness for failure was shown to be 5.54 mm of PMMA. This clearly shows that the finer grained material is *less* shock sensitive in this regime. To get a quantitative value for the stress levels PVDF gauges (Dynasen) were placed between a PMMA gap and a PMMA block 25 mm thick. A 5.54 mm gap corresponded to a stress level of 2.1 GPa; 3.67 mm to 4.1 GPa[26]. Therefore in this experimental arrangement the smaller grain size material is much less sensitive.

However, the situation is not so simple. A further series of experiments involving laser driven fliers $\sim 5 \mu\text{m}$ thick, 1 mm in diameter travelling at velocities up to $5 \text{ mm} \mu\text{s}^{-1}$ showed the fine grained material to be much *more* sensitive to impact than the conventional grained material[27].

The explanation for this we suggest lies in the fact that the formation of reaction sites is a function of size, temperature *and* time. The laser driven flier induces shock pulses of nano-second duration and such compressive pulse can encompass several grains and voids in the fine-grained material. Reaction initiated at the surface of a small-grain rapidly consumes the whole

grain. However, for the larger grain sizes the shock pulse is substantially thinner than the width of a crystal; the crystal size ensures that any surface ignition is more easily quenched by the larger thermal mass.

Internal voids within a crystal are obvious sites for ignition[28, 29]. It would seem logical to assume that crystals with a high void content should be more sensitive[30]. There are several studies to this effect. In order to investigate this, a combination of high-resolution x-ray tomography and gap testing has been applied to RDX from a number of commercial suppliers.

In this study[31], we investigated shock sensitivity differences between unpressed granular beds of RDX. The size classes, e.g. class 5, are the industry-recognised standard for these materials. Our sample set comprises seven batches from three manufacturers, in two size classes, produced by both Bachmann and Woolwich processes. The class 1 samples are 1a-c. In order to examine both surface and internal morphology, we have used Environmental Scanning Electron Microscopy (ESEM), optical microscopy and mercury porosimetry. Shock sensitivity was assessed using the small scale gap test.

In order to test the RDX crystals in the as-supplied state, the charges were not pressed but were poured into confinements in small increments and tapped. The differences in final density were only 1-2% for the medium size class. For the smallest size class, tapped densities for different batches ranged from 32% to 49% of the theoretical maximum density. Repeating some of the sensitivity tests with samples pressed to 50% showed no change in sensitivity

Samples were placed in index-matched fluid, and typical crystals are shown in figure 4. Black areas on the photographs arise from the refractive index mismatch between the crystal and the contents of the internal closed voids. This allows the identification of internal voids with diameters of 2 μm and above. Crystals were inspected and the numbers of voids in different size classes were counted. The size classes used were <5 μm , 5-15 μm , 15-50 μm and >50 μm . For the smallest crystals, size classes were not appropriate, and instead the total number of voids in each crystal large enough to be resolved was counted. Most voids were almost spherical in shape.

It was found for the smallest size class, the most sensitive crystals have only 1 or 2 voids per crystal, although a few crystals with many voids (up to 20) skew the average. For each size class studied, we observed that the most sensitive crystals contained the fewest internal voids with the difference in critical stress being of the order of 50%. The results for class 1 are summarised in table 1. This result was surprising and the series was run again to double-check. This suggests that either the void content is irrelevant on this time scale and size scale, however, in view of the large volume of literature correlating void content with sensitivity, it seems that for RDX in these gap tests, factors other than void content dominate. It may be that the crystals with voids are structurally weaker and so less energy is accumulated in elastic strain prior to failure. The main point from this research was that voids are not the sole determining factor in sensitivity. A fuller account of this research can be found on [32]

Sample label		1a	1b	1c
Crit. gap/mm		7.9	8.5	9.3
Av. no. of voids	35	21	9	
Av. crystal size/ μm	237	177	165	

Table 1. Void data from optical microscopy for size class 1.

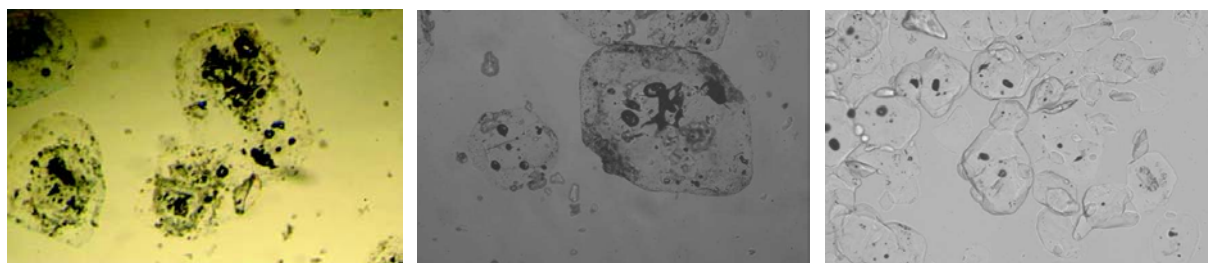


Figure 4. Typical crystals of class 1 material. They are shown in order from lowest to highest sensitivity: 1a, 1b, 1c. Magnification is the same in all images and the field of view is $\sim 500 \mu\text{m}$

In addition to conventional and electron microscopies, X-ray tomography is now capable of clearly resolving structures of $10 \mu\text{m}$ size[33]. This allows the interior of optically opaque systems to be probed. This is invaluable for the compaction of two-phase composites and granular beds. Analysis of such data allows a quantitative measure of the nature and extent of structural inhomogeneities such as voids and fractures. Figure 5(a) shows a pore in a large single crystal of RDX while figure 5(b) shows a section through a granular bed of HMX contained in a PMMA cylinder. In the granular bed, many crystals can be seen which have internal fractures and voids.

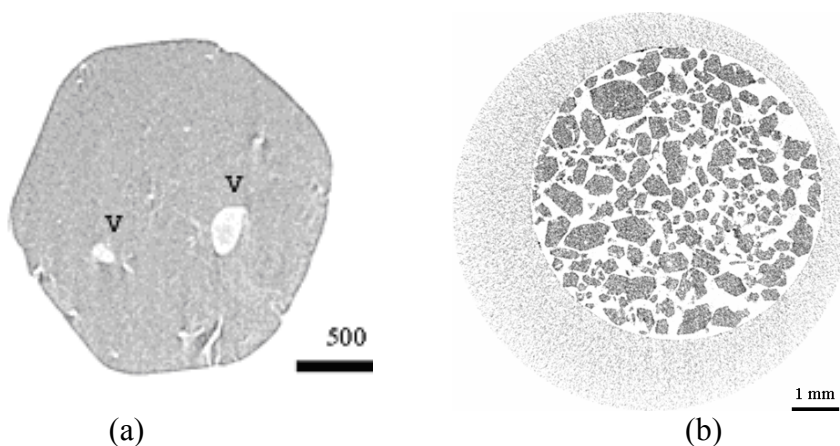


Figure 5(a) Tomograph of a large single crystal of RDX with two large voids, 'v' indicates the position of a void (b) Tomograph of a bed of HMX.

POLYMER-BONDED EXPLOSIVE SYSTEMS

In PBX systems, despite the high loading of energetic the mechanical response is strongly influenced by that of the binder[34] [35] [36]. The modulus of the binder may be 1000 times lower than that of the crystals. This means that the binder takes up virtually all of the imposed deformation, which has a strong influence on the strain and strain rate localisation in the material. In this section, we deal with strain rates of $10^3 - 10^4 \text{ s}^{-1}$ i.e. those associated with Hopkinson Bar systems.

We have shown that the size of the crystals has a major effect on the stress strain relationship of the PBX material[37]. An example is given in figure 7(a) for a 66% ammonium perchlorate (AP): 33% hydroxy-terminated polybutadiene (HTPB) system. The flow stress can be related to the square root of the grain size, this relationship is empirically determined but is similar to many found in fracture mechanics.

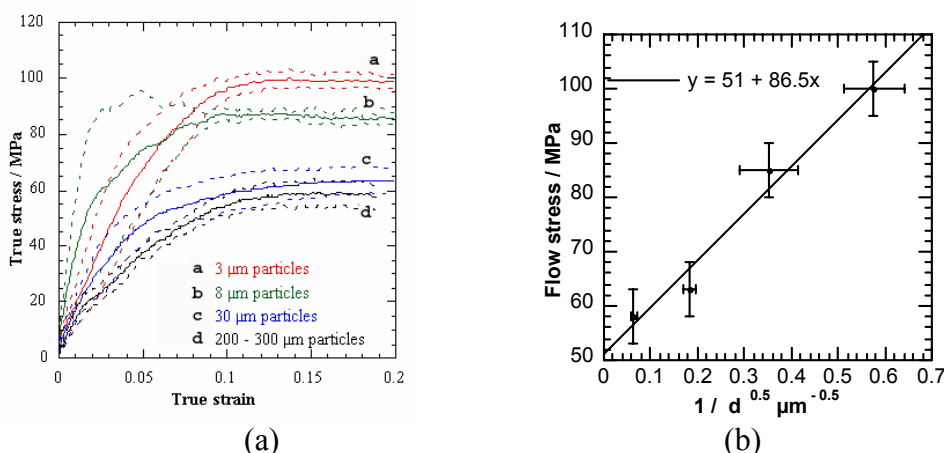


Figure 7. (a) The stress strain response of an AP:HTPB composite with varying grain size. (b) The dependency of the flow stress on the crystal size.

Polymer-bonded systems are also strongly dependant on temperature and age[38]. In figure 8, the results of changing the temperature of the composite is shown. The material used was an inert simulant, a 75% caster sugar: 25% HTPB. At 20 °C, the material starts to flow at 0.05 strain. Reducing the temperature to 0 °C increases the strength slightly but does not affect the shape of the curve. However, at -20 °C the strength has increased dramatically and increases further by -40 °C. At -60 °C the first sign of strain softening after yield is seen; this is more dramatic at -80 °C. Finally at -100 °C the material is behaving in a brittle fashion[39] [40].

The material was characterised using X-ray tomography. In figure 9 a small sample was cut from a pristine larger specimen[41]. The side length of the image is 4 mm, within sugar crystals pores can be seen.

Altering the temperature of the specimen is, for many polymers, qualitatively equivalent to changing the strain rate. Recent studies [42] on a HMX composition have given this a quantitative basis. It was noted that the material changed colour during the deformation from a translucent form to a milky colour. This was associated with debonding of the crystal from its binder. This process, at room temperature started at strains of 0.15 and continued until 0.3 strain. After the experiments the sample recovered and residual stain was of the order 3%. However a volume increase of 16% was found compared to the pristine samples.

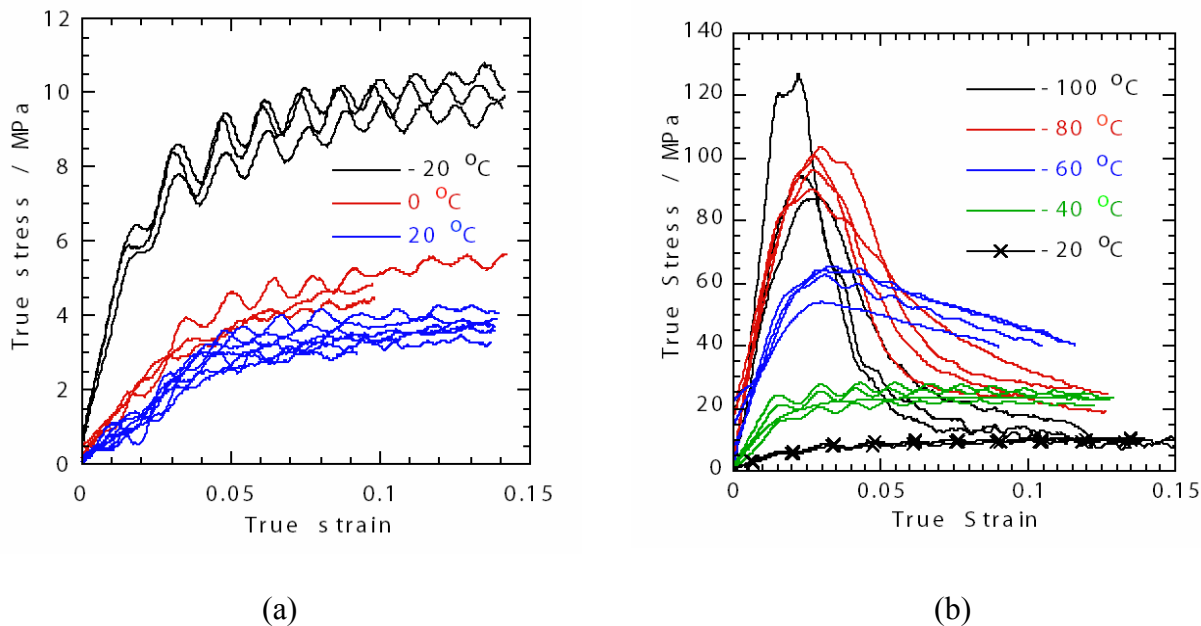


Figure 8 (a) Stress strain curves taken between -20 and $+20$ °C (b) Stress strain curves from -100 to -20 °C.

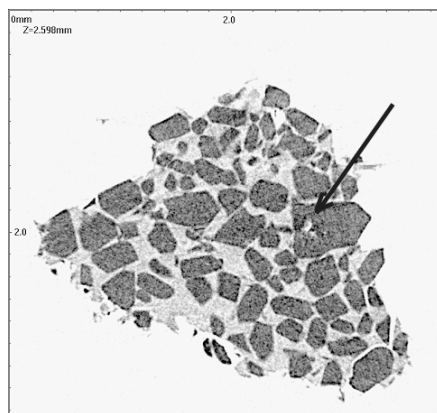


Figure 9. X-ray tomograph of a PBS sample showing a void in a sugar crystal (arrow).

X-ray tomography of samples, subject to loading in an Instron, showed that debonding of the polymer from the binder is the main failure mechanism in the material at the low rates. This can be seen in Figure 10. This damage has occurred at stresses well below that required for the fracture of sugar (~ 50 MPa). Overall this tearing of the binder is significant as the rapid strain softening seen at low temperatures is often associated with particle-particle interaction. Such interaction would allow the frictional hot-spot mechanisms to come into play between particles as well as due to internal crystal fracture. This debonding would also open up pathways for hot products gases to flow through the sample causing widespread reaction.

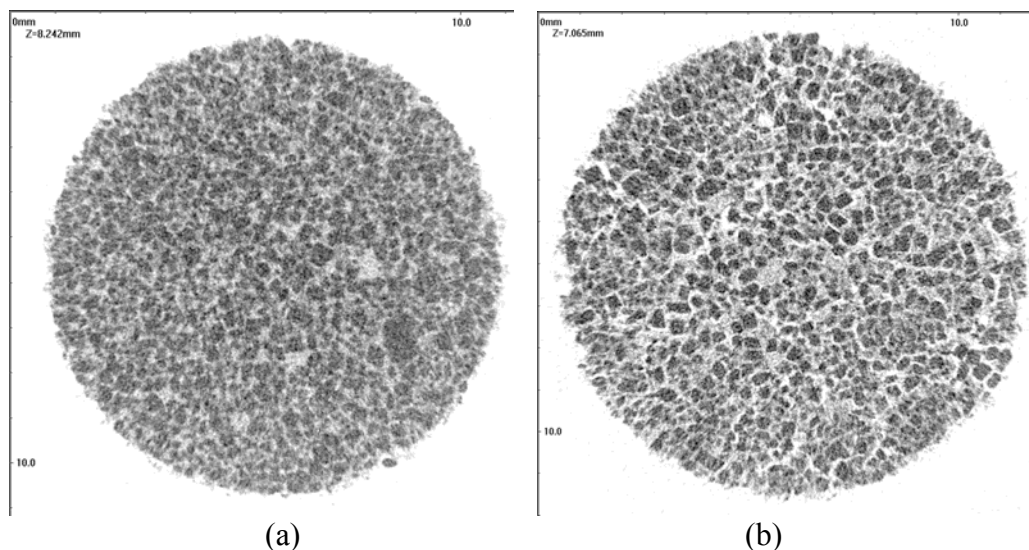


Figure 10(a) X-ray tomograph of pristine PBS (b) Sample after recovery from an Instron test. The side length of each image is 10 mm.

IMPACT ON POLYMER-BONDED SIMULANTS

Impact can produce ignition in energetic materials and is an obvious hazard scenario. The situation is complex involving both mechanical and chemical effects. Plate impact studies, using digital speckle radiography have been performed on a polymer bonded sugar to look at the internal displacement caused by a two step shock wave passing through the stimulant [42].

The inert polymer bonded explosive simulant was based on granulated sugar in a hydroxy-terminated polybutadiene (HTPB) matrix, designed to mimic gun-launch type fillings. The speckle field was created within the target samples by the seeding of lead particles within a central plane perpendicular to x-ray axis and parallel to the impact axis.

The X-ray system used was a Scandiflash 150 KeV unit producing a flash of x-rays in a 70 ns pulse. The X-rays impinged upon medical grade intensifier screens and film, which was subsequently digitally scanned. Images were taken of the target in advance of and during the impact process.

The targets were shock loaded by plate impact of polycarbonate [43]. Additionally, an experiment was performed in which the sample was doubly shocked, first by polycarbonate and then by copper a few microseconds later. Double shock scenarios have important implications for explosive initiation [44].

Figure 11 shows the x-ray of the image taken during impact. The projectile has just begun to penetrate the target. Also visible in the image is a fiducial speckle field which is used to remove any rigid body motions introduced during the scanning process. Also visible is the silhouette of a 1 pence piece which is used as a scale bar (diameter 20.32 mm).

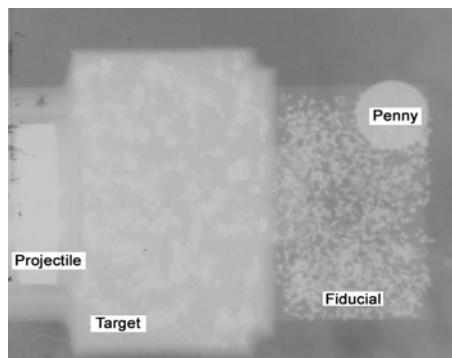


Figure 11: X-ray of experiment 5, 8.4 μ s after impact. Projectile travelling left to right.

Figure 12 shows the u -component of displacement obtained from the DSR analysis within the target area of experiment 11. The u -axis is parallel to the projectile axis, and the v -axis is perpendicular. The curved nature of the shock front shown in figure 12a is due to the lateral release of material from a shocked to an unshocked state. The lateral release waves originate from the radial edges of the plate projectile where the material is no longer loaded uniaxially, and will eventually negate the propagating shock wave. Information about the lateral release is best seen within the v -component data, shown in figure 12b.

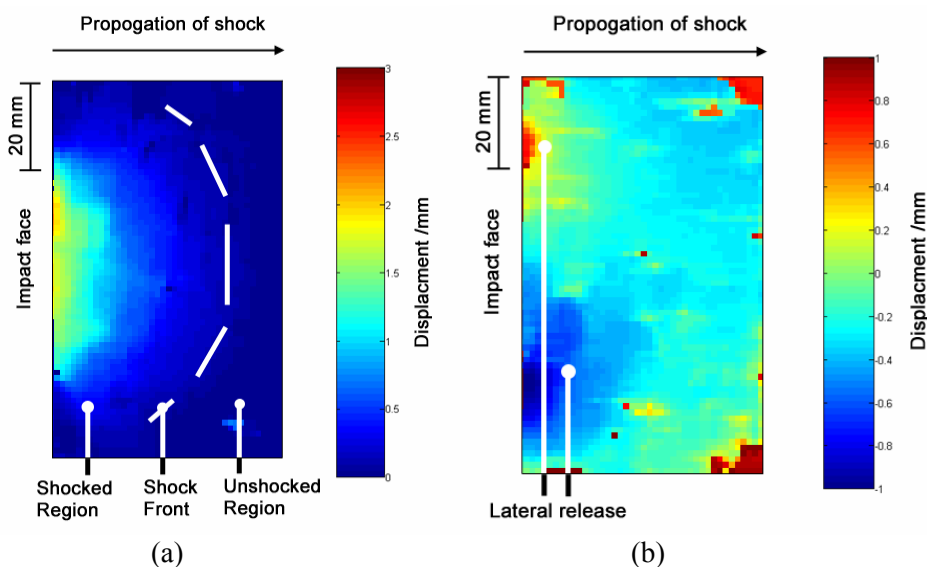


Figure 12: u -component data (a) and v -component (b) from the data in figure 11.

Figure 13 shows the mean u -component of displacement along the central impact axis for a double shock experiment. Three regions are distinguishable. Region I is unshocked material. Region II is material subject to shock loading by polycarbonate: the strain in this region is 5.5 ± 0.1 %. Region III is material subject to double shock loading, first by polycarbonate and then copper: the strain in this region is 60 ± 5 %.

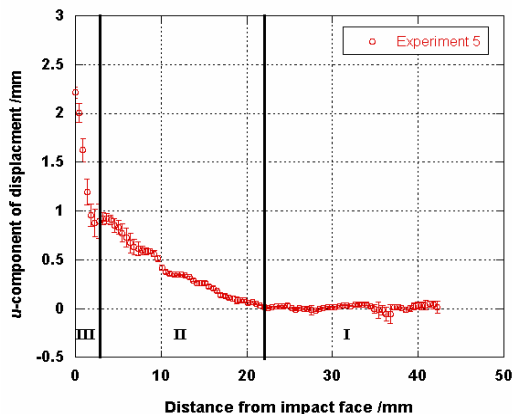


Figure 13: Double Shock Experiment u -component data.

SUMMARY

As PBX systems become more widely used, the understanding of the mechanisms responsible for reaction formation and growth is necessary.

In this paper, a brief review of the main mechanisms for hot-spot formation has been given. It must be remembered that these mechanisms are additive in nature. In some of the cases presented, the use of a single parameter, such number of voids in a crystal, does not give an indication of explosive sensitivity. This is a result of the formation of hot-spots being a function of length, pressure and time, as emphasised by the different ranking of material sensitivity seen in a gap test as opposed to a laser driven flier experiment. Once formed, however, the hot-spots can cause reaction to spread rapidly though a granular bed or, in PBXs, through openings caused by debonding of the explosive from the binder.

Polymer bonded systems have added complication due to nature of the polymer itself. However, the inclusion of fine-grained energetic material within the binder is an added factor. For modellers, this adds the difficulty that the polymer binder may be significantly stiffer in the PBX than it is a single material and be acting as a two or three phase system. Additionally, this fine-grained material may become sensitive if the polymer surrounding it is heated. This may happen for example when the polymer takes up most of the dynamic strain during compression.

The interaction of modelling with experimental programmes provides the most effective route to understanding the basic processes. Much of the above data has been used to populate the Porter Gould model, developed by QinetiQ.

ACKNOWLEDGEMENTS

Many organisations have sponsored research in the Fracture and Shock Physics Group. This has allowed a variety of experimental systems to be developed. Amongst those who have directly or indirectly contributed to the research presented here are MoD, QinetiQ, AWE, [dstl], EPSRC and Orica. Dr. P. Laity of the Materials Science department gave invaluable help with X-ray tomography. D. Johnson, R. Flaxman, R. Marrah, D. Powell of the Cavendish Workshops gave much technical support. Dr. S. Walley ensured that the references were up to date. Former members of the Group, Drs H.T. Goldrein, S.G. Grantham, P.R. Rae and C.R. Siviour made possible the ground work for much of this research.

REFERENCES

1. Bowden, F.P. and A.D. Yoffe, *Initiation and Growth of Explosion in Liquids and Solids (republ. 1985)*. 1952, Cambridge: Cambridge University Press.
2. Bowden, F.P., K. Singh, and A.M. Yuill, *Size effects in the initiation and growth of explosion*. *Nature*, 1953. **172**: p. 378-380.
3. Bowden, F.P., B.L. Evans, and A.D. Yoffe, *The combustion and explosion of crystals*, in *Proc. Sixth Symp. (Int.) on Combustion*. 1957, Reinhold: New York. p. 609-612.
4. Bowden, F.P. and A.D. Yoffe, *Fast Reactions in Solids*. 1958, London: Butterworth.
5. Field, J.E., G.M. Swallowe, and S.N. Heavens, *Ignition mechanisms of explosives during mechanical deformation*. *Proc. R. Soc. Lond. A*, 1982. **382**: p. 231-244.
6. Field, J.E., *Hot spot ignition mechanisms for explosives*. *Accounts Chem. Res.*, 1992. **25**: p. 489-496.
7. Bonnett, D.L. and P.B. Butler, *Hot-spot ignition of condensed phase energetic materials*. *J. Propulsion Power*, 1996. **12**: p. 680-690.
8. Coffey, C.S., et al., *Experimental investigation of hot spots produced by high rate deformation and shocks*, in *Proc. Seventh Symposium (Int.) on Detonation*, J.M. Short, Editor. 1981, Naval Surface Weapons Center: Dahlgren, Virginia. p. 970-975.
9. Armstrong, R.W., et al., *Investigation of hot spot characteristics in energetic crystals*. *Thermochim. Acta*, 2002. **384**: p. 303-313.
10. Sharma, J., et al., *Atomic force microscopy of hot spot reaction sites in impacted RDX and laser heated AP*. *Mater. Res. Soc. Symp. Proc.*, 1996. **418**: p. 257-264.
11. Gifford, M.J., W.G. Proud, and J.E. Field, *Development of a method for quantification of hot-spots*. *Thermochim. Acta*, 2002. **384**: p. 285-290.
12. Balzer, J.E., et al., *High-speed photographic study of the drop-weight impact response of RDX/DOS mixtures*. *Combust. Flame*, 2003. **135**: p. 547-555.
13. Proud, W.G., I.J. Kirby, and J.E. Field, *The nature, number and evolution of hot-spots in ammonium nitrate*, in *Shock Compression of Condensed Matter - 2003*, M.D. Furnish, Y.M. Gupta, and J.W. Forbes, Editors. 2004, American Institute of Physics: Melville NY. p. 1017-1020.
14. Butler, P.B., J. Kang, and M.R. Baer, *Hot spot formation in a collapsing void of condensed-phase, energetic material*, in *Proc. Ninth Symposium (Int.) on Detonation*. 1989, Office of the Chief of Naval Research: Arlington, Virginia. p. 906-917.
15. Walley, S.M., et al., *Response of thermites to dynamic high pressure and shear*. *Proc. R. Soc. Lond. A*, 2000. **456**: p. 1483-1503.

17th DYMAT Technical Meeting, 2007, Cavendish Laboratory, Cambridge

16. Bowden, F.P., M.A. Stone, and G.K. Tudor, *Hot spots on rubbing surfaces and the detonation of explosives by friction*. Proc. R. Soc. Lond. A, 1947. **188**: p. 329-349.
17. Afanasev, G.T., et al., *Formation of local hot spots during the fracture of thin layers under shock*. Combust. Explos. Shock Waves, 1972. **8**: p. 241-246.
18. Chaudhri, M.M., *High speed photography of electrical breakdown and explosion of silver azide*. Nature, 1973. **242**: p. 110-111.
19. Shonhiwa, T. and M.B. Zaturka, *Disappearance of criticality in thermal ignition for a simple reactive viscous flow*. J. Appl. Math. Phys., 1986. **37**: p. 632-635.
20. Bowden, F.P., et al., *The period of impact, the time of initiation and the rate of growth of the explosion of nitroglycerine*. Proc. R. Soc. Lond. A, 1947. **188**: p. 311-329.
21. Bowden, F.P. and A. Yoffe, *Hot spots and the initiation of explosion*, in *Proc. Third Symp. on Combustion and Flame and Explosion Phenomena*. 1949, Williams & Wilkins: Baltimore, Maryland. p. 551-560.
22. Proud, W.G., et al., *AFM studies of PBX systems*. Thermochim. Acta, 2002. **384**: p. 245-251.
23. Gifford, M.J., et al., *Properties of ultrafine energetic materials*, in *Theory and Practice of Energetic Materials. 4*, L. Chen and C. Feng, Editors. 2001, China Science and Technology Press: Beijing. p. 3-11.
24. Field, J.E., et al., *The shock initiation and high strain rate mechanical characterization of ultrafine energetic powders and compositions*. Mater. Res. Soc. Symp. Proc., 2004. **800**: p. 179-190.
25. Chakravarty, A., W.G. Proud, and J.E. Field, *Small scale gap testing of novel compositions*, in *Shock Compression of Condensed Matter - 2003*, M.D. Furnish, Y.M. Gupta, and J.W. Forbes, Editors. 2004, American Institute of Physics: Melville NY. p. 935-938.
26. Chakravarty, A., et al., *Factors affecting shock sensitivity of energetic materials*, in *Shock Compression of Condensed Matter - 2001*, M.D. Furnish, N.N. Thadhani, and Y. Horie, Editors. 2002, American Institute of Physics: Melville, NY. p. 1007-1010.
27. Greenaway, M.W., et al., *An investigation into the initiation of hexanitrostilbene by laser-driven flyer plates*, in *Shock Compression of Condensed Matter - 2001*, M.D. Furnish, N.N. Thadhani, and Y. Horie, Editors. 2002, American Institute of Physics: Melville, NY. p. 1035-1038.
28. Partom, Y., *A void collapse model for shock initiation*, in *Proc. Seventh Symposium (Int.) on Detonation*, J.M. Short, Editor. 1981, Naval Surface Weapons Center: Dahlgren, Virginia. p. 506-516.
29. Chaudhri, M.M., *The initiation of fast decomposition in solid explosives by fracture, plastic flow, friction and collapsing voids*, in *Proc. Ninth Symposium (Int.) on Detonation*. 1989, Office of the Chief of Naval Research: Arlington, Virginia. p. 857-867.
30. van der Heijden, A.E.D. and R.H.B. Bouma, *Shock sensitivity of HMX/HTPB PBXs: Relation with HMX crystal density*, in *Proc. 29th Int. Ann. Conf. of ICT: Energetic Materials Production, Processing and Characterization*. 1998, Fraunhofer Institut für Chemische Technologie: Karlsruhe, Germany. p. paper 65.
31. Czerski, H., et al. *Links between the morphology of RDX crystals and their shock sensitivity*. In *Shock Compression of Condensed Matter - 2005*, M.D. Furnish, M. Elert,

17th DYMAT Technical Meeting, 2007, Cavendish Laboratory, Cambridge

- T.P. Russell, C.T. White, Editors. 2006, American Institute of Physics: Melville NY. p. 1053-1056.
32. Czerski, H. Ignition of HMX and RDX, PhD Thesis, Cambridge University, 2006
 33. Greenaway, M.W., P.R. Laity, and V. Pelikan. *X-ray tomography of sugar and HMX granular beds undergoing compaction*. In *Shock Compression of Condensed Matter - 2005*, M.D. Furnish, M. Elert, T.P. Russell, C.T. White, Editors. 2006, American Institute of Physics: Melville NY. p. 1279-1282.
 34. Gray III, G.T., et al., *High- and low-strain rate compression properties of several energetic material composites as a function of strain rate and temperature*, in *Proc. 11th Int. Detonation Symposium*, J.M. Short and J.E. Kennedy, Editors. 2000, Office of Naval Research: Arlington, Virginia. p. 76-84.
 35. Idar, D.J., et al., *Influence of polymer molecular weight, temperature, and strain rate on the mechanical properties of PBX 9501*. 2001, Los Alamos National Laboratory.
 36. Goldrein, H.T., *Monitoring the effects of ageing on the mechanical properties of polymer bonded explosives*, in *Slow Processes: The Accumulation of Molecular Events Leading to Failure on Macroscale (ARL-SR-16)*, R.W. Shaw, Editor. 2001, Army Research Laboratory: Research Triangle Park, North Carolina. p. 15-30.
 37. Siviour, C.R., et al., *High resolution optical analysis of dynamic experiments on PBXs*, in *Proc. 7th Seminar on New Trends in Research of Energetic Materials*, J. Vágenknecht, Editor. 2004, University of Pardubice: Pardubice, Czech Republic. p. 277-284.
 38. Siviour, C.R., et al., *Particle size effects on the mechanical properties of a polymer bonded explosive*. *J. Mater. Sci.*, 2004. **39**: p. 1255-1258.
 39. Laity, P.R., et al. *High strain rate characterisation of a polymer bonded sugar*. in *Shock Compression of Condensed Matter*. 2005. Baltimore: AIP. in press
 40. C.R.Siviour, et al., *High strain-rate properties of a polymer-bonded sugar*. in preparation, 2007.
 41. C.R.Siviour, et al., *Novel optical techniques applied to a PBX system*. in preparation, 2007.
 42. D M Williamson, D J Chapman, W G Proud and P D Church, Application of digital speckle radiography to measure the internal displacement fields of a shock loaded material. *Photon06*
 43. Field J.E., Walley S.M., Proud W.G., Goldrein H.T., and Siviour C.R. 2004 Review of experimental techniques for high rate deformation and shock studies. *International Journal of Impact Engineering* **30** 725-775.
 44. Gustavsen R.L., Sheffield S.A., Alcon R.R., Winter R.E., Taylor P., and Salisbury D.A. 2002 Double shock initiation of the HMX based explosive EDC-37. In proceedings of the 12th APS Topical Meeting on *Shock Compression of Condensed Matter 2001* (Edited by Furnish/Thadhani/Horie) pp. 999-1002. (The American Institute of Physics, New York).

Viscoelastic Behaviors of Plastic-Bonded Energetic Materials Accounting for Nonlinear Interface Debonding

Henry Tan

School of Mechanical, Aerospace and Civil Engineering, The University of Manchester, Manchester, M60 1QD, UK

Abstract: The effect of crystal/binder interface debonding on the behavior of plastic-bonded explosives is studied. The interface debonding is represented by a nonlinear cohesive law for the high explosive PBX 9501. The micromechanics analysis based on the Mori-Tanaka method gives the constitutive relation of plastic-bonded explosives in terms of the properties of elastic crystals, viscoelastic binder, and nonlinear cohesive law for interfaces. For the example of a plastic-bonded explosive subject to hydrostatic tension, simple analytical expressions of the macroscopic stress-strain relation are obtained. The strain rate, temperature and interface debonding, have combined effects on the behavior of plastic-bonded explosives. High strain rate and low temperature give higher strength. However, the rate and temperature effects decrease as the crystal volume fraction increases.

Keywords: Interface debonding, Binder, Viscoelasticity, Strain rate, Temperature, Size effect

1 Introduction

A plastic-bonded explosive is composed of energetic crystals and a polymeric binder. The volume fraction of the energetic crystals is high. For the high explosive PBX 9501, the volume fraction of HMX energetic crystals is 93% (Bennett et al., 1998; Liu, 2003). Because of the introduced high specific surface (i.e., high crystal/binder interface area per unit volume of the plastic-bonded explosive), and the large openings of the debonded interfaces which can be on the order of 100 μ m (Tan et al. 2005b), the debonding of the interfaces between energetic crystals and the binder may significantly influence the behavior of the plastic-bonded explosive.

Plastic-bonded explosives can be treated as composite materials with energetic crystals embedded in the polymeric binder. Using micromechanics modeling, Tan et al., (2005a, 2006, 2007) analyzed the effects of nonlinear interface debonding on the behavior of high explosive PBX 9501. Typically interface debonding introduces size effect of the energetic crystals, with small crystals lead to the hardening while large crystals yield the softening behavior of the plastic-bonded explosives. Large crystals may lead to catastrophic debonding, i.e., sudden debonding even under static load, that may trigger the reaction or detonation of plastic-bonded explosives.

However, viscoelastic properties of the binder were neglected in previous analytical studies on the constitutive behavior of plastic-bonded explosives accounting for nonlinear interface debonding. The binder is used to bond the constituents together as a composite. It is usually a long chain polymer with mechanical properties distinctly different from a linear elastic material. The plastic-bonded explosives typically exhibit viscoelastic behavior with stress-strain relation that depends on the loading rate and temperature (Cady et al., 2006). This may influence the explosive initiation sensitivity (Baer et al., 2007).

The objective of this paper is to investigate the viscoelastic behavior of plastic-bonded explosives while accounting for the nonlinear debonding of interfaces between crystals and the binder. We establish an analytic model to obtain the constitutive properties of a plastic-bonded explosive in terms of the properties of elastic crystals, viscoelastic binder, and nonlinear cohesive law for crystal/binder interfaces. The paper is outlined as follows. The viscoelastic behavior of the polymeric binder is reviewed in Section 2. The cohesive law for interfaces between crystals and the binder for the high explosive PBX 9501 is summarized in section 3. A micromechanics model that links the behavior of the plastic-bonded explosive to its constituents (crystals, viscoelastic binder and interfaces) is established. In order to illustrate the approach, we present an example of a plastic-bonded explosive subject to hydrostatic tension in Section 4. The results pertinent to the strain rate, temperature, and crystal sizes are given in Section 5.

2 Viscoelastic behavior of the binder

At a temperature above -20°C and moderate loading rate, the polymeric binder in the high explosive PBX 9501, plasticized estane, is a rubbery elastomer. Its mechanical response can be treated as linear viscoelastic (Mas et al., 2002; Clements and Mas, 2004) with the stress-strain relation

$$\sigma_{ij}(t) = \int_{-\infty}^t L_{ijkl}^b(t-\xi) \dot{\epsilon}_{kl}(\xi) d\xi, \quad (1)$$

where σ_{ij} is the stress, $\dot{\epsilon}_{kl}(\xi)$ is the strain rate at time ξ , and $L_{ijkl}^b(t)$ is the fourth-order stress relaxation tensor given in terms of the bulk modulus K^b and shear stress relaxation modulus $\mu^b(t)$ by (Clements and Mas, 2004)

$$L_{ijkl}^b(t) = \left[K^b - \frac{2}{3} \mu^b(t) \right] \delta_{ij} \delta_{kl} + \mu^b(t) (\delta_{ik} \delta_{jl} + \delta_{il} \delta_{jk}). \quad (2)$$

Here δ_{ij} is the Kronecker delta, K^b is rate- (or time-) independent, and $\mu^b(t)$ can be expressed in Prony series as (Mas et al., 2002; Clements and Mas, 2004)

$$\mu^b(t) = \mu_{\infty} + \sum_{i=1}^N \mu_i \exp(-t/t_i), \quad (3)$$

where μ_{∞} is the discrete equilibrium shear modulus that corresponds to infinite relaxation time; N is the number of relaxation modes; and μ_i and t_i are the strength and relaxation time for the i^{th} relaxation mode, respectively. For the polymeric binder in the high explosive PBX 9501, Mas et al. (2002) determined for μ_i (in MPa) (i form 1 to $N=22$) as given in Table 1.

Table 1. The 22-element ($N=22$) generalized Maxwell model for the binder in the high explosive PBX 9501. The unit for shear strength μ_i is MPa.

Element i	1	2	3	4	5	6	7
$\log_{10}(\mu_i)$	-2.38	-2.13	-1.80	-1.42	-1.17	-1.05	-0.937
8	9	10	11	12	13	14	15
-0.847	-0.790	-0.654	-0.323	0.418	1.11	1.72	2.35
16	17	18	19	20	21	22	
2.64	2.66	2.54	2.40	2.25	2.07	1.88	

The relaxation time for the i^{th} relaxation mode in Eq. (3) is $t_i = 1.5\alpha_T 10^{(7-i)}$ (in seconds), where α_T is the Williams-Landell-Ferry (WLF) shift function (Williams et al., 1955) that accounts for the temperature effect, and is given by

$$\log_{10} \alpha_T = -\frac{C_1(T-T_{ref})}{C_2 + T - T_{ref}}, \quad (4)$$

17th DYMAT Technical Meeting, 2007, Cavendish Laboratory, Cambridge

where T_{ref} is the reference temperature, C_1 and C_2 are two WLF shift constants. For the polymeric binder in the high explosive PBX 9501, $T_{ref} = 19^\circ\text{C}$, $C_1 = 6.5$ and $C_2 = 120^\circ\text{C}$ (Clements and Mas, 2004). Figure 1 shows the time-dependent shear stress relaxation modulus $\mu^b(t)$ at different temperature $T=0^\circ\text{C}$, 20°C and 40°C .

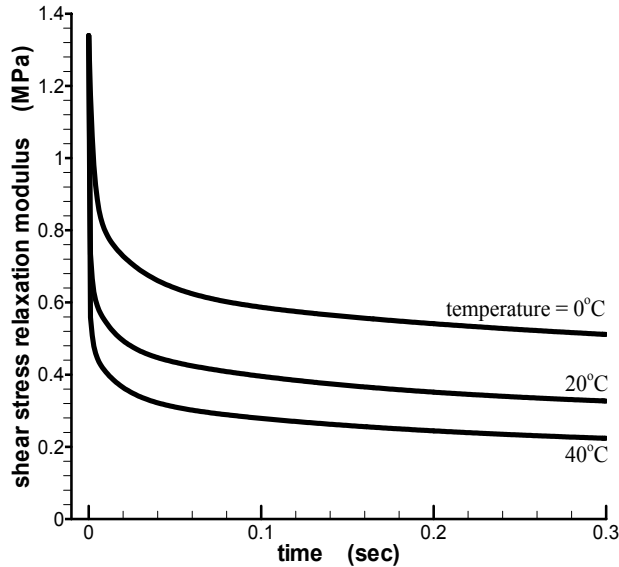


Figure 1. The time-dependent shear stress relaxation modulus $\mu^b(t)$ at different temperatures $T=0^\circ\text{C}$, 20°C and 40°C .

3 The cohesive law for interfaces between energetic crystals and the binder

Debonding of crystal/binder interfaces can usually be characterized by a nonlinear cohesive law, which gives stress tractions in terms of displacement discontinuities across the interface. Tan et al. (2005b) combined experiments and micromechanics models to determine the cohesive law for crystal/binder interfaces in the high explosive PBX 9501. The cohesive law displays three stages, namely the linear hardening (stage I), softening (stage II), and complete debonding. As shown in Figure 2, the cohesive law displays three-stage, piecewise linear relation involving three parameters, namely, the interface cohesive strength σ_{max} , linear modulus k_σ and softening modulus \tilde{k}_σ . For the high explosive PBX 9501, the cohesive strength $\sigma_{max} = 1.66\text{MPa}$, and the linear modulus $k_\sigma = 1.55\text{GPa}/\mu\text{m}$ is much larger than the softening modulus $\tilde{k}_\sigma = 17\text{MPa}/\text{mm}$ (Tan et al., 2005b). The normal traction σ^{int} is then given in term of the opening displacement $[u]$ across the interface by

$$\begin{aligned}
 \sigma^{int} &= k_\sigma [u] & [u] \leq 1.1\text{nm} & \text{stage - I, hardening} \\
 \sigma^{int} &= (1 + \tilde{k}_\sigma / k_\sigma) \sigma_{max} - \tilde{k}_\sigma [u] & 1.1\text{nm} < [u] < 98\mu\text{m} & \text{stage - II, softening} \\
 \sigma^{int} &= 0 & [u] \geq 98\mu\text{m} & \text{stage - III, complete debonding}
 \end{aligned} \quad (5)$$

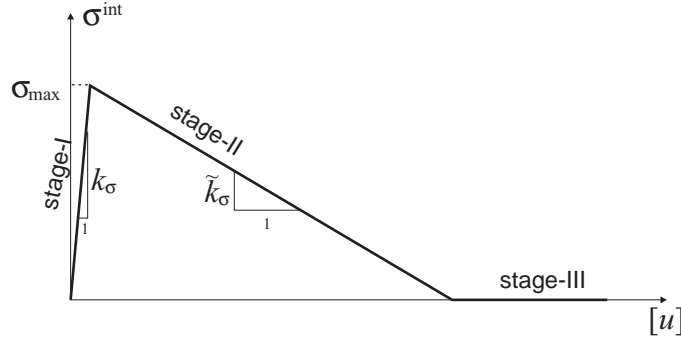


Figure 2. Interface cohesive model.

4 The Mori-Tanaka Method Accounting for the Debonding between Energetic Crystals and the Binder

4.1 Laplace Transform to the Deformation of Energetic Crystals and Binder

For any function $g(t)$, the Laplace transform is defined as

$$\hat{g}(s) = \int_0^{\infty} e^{-st} g(t) dt. \quad (6)$$

The energetic crystals are linear elastic with the linear modulus tensor $L_{ijkl}^c(t) = \left(K^c - \frac{2}{3} \mu^c \right) \delta_{ij} \delta_{kl} + \mu^c (\delta_{ik} \delta_{jl} + \delta_{il} \delta_{jk})$, where K^c and μ^c are the elastic bulk and shear moduli, respectively. With the Laplace transform, their stress-strain relation $\sigma_{ij} = L_{ijkl}^c \varepsilon_{kl}$ becomes

$$\hat{\sigma}_{ij} = L_{ijkl}^c \hat{\varepsilon}_{kl}, \quad (7)$$

i.e., $\hat{\sigma}_{ij}$ and $\hat{\varepsilon}_{kl}$ satisfy the linear elastic relation with the elastic bulk modulus K^c and shear modulus μ^c .

The Laplace transform of the linear viscoelastic stress-strain relation (2) for the binder is

$$\hat{\sigma}_{ij} = s \hat{L}_{ijkl}^b \hat{\varepsilon}_{kl}, \quad (8)$$

where we have used the initial condition $\varepsilon_{kl}|_{t=0} = 0$, and

$$s \hat{L}_{ijkl}^b = \left(K^b - \frac{2}{3} s \hat{\mu}^b \right) \delta_{ij} \delta_{kl} + s \hat{\mu}^b (\delta_{ik} \delta_{jl} + \delta_{il} \delta_{jk}). \quad (9)$$

Equations (8) and (9) suggest that $\hat{\sigma}_{ij}$ and $\hat{\varepsilon}_{kl}$ satisfy the linear elastic relation with the elastic bulk modulus K^b and equivalent elastic shear modulus $s \hat{\mu}^b$. For the Prony series expression of the shear stress relaxation modulus in (3), $s \hat{\mu}^b$ is given by

$$s\hat{\mu}^b = \mu_\infty + \sum_{i=1}^N \mu_i \frac{st_i}{st_i + 1}. \quad (10)$$

4.2 General Approach Accounting for Interface Debonding

Tan et al. (2005a) used the Mori-Tanaka method to study the effect of nonlinear interface debonding between elastic crystals and the binder. Its constitutive relations still hold if the stress and strain are substituted by the Laplace transformed $\hat{\sigma}_{ij}$ and $\hat{\epsilon}_{ij}$, and the elastic shear modulus of the binder is substituted by $s\hat{\mu}^b$.

Let $\hat{\sigma}$ and $\hat{\epsilon}$ denote the Laplace transform of the macroscopic stress $\bar{\sigma}$ and strain $\bar{\epsilon}$ in a plastic-bonded explosive, and they are given by (Tan et al., 2005a)

$$\hat{\sigma} = (1-f)\hat{\sigma}^b + f\hat{\sigma}^c, \quad (11)$$

$$\hat{\epsilon} = (1-f)\hat{\epsilon}^b + f\hat{\epsilon}^c + f\hat{\epsilon}^{\text{int}}, \quad (12)$$

where σ^b , σ^c , ϵ^b , and ϵ^c are the average stresses and strains in the binder and crystals, respectively, the additional term $f\hat{\epsilon}^{\text{int}}$ represents the contribution from crystal/binder interface debonding with $\hat{\epsilon}^{\text{int}}$ relating to the Laplace transform of the displacement discontinuity $[\hat{u}] = \hat{u}^b - \hat{u}^c$ across crystal/binder interfaces S^{int} by

$$\hat{\epsilon}^{\text{int}} = \frac{1}{2\Omega^c} \int_{S^{\text{int}}} ([\hat{u}] \otimes \mathbf{n} + \mathbf{n} \otimes [\hat{u}]) dA. \quad (13)$$

Here Ω^c is the total crystal volume, and \mathbf{n} is the unit normal vector on the interface pointing into the binder.

Equations (11) and (12), together with (7) and (8), give the macroscopic strain $\hat{\epsilon}$ as

$$\hat{\epsilon} = (s\mathbf{L}^b)^{-1} : \hat{\sigma} + f \left\{ \left[(s\mathbf{L}^c)^{-1} - (s\mathbf{L}^b)^{-1} \right] : \hat{\sigma}^c + \hat{\epsilon}^{\text{int}} \right\}. \quad (14)$$

4.3 Hydrostatic Tension

To illustrate the present approach accounting for the debonding of interfaces between crystals and binder, we consider an example of spherical crystals in binder subject to hydrostatic tension $\bar{\sigma}\mathbf{I}$, where \mathbf{I} is the second-order identity tensor. The crystal volume fraction is f and the crystal radius is a . Under such loading the stress in crystals is hydrostatic $\sigma^{\text{int}}\mathbf{I}$, where σ^{int} is the normal traction along crystal/binder interfaces. The tensorial equation (14) then becomes the following scalar equation

$$\hat{\epsilon} = \frac{1}{3K^b} \hat{\sigma} + f \left(\frac{1}{3K^c} - \frac{1}{3K^b} \right) \hat{\sigma}^{\text{int}} + f \frac{[\hat{u}]}{a}, \quad (15)$$

where $\hat{\epsilon} = \hat{\epsilon}_{kk}/3$ and $\hat{\sigma}$ are the transformed mean strain and stress in the explosive, $\hat{\sigma}^{\text{int}}$ is the Laplace transform of σ^{int} , and $[\hat{u}]$ is the Laplace transform of the normal displacement discontinuity across crystal/binder interfaces.

17th DYMAT Technical Meeting, 2007, Cavendish Laboratory, Cambridge

In the following we use the Mori-Tanaka method to relate $\hat{\sigma}^{\text{int}}$ and $[\hat{u}]$ in terms of stress $\hat{\sigma}$, such that Eq. (15) gives the transformed stress-strain relation of the plastic-bonded explosive.

4.4 Mori-Tanaka Method

For the high explosive PBX 9501, the elastic bulk moduli of energetic crystals and binder are $K^c = 12.5 \text{ GPa}$ (Zaug, 1998) and $K^b = 167 \text{ MPa}$ (Tan et al., 2005b), and both are much larger than the shear modulus μ^b of the binder (on the order of 1 MPa). The linear modulus of the interface $k_\sigma = 1.55 \text{ GPa}/\mu\text{m}$ also gives $k_\sigma a$ much larger than μ^b (for the representative crystal size a from $4 \mu\text{m}$ to $125 \mu\text{m}$ in the high explosive PBX 9501). Tan et al. (2005b) showed that, under these conditions ($K^c \gg \mu^b$, $K^b \gg \mu^b$, $k_\sigma a \gg \mu^b$), the high explosive PBX 9501 has a rather large elastic bulk modulus such that the elastic deformation during stage-I opening of crystal/binder interfaces is negligible, i.e., the opening displacement is negligible before the interface cohesive strength σ_{max} is reached. The interface cohesive law (1) during stage-II opening of crystal/binder interfaces then becomes

$$\sigma^{\text{int}} = \sigma_{\text{max}} - \tilde{k}_\sigma [u] \quad \text{for} \quad [u] \leq \frac{\sigma_{\text{max}}}{\tilde{k}_\sigma} \approx 98 \mu\text{m} \quad (16)$$

Its Laplace transform gives

$$\hat{\sigma}^{\text{int}} = \frac{\sigma_{\text{max}}}{s} - \tilde{k}_\sigma [\hat{u}]. \quad (17)$$

As shown in the Appendix, the Mori-Tanaka method gives $[u]$ in terms of σ^{int} and $\bar{\sigma}$, and its Laplace transform is

$$\frac{[\hat{u}]}{a} = \frac{1}{1-f} \left(\frac{1}{3K^b} + \frac{1}{4s\hat{\mu}^b} \right) (\hat{\sigma} - f\hat{\sigma}^{\text{int}}) - \left(\frac{1}{3K^c} + \frac{1}{4s\hat{\mu}^b} \right) \hat{\sigma}^{\text{int}}. \quad (18)$$

Elimination of $[\hat{u}]$ and $\hat{\sigma}^{\text{int}}$ from Eqs. (15), (17) and (18), together with the fact that the bulk moduli of energetic crystals and the binder are much larger than the softening modulus of crystal/binder interfaces ($K^c \gg \tilde{k}_\sigma a$ and $K^b \gg \tilde{k}_\sigma a$), gives

$$f \left(\hat{\sigma} - \frac{\sigma_{\text{max}}}{s} \right) = [4(1-f)s\hat{\mu}^b - \tilde{k}_\sigma a] \hat{\varepsilon}. \quad (19)$$

The inverse Laplace transform gives

$$f(\bar{\sigma} - \sigma_{\text{max}}) = 4(1-f) \int_0^t \mu^b(t-t') \dot{\bar{\varepsilon}}(t') dt' - \tilde{k}_\sigma a \bar{\varepsilon}. \quad (20)$$

For the Prony series of μ^b in (3), the above stress-strain relation becomes

$$f(\bar{\sigma} - \sigma_{\text{max}}) = [4(1-f)\mu^b(0) - \tilde{k}_\sigma a] \bar{\varepsilon} - 4(1-f) \sum_{i=1}^N \frac{\mu_i}{t_i} \int_0^t \bar{\varepsilon}(\xi) \exp\left(-\frac{t-\xi}{t_i}\right) d\xi. \quad (21)$$

17th DYMAT Technical Meeting, 2007, Cavendish Laboratory, Cambridge

The normal displacement discontinuity across the crystal/binder interface is given in terms of the macroscopic strain $\bar{\varepsilon}$, crystal volume fraction f and radius a by

$$[u]f = a\bar{\varepsilon}. \quad (22)$$

This simple relation suggests that the macroscopic strain results mainly from the crystal/binder interface debonding. As seen from (16), the analysis in this section holds for $[u] \leq \frac{\sigma_{\max}}{\tilde{k}_\sigma}$. Therefore, the constitutive relation (20) and (21) hold when

$$\bar{\varepsilon} \leq \frac{f\sigma_{\max}}{\tilde{k}_\sigma a}. \quad (23)$$

5 Results

5.1 Strain Rate Effect

For a constant strain rate $\dot{\bar{\varepsilon}}$ of the plastic-bonded explosive, i.e., $\bar{\varepsilon} = \dot{\bar{\varepsilon}}t$, the constitutive relation Eq.(20) becomes

$$f(\bar{\sigma} - \sigma_{\max}) = \left[4(1-f)\mu_\infty - \tilde{k}_\sigma a \right] \bar{\varepsilon} + 4(1-f)\dot{\bar{\varepsilon}} \sum_{i=1}^N \mu_i t_i \left[1 - \exp\left(-\frac{\bar{\varepsilon}}{\dot{\bar{\varepsilon}}t_i}\right) \right]. \quad (24)$$

Figure 3 shows the stress-strain behavior of the plastic-bonded explosive for several strain rates $\dot{\bar{\varepsilon}} = 10, 1$ and 0.1sec^{-1} . The crystal volume fractions are $f=20\%$ and 60% , and the crystal radius is $a=125\mu\text{m}$. The viscoelastic properties of the binder are given in Section 2, and the room temperature is $T=20^\circ\text{C}$. The cohesive strength and softening modulus of the crystal/binder interfaces are $\sigma_{\max}=1.66\text{MPa}$ and $\tilde{k}_\sigma=17\text{MPa}/\text{mm}$ (Tan et al., 2005b). For $\dot{\bar{\varepsilon}}=10\text{sec}^{-1}$, the time to reach a fixed strain level is short (e.g., 0.01 second for the 10% strain), which gives the binder shear modulus $\mu^b=0.545\text{MPa}$ (for $T=20^\circ\text{C}$) from Fig. 2. For smaller strain rates $\dot{\bar{\varepsilon}}=1\text{sec}^{-1}$ and 0.1sec^{-1} , the corresponding time to reach the 10% strain is 0.1 second and 1 second, respectively, which give smaller binder shear moduli 0.396MPa and 0.270MPa at the same temperature $T=20^\circ\text{C}$ from Fig. 2. This is the reason that, for each fixed crystal volume fraction f , the stress-strain curve increases with the strain rate in Fig. 3. The stress-strain curve depends strongly on the strain rate $\dot{\bar{\varepsilon}}$ for relatively low crystal volume fraction $f=20\%$, but becomes insensitive to the strain rate for high crystal volume fraction $f=60\%$. This is because, as the crystal volume fraction increases (and therefore binder volume fraction decreases), the effect of viscous binder decreases, and the plastic-bonded explosive shows small strain rate dependence.

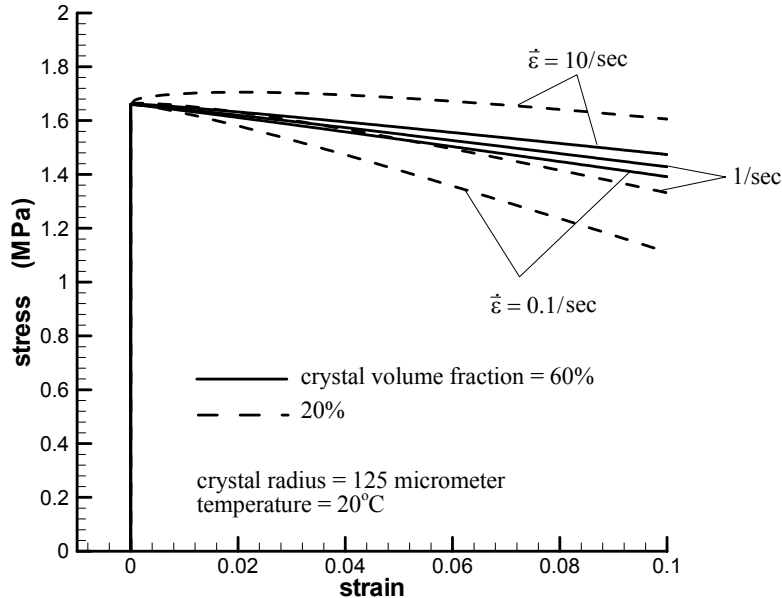


Figure 3. Effect of strain rate on the constitutive relation of plastic-bonded explosives.

At the low strain rate $\dot{\epsilon} = 0.1 \text{sec}^{-1}$, the viscous effect is relatively small and the elastic deformation plays an important role. The curve for $f=20\%$ is lower than that for $f=60\%$ due to the hard and stiff crystal. As the strain rate increases, however, the stress-strain curve for $f=20\%$ increases rapidly due to the viscous effect, and exceeds that for $f=60\%$.

5.2 Temperature Effect

Figure 4 shows the stress-strain curve for temperature 0°C , 20°C , 40°C and the strain rate 1sec^{-1} . The crystal volume fractions are $f=20\%$ and 60% , and the crystal radius is $a=125\mu\text{m}$. The properties of the binder and crystal/binder interfaces are the same as Section 5.1. The stress-strain curve in Fig. 4 increases as the temperature decreases; i.e., the composite displays higher strength at lower temperature. Similar to Fig. 3, the increase of stress-strain curve is significant for crystal volume fraction $f=20\%$ but becomes small for high crystal volume fraction $f=60\%$, which is once again due to the effect of viscous binder.

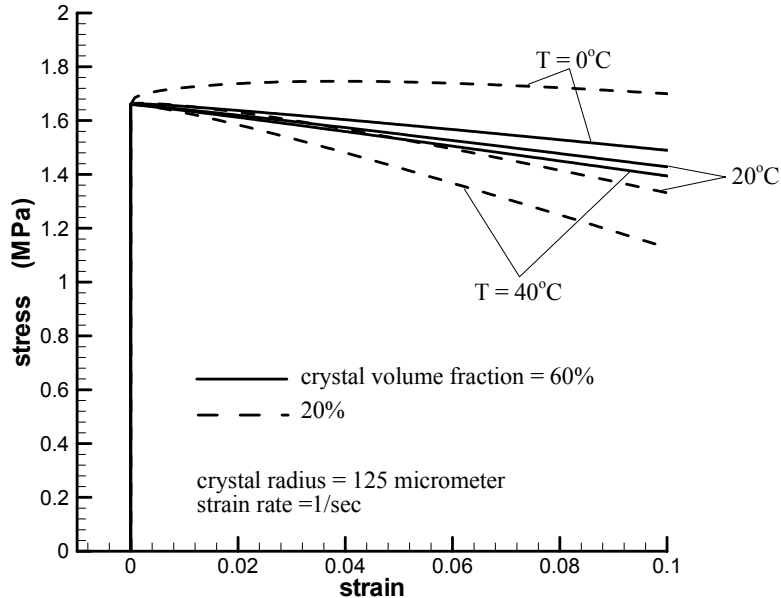
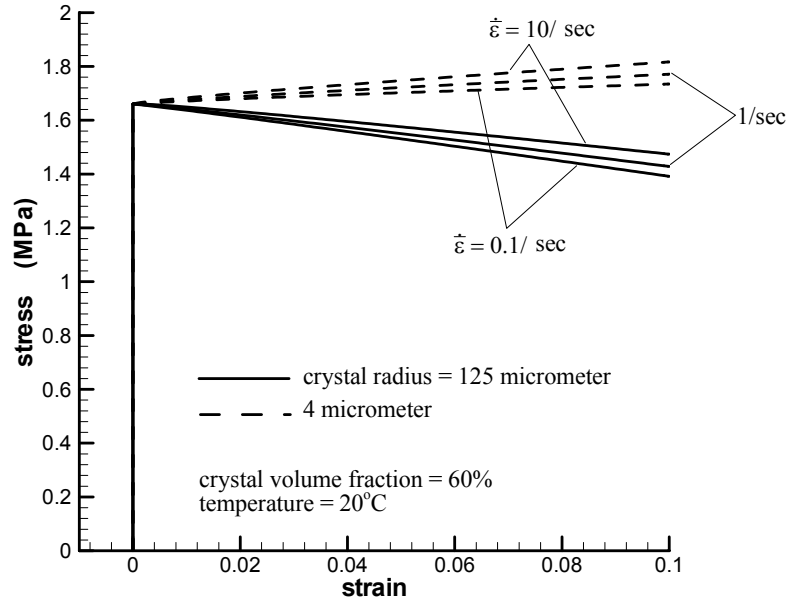


Figure 4. Effect of temperature on the constitutive relation of plastic-bonded explosives.

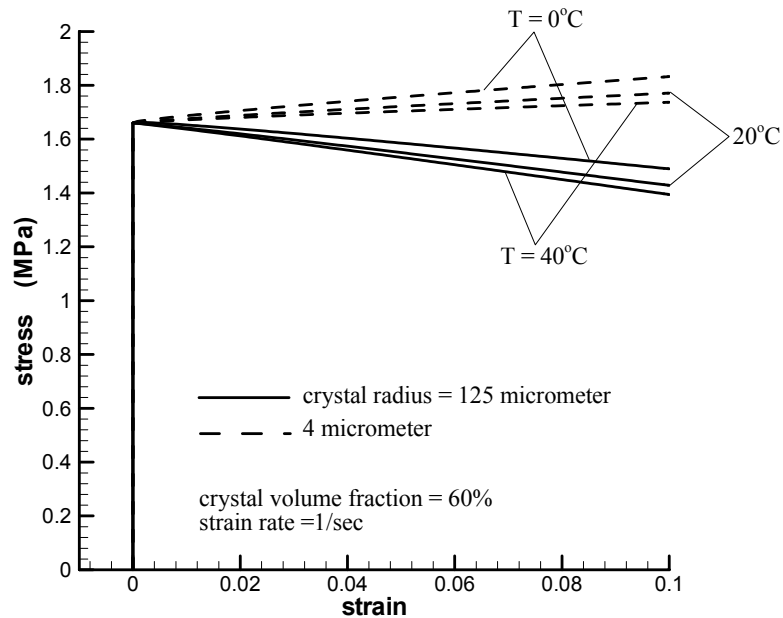
The curves in Fig. 4 for different temperatures are rather similar to those in Fig. 3 for different strain rates. This results from the Williams-Landell-Ferry shift function in Eqs. (3) and (4), which gives equivalence between time (or strain rate) and temperature.

5.3 Crystal Size Effect

The stress-strain curves for small ($a=4\mu\text{m}$) and large crystal ($a=125\mu\text{m}$) are shown in Fig. 5 for various strain rates $\dot{\epsilon}$ and temperature T . For each crystal size, the curves for different $\dot{\epsilon}$ and T are very close, which suggests the minimal viscous effect because of the high crystal volume fraction $f=60\%$. However, the curves for small crystals $a=4\mu\text{m}$ are higher than that for large crystals $a=125\mu\text{m}$. This crystal size effect is not due to the viscous effect since it has also been observed in prior studies based on the rate-independent binder behavior (Tan et al., 2005a).



(a)



(b)

Figure 5. Effect of crystal size (solid line for large crystals with radius of 125mm, and dashed line for small crystals with radius of 4mm) on the constitutive relation of plastic-bonded explosives. (a) different strain rates; (b) different temperature.

6 Concluding Remarks

We have studied the effect of nonlinear interface debonding on the viscoelastic behavior of plastic-bonded explosives. Together with a nonlinear cohesive law obtained for the high explosive PBX 9501, the Mori-Tanaka method gives the constitutive behavior of the plastic-bonded explosives in terms of the properties

17th DYMAT Technical Meeting, 2007, Cavendish Laboratory, Cambridge

of crystal, binder and interfaces. Using the example of plastic-bonded explosives with spherical crystals subject to hydrostatic tension, we show that the strain rate and temperature have strong effects on the behavior of plastic-bonded explosives. High strain rate and low temperature give higher strength. However, these rate and temperature effects decrease as the crystal volume fraction increases. Simple analytical expressions of the macroscopic stress-strain relation, accounting for nonlinear interface debonding and viscoelastic binder, are obtained.

Appendix

We consider a single spherical crystal of radius a in a infinite binder matrix subject to remote hydrostatic stress σ^b , where $\sigma^b = \sigma_{kk}^b/3$ is taken as the average mean stress in the binder in the Mori-Tanaka method. The stress state in the crystals is uniform and hydrostatic, and is denoted by $\sigma^{\text{int}}\mathbf{I}$. This gives the radial displacement at the crystal boundary as $\frac{\sigma^{\text{int}}}{3K^c}a$ (Timoshenko and Goodier, 1970).

The displacement is discontinuous across the crystal/binder interface due to interface debonding. The displacement and stress fields in the binder after the Laplace transform satisfy the linear elastic relation. The radial displacement at the inner boundary of the binder is given in terms of $\hat{\sigma}^b$ and $\hat{\sigma}^{\text{int}}$ by $a\left[\left(\frac{1}{3K^b} + \frac{1}{4s\hat{\mu}^b}\right)\hat{\sigma}^b - \frac{1}{4s\hat{\mu}^b}\hat{\sigma}^{\text{int}}\right]$, where K^b and $s\hat{\mu}^b$ are the bulk modulus and equivalent elastic shear modulus of the binder, respectively. Therefore, the displacement discontinuity in the radial direction is

$$[\hat{u}] = \left[\left(\frac{1}{3K^b} + \frac{1}{4s\hat{\mu}^b} \right) \hat{\sigma}^b - \left(\frac{1}{3K^c} + \frac{1}{4s\hat{\mu}^b} \right) \hat{\sigma}^{\text{int}} \right] a. \quad (\text{A1})$$

Elimination of $\hat{\sigma}^b$ from the above equation and Eq. (11) gives the Mori-Tanaka relation (18).

References

- Baer, M.R., Hall, C.A., Gustavsen, R.L., Hooks, D.E., Sheffield, S.A., 2007. Isentropic loading experiments of a plastic bonded explosive and constituents. *J. Appl. Phys.* 101, 034906.
- Bennett, J.G., Haberman, K.S., Johnson, J.N., Asay, B.W., Henson, B. F., 1998. A constitutive model for the non-shock ignition and mechanical response of high explosives. *J. Mech. Phys. Solids* 35, 2303-2322.
- Cady, C.M., Blumenthal, W.R., Gray III, G.T., Idar, D.J., 2006. Mechanical properties of plastic-bonded explosive binder materials as a function of strain-rate and temperature. *Polym. Eng. Sci.* 46, 812-819.
- Chu, T.C., Ranson, W.F., Sutton, M.A., Peters, W.H., 1985. Applications of digital image correlation techniques to experimental mechanics. *Exp. Mech.* 25, 232-244.
- Clements, B.E., Mas, E.M., 2004. A theory for plastic-bonded materials with a bimodal size distribution of filler particles. *Modelling Simul. Mater. Sci. Eng.* 12, 407-421.
- Liu, C., 2003. Specific surface: a missing parameter in high-explosive modeling. LANL Report, LA-14024.
- Mas, E.M., Clements, B.E., Blumenthal, W.R., Cady, C.M., Gray III, G.T., Liu, C., 2002. A viscoelastic model for PBX binders. In: M.D. Furnish, N. N. Thadhani, and Y. Horie, editors. *Shock Compression of Condensed Matter*, American Institute of Physics, New York, USA, 2002, pp. 661-664.
- Tan, H., Huang, Y., Liu, C., Geubelle, P.H., 2005a. The Mori-Tanaka method for composite materials with nonlinear interface debonding. *Int. J. Plasticity* 21, 1890-1918.
- Tan, H., Liu, C., Huang Y., Geubelle, P.H., 2005b. The cohesive law for the particle/matrix interfaces in high explosives. *J. Mech. Phys. Solids* 53, 1892-1917.
- Tan, H., Huang, Y., Liu, C., Geubelle, P. H., 2006. Effect of nonlinear interface debonding on the constitutive model of composite materials. *Int. J. Multiscale Comput. Eng.* 4, 147-167.

17th DYMAT Technical Meeting, 2007, Cavendish Laboratory, Cambridge

- Tan, H., Huang, Y., Liu, C., Inglis, H.M., Ravichandran, G., Geubelle, P.H., 2007. The uniaxial tension of particle-reinforced composite materials with nonlinear interface debonding. *Int. J. Solids Struct.* 44, 1809–1822.
- Timoshenko, S., Goodier, J.N., 1970. *Theory of elasticity* 3rd ed., McGraw-Hill, New York.
- Williams, M.L., Landel, R.F., Ferry, J.D., 1955. Temperature dependence of relaxation mechanisms in amorphous polymers and other glass forming liquids. *J. Am. Chem. Soc.* 77, 3701-3706.
- Zaug, J.M., 1998. Elastic constants of β -HMX and tantalum, equations of state of supercritical fluids and fluid mixtures and thermal transport determinations. *Proc. 11th Intl. Detonation Symp.*, Snowmass, Colorado, pp. 498-509

SIMULATION OF PBX WHEN SUBMITTED TO LOW VELOCITY MECHANICAL IMPACTS

C. GRUAU^a, D. PICART^{a*}, C. BIANCHI^b, J.P. PERLAT^b, H.J. VERBEEK^c, J.H.G. SCHOLTES^c

^a Commissariat à l'Énergie Atomique, Le Ripault, BP16, 37260 Monts (France).

^b Commissariat à l'Énergie Atomique, DAM Ile de France, BP 12, 91680 Bruyères le Châtel (France).

^c TNO Defence, Security and Safety Lange Kleiweg 137 P.O. Box 45 2280 AA Rijswijk ZH (The Netherlands).

*Corresponding author: didier.picart@cea.fr

INTRODUCTION

Low-velocity impacts followed by unintentional reactions must be taken into account in safety analyses of transport, storage and handling of explosives samples and devices. Predicting such impact consequences, like ignition, combustion or transition to detonation, is difficult due to many complex and interacting mechanisms at work. Our attention is focussed on ignition, the first event that must be predicted in a safety analysis.

The considered high explosive is composed of a polydisperse distribution of HMX grains with a mean diameter of 100 µm. These crystals are mixed with a few percentage of a polymeric binder. An isostatic compaction process is used to reduce the porosity of the composition nearby 2%. The mechanical response is close to the behaviour exhibited by PBX-9501.

Previous studies have shown that shear bands and macro-cracks can develop in the structure with respect to the impact loading conditions. On the other hand, ignition being suspected to appear in such localized areas, the choice of the numerical methods is a crucial one. This lecture describes a benchmark that has been simulated using three finite element codes: ABAQUS/Explicit, AUTODYN and HESIONE, a CEA hydrocode.

The first part of this paper is dedicated to the description of the benchmark and of the adjustments of each code.

Then, a comparative study is proposed based on the response recorded during the simulations. The plastic quantities, the forces and relative slip at some contacts, and the hourglass control methods are compared.

1. DESCRIPTION OF THE BENCHMARK AND THE CODES

1.1. Conditions proposed for the benchmark

An experimental set-up called the “Steven-test” was proposed during the 90’s to determine the behaviour of a pyrotechnic target when impacted at low velocity (see for example Chidester *et al.* 1998). A spherical nosed projectile is projected against a target composed of an explosive piece confined between two metallic plates. In order to propose a more severe loading case, a penetrating impact has been chosen to compare the codes (fig. 1).

The depth of the explosive piece is equal by 40 mm to allow the development of the shear bands and the conical punch, which appears in front of the projectile during the penetration. The diameter of the explosive part is 60 mm. A flat-nosed projectile (diameter 40 mm, height 50 mm) is used, with a one-millimetre radius at the edge. Its initial velocity is 61 m/s. The metallic confinement is composed of a back plate (10 mm thick), a front plate (15 mm thick) and the lateral confinement. Free boundary conditions have been used for the target except along the axis (symmetry).

The same mesh has been built for the three codes. Linear quadratic finite elements have been used, with a size of 0.25 mm for the PBX and the steel pieces.

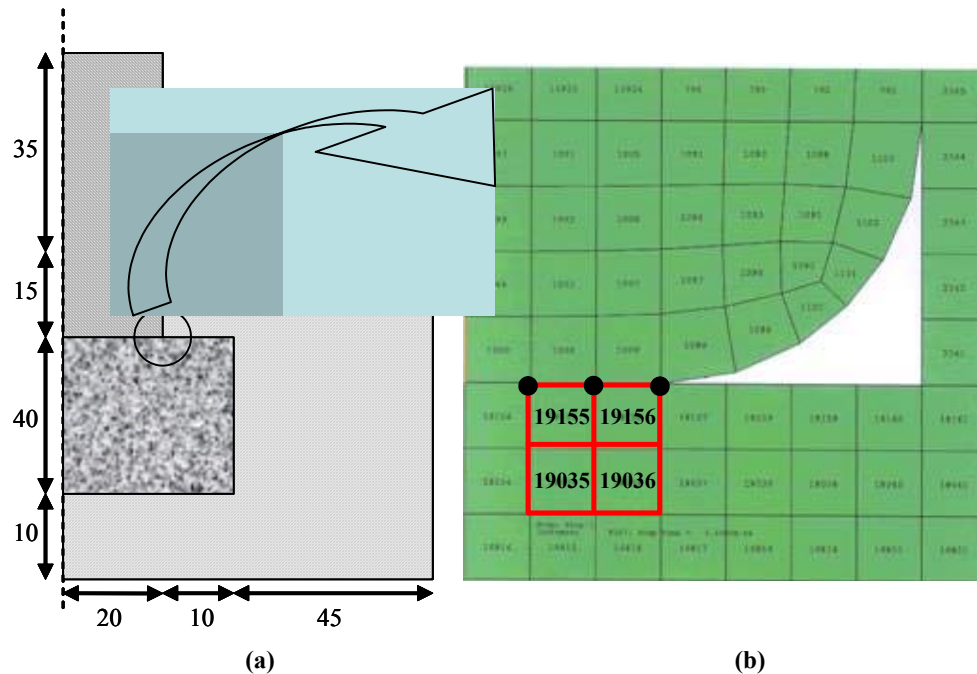


Figure 1: Description of the proposed benchmark-dimension in millimetre- (a) and the mesh used for the three codes (b).

The need of an accurate mechanical constitutive law is reinforced by the ignition threshold, which relates macroscopic mechanical states to local mechanical dissipation in hot spots (Bennett *et al.* 1998, Dienes 1984 and 1996, Browning *et al.* 2001). The behaviour of such quasi-compact material is close to the behaviour of concrete or rock-like materials for which many experimental data have been collected. Today, a convincing constitutive law has not been proposed to model the PBX behaviour. On the other hand, in order to compare the responses of the codes (and not the influence of their different constitutive laws), the benchmark has been simulated using a simple von Mises' model with a perfect plastic behaviour (table 1).

Table 1: Parameters for the von Mises perfect plasticity behaviour of the materials.

	PBX	Metallic pieces
Young's modulus (GPa)	5	210
Poisson's ratio	0.3	0.3
Elastic limit (MPa)	100	240
Density (kg/m ³)	1800	7850

The friction coefficient between PBX and metallic pieces was set to the arbitrary value of 0.2. A frictionless contact is used between the other surfaces. The separation is allowed between the surfaces in contact.

During experiments, ignition is observed just about 100 μ s after the impact. So, simulations have been run during the first 150 μ s.

1.2. The numerical codes

Three codes have been compared: ABAQUS/Explicit-6.6EF (SIMULIA), AUTODYN-2Dv11.0 (ANSYS) and a CEA/DAM hydrocode HESIONE-v4 (an example of use is given in Mariotti *et al.* 2003).

The results presented for ABAQUS and HESIONE have been obtained using a full lagrangian kinematic. For ABAQUS, the "Enhanced Hourglass Control" option is activated. For AUTODYN with the Lagrange

kinematic serious distortion of part of the grid was observed, making it necessary to rezone a small part of the grid (in the explosive near the edge of the punch). The results mentioned here have been obtained using a combination of the Lagrange and the ALE kinematic. A small number of nodes in the explosive near the edge of the punch but outside the region of interest are treated with ALE while all other nodes are treated with Lagrange kinematic (fig. 2). The automatic mesh control of ABAQUS gives a final mesh close to the one obtained with a user mesh control for AUTODYN. The mesh obtained with HESIONE is more distorted showing that this code is robust.

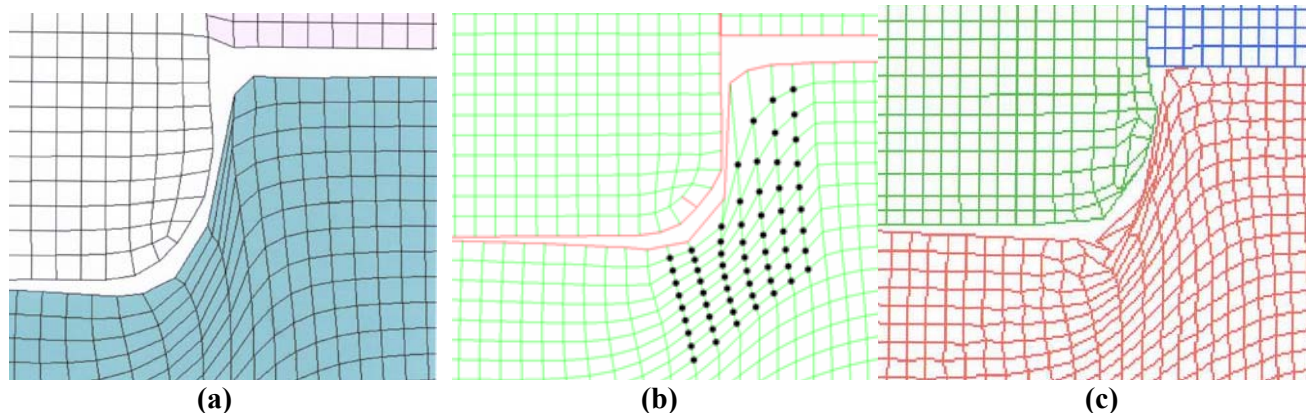


Figure 2: Deformed meshes 150 μ s after the impact using (a) ABAQUS, (b) AUTODYN and (c) HESIONE. For AUTODYN, the black dots indicate the nodes for which an ALE kinematic processor is used.

2. COMPARATIVE STUDY OF THE CODES

2.1. Preliminary remarks

The aim of our study is to predict the ignition of a pyrotechnic structure when impacted by a projectile. Several studies have been made to determine the microscopic mechanism of ignition during such loading conditions (Dienes 1996, Browning *et al.* 2001). The viscoplastic mechanical dissipation due to the implosion of the porosity is usually invoked to explain the ignition of PBX when submitted to shock conditions. The time to transition from the shock to the detonation is close to 1 μ s. Nevertheless, for low amplitude loading conditions, the friction between micro-cracks lips is a more probable candidate to explain ignition of quasi-compact material. This means that magnitudes of the pressure and of the shear strain rate, as well as the duration of the loading are crucial quantities that must be calculated with the maximum accuracy. The equivalent plastic strain and the von Mises equivalent stress have been also compared.

The capability of software to handle contact conditions has been studied, as well as the magnitude of the artificial energy for the whole model introduced to deal with the zero energy deformation modes because of the reduced integration.

The number of increments needed to solve the problem was monitored but is not reported here. Indeed, each code has its own adjustments, optimized for its usual conditions of use (shock studies, detonation, and impact). Some differences have been noticed due to these adjustments (from 0.1 to 0.25 times the critical time). However, the total duration of the simulation is qualitatively acceptable for the three codes (few hours).

2.2. Equivalent stress contours

The contours of the von Mises equivalent stress are compared in the figure 3. Ten intervals have been plotted between 0 and 100 MPa. 50 μ s after the impact, the elastic limit is reached inside a half of the

explosive piece. After 100 and 150 μs , the maximum of the stress has decreased due to the deformation of the back plate. The maximum stress is localized around the edge of the plunger at 150 μs .

The contours look similar at 50 μs for the three codes if the second level (orange) is adopted for AUTODYN. For the later times, AUTODYN is close to ABAQUS and a slight difference appears with HESIONE at the edge.

Using coloured plots, some bands have been observed with alternative colours (fig. 4). These artificial “oscillations” (chessboard pattern) are related to the reduced integration algorithm used here and the low level of the interpolation that is possible using constant stress finite elements. This observation shows that the use of fully integrated finite elements for explicit codes would be appreciated, this technique being not available in the selected codes.

2.3. Equivalent plastic strain

A comparison of the equivalent plastic strain is proposed at the end of the simulation (fig. 5). Open contact are observed between the explosive part and the front and back plates. As the front plate is not deformed, the back plate is submitted to a bend moment. A low-level of strain is observed inside this plate.

As it is observed in the figure 5, the energetic material is not flowing inside the gap formed between the projectile and the front plate. Sometime such a mechanism is invoked to explain ignition of pyrotechnic structures when submitted to high deformation and finite strain.

Due to the perfect plastic flow rule, the maximum of the equivalent plastic strain is localized at the edge of the projectile. The maximum propagates towards the core of the target. The contours have been plotted between 0 and 10% of strain. For example, the maximum is reached at the edge and is close to 236%. Strain exceeding 10% are also reached in the right bottom edge of the explosive piece. The three codes give the same result at the edge. AUTODYN and HESIONE show a band developing at the right side of the explosive piece, and the same response at the contact with the projectile (red area at the middle of the radius of the projectile in HESIONE simulation).

It would be profitable to zoom close to the edge and to analyse the strain gradient in this area. However, due to the sensitivity of the results to the numerical methods used (ALE, hourglass control...), the comparison would be difficult to analyse.

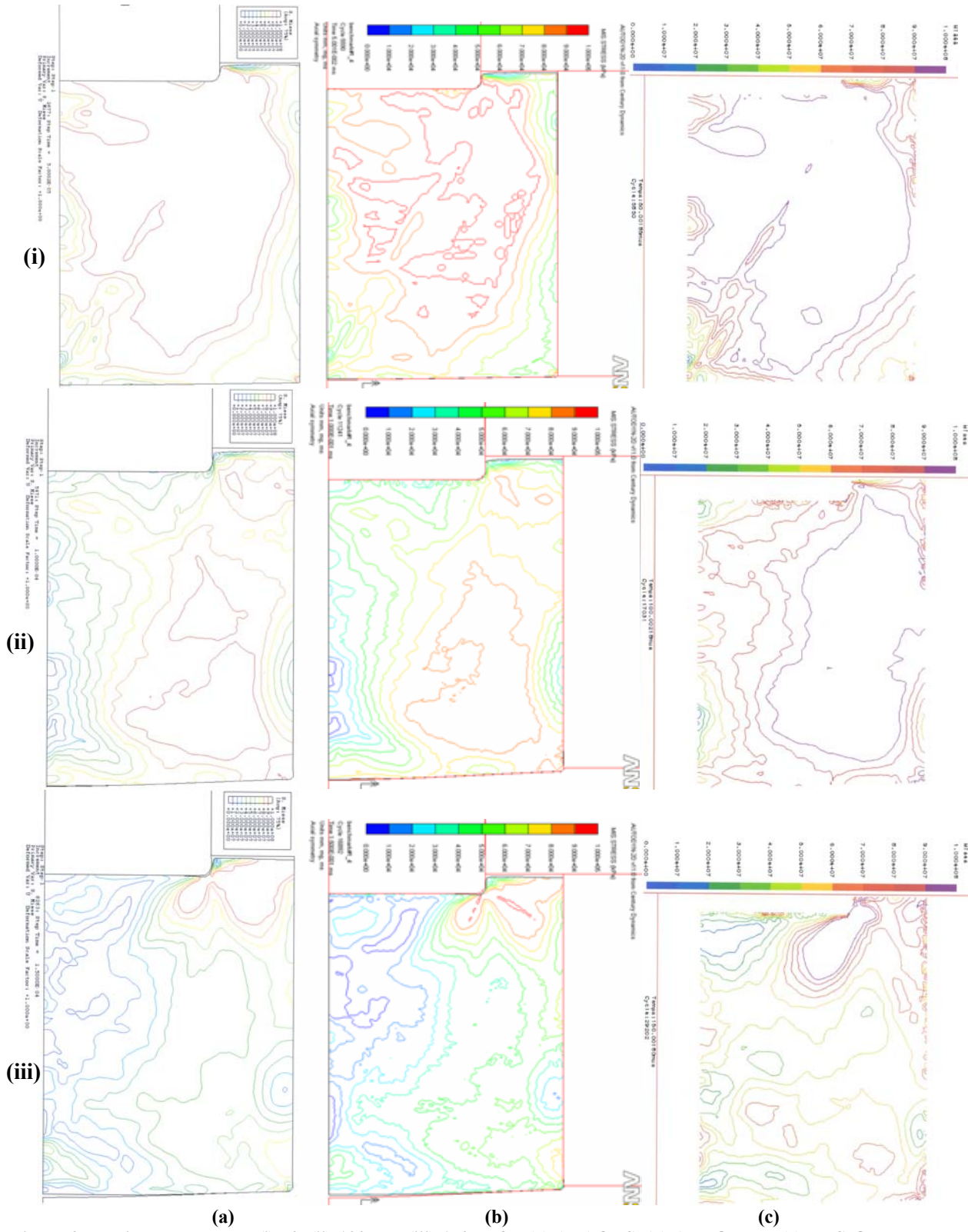
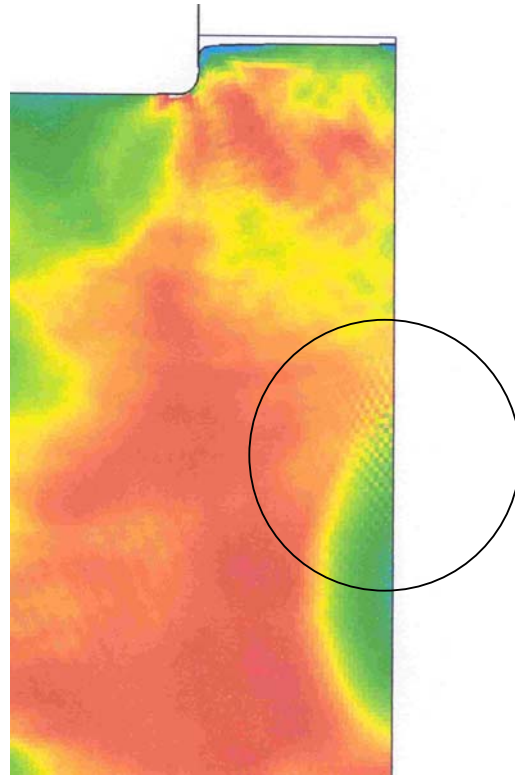


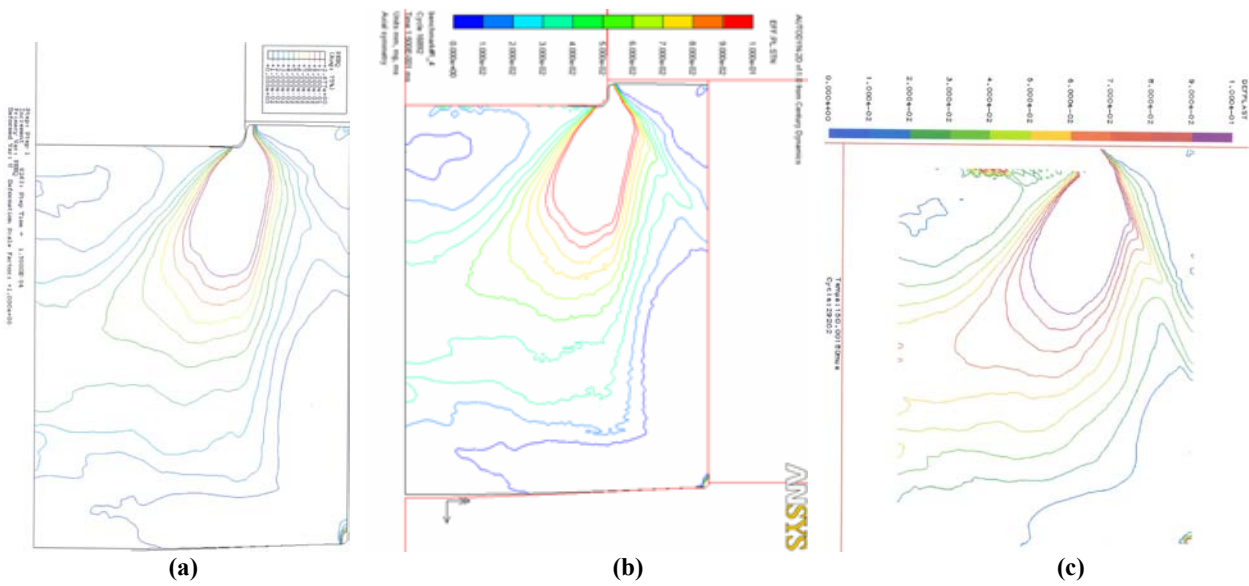
Figure 3: Equivalent stress at (i) 50, (ii) 100 and (iii) 150 μ s for (a) ABAQUS, (b) AUTODYN, (c) HESIONE. Due to post-processor differences, it is not possible to adopt the same colours for the contours.



(a)

(b)

Figure 4: An example of von Mises stress with oscillating “chessboard” pattern using (a) ABAQUS. These patterns are observed using the three codes.



(a)

(b)

(c)

Figure 5: Equivalent plastic strain at 150 μ s for (a) ABAQUS, (b) AUTODYN, (c) HESIONE.

2.4. Pressure and equivalent shear stress histories

The response of four finite elements has been monitored during the simulations. These elements are located under the projectile, inside the explosive part and close to the edge (see the elements with red boundaries in the figure 1).

After a rapid pressure drop (which is captured equally by the codes), the pressure is close to 250 MPa at 60 μs (fig. 6). This level is higher than the pressure measured during a classical Steven-test (about 150 MPa at 60 μs). The codes give same results except the duration of the maximum level stage, which takes 40, 45 or 55 μs respectively using ABAQUS, AUTODYN and HESIONE. For the four elements and close to 60 μs , the maximum difference is 25 to 40 MPa with ABAQUS and AUTODYN, and 80 MPa with HESIONE. The behaviour is similar for the four elements in ABAQUS during the decrease of the pressure when some differences can be observed with the two other codes. The ultimate values of the pressures are comparable.

The elastic limit is reached suddenly after the impact (fig. 7). For these four elements, the value remains constant during the penetration except around 100 μs . Until 100 μs , the stress is between 80 and 100 MPa. AUTODYN shows a lower value at 25 μs for one element. The sudden decrease of the stress at 100 μs is the same for ABAQUS and AUTODYN except a delay in time. Some differences are observed between ABAQUS and AUTODYN for the final values, which are ranging from 90 to 100 MPa for ABAQUS and 75 to 100 for AUTODYN.

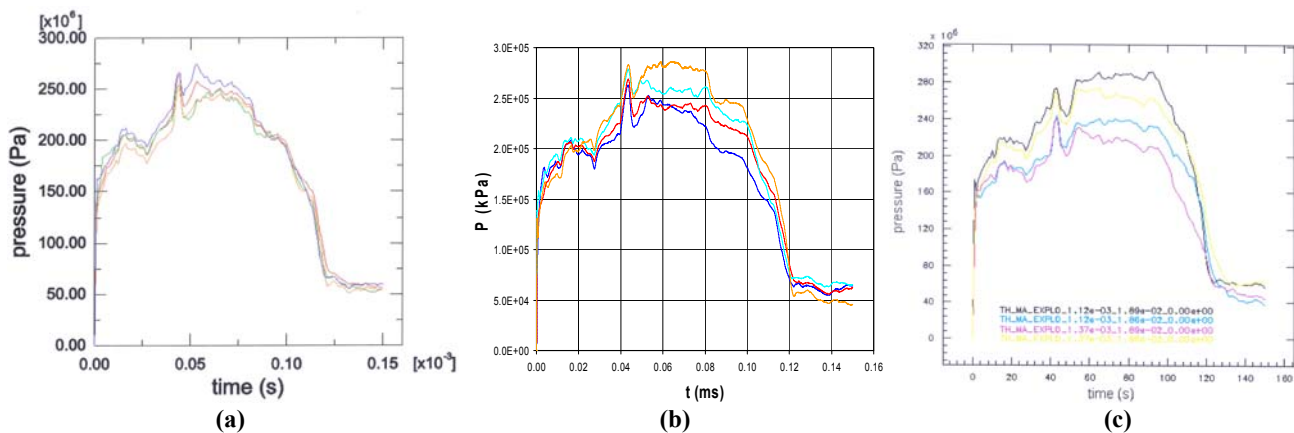


Figure 6: Pressure versus time for (a) ABAQUS, (b) AUTODYN, (c) HESIONE.

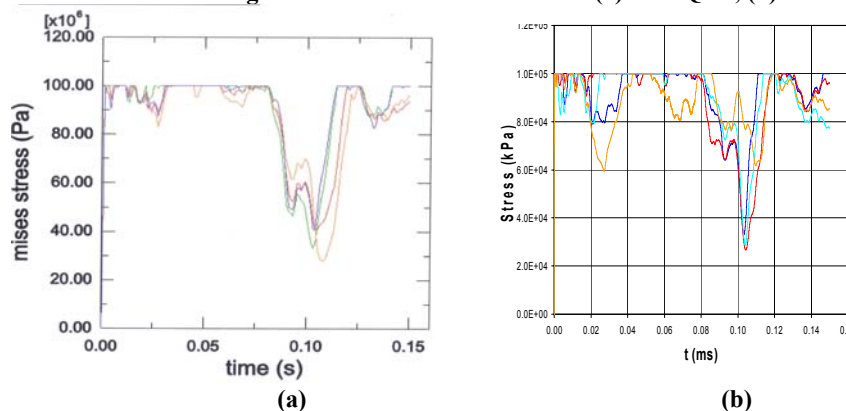


Figure 7: Equivalent stress versus time for (a) ABAQUS, (b) AUTODYN.

2.5. Equivalent plastic strain rate

The equivalent plastic strain rate is given for the four finite elements in the figure 8. A zoom of the first 100 μs is given for the AUTODYN response. At the impact, the maximum of the equivalent plastic strain rate is the same for ABAQUS and HESIONE when AUTODYN produces a value two times higher than the other codes. Again, at 50 and 120 μs , ABAQUS and HESIONE give comparable results.

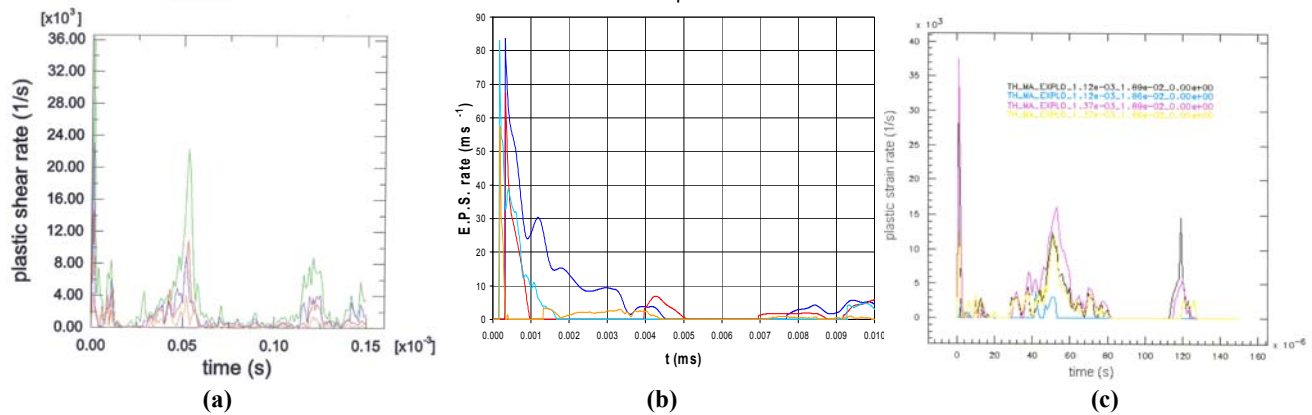


Figure 8: Equivalent plastic strain rate versus time for (a) ABAQUS, (b) AUTODYN, (c) HESIONE.

2.6. Contact conditions

To compare how the codes handle contact boundary conditions, the contact forces and the relative displacements have been plotted for three nodes located between the projectile and the pyrotechnic piece (see the location of the black nodes in the figure 1). This analysis was not made using HESIONE.

Again, after the first microseconds, the contact forces have a constant value (fig. 9). The levels reached by ABAQUS and AUTODYN differed significantly by a ratio of almost two. This difference is unexplained and can be due to different numerical methods or to different output quantities determined at the nodes. The forces decrease as the finite element arrived inside the gap formed around the edge of the projectile.

In ABAQUS, a constant value of the relative slip is kept after the separation of the two materials. Strong differences are observed between ABAQUS and AUTODYN. For ABAQUS, the nodes that are face to face give a zero relative slip displacement at the beginning, when the nodes in AUTODYN are not placed at the same spatial location (negative value of the relative position of the nodes at the beginning). For the nodes located in the middle and the left side of the mesh, a constant value is observed in ABAQUS at 120 μ s. At this time, the PBX and the projectile are separated. When ABAQUS give different values for the relative slip for the two nodes (16 and 28 μ m), AUTODYN indicates a zero relative displacement meaning 10 μ m (after correction of the initial value). The observed differences could be explained by the used or not of ALE method near these nodes, or a different method to deduce the quantities in ABAQUS.

2.6. Hourglass control

Explicit finite element codes usually propose a reduced integration method that must be corrected using hourglass control techniques, to avoid zero energy deformation modes. The total energy of the whole model has been compared to the artificial energy (fig. 10).

A perfect agreement is obtained between AUTODYN and ABAQUS for the total energy. The comparison with HESIONE shows some slight differences. The minimum energy is recorded at 100 μ s for ABAQUS and 90 μ s for HESIONE, when the final energies are different.

The amount of artificial energy being negligible compared to the total energy of the model, it could be concluded that the hourglass control method does not influence the results even if some differences are observed between ABAQUS and HESIONE. The hourglass energy dissipated by AUTODYN is remarkably low (one order of magnitude less than ABAQUS and HESIONE).

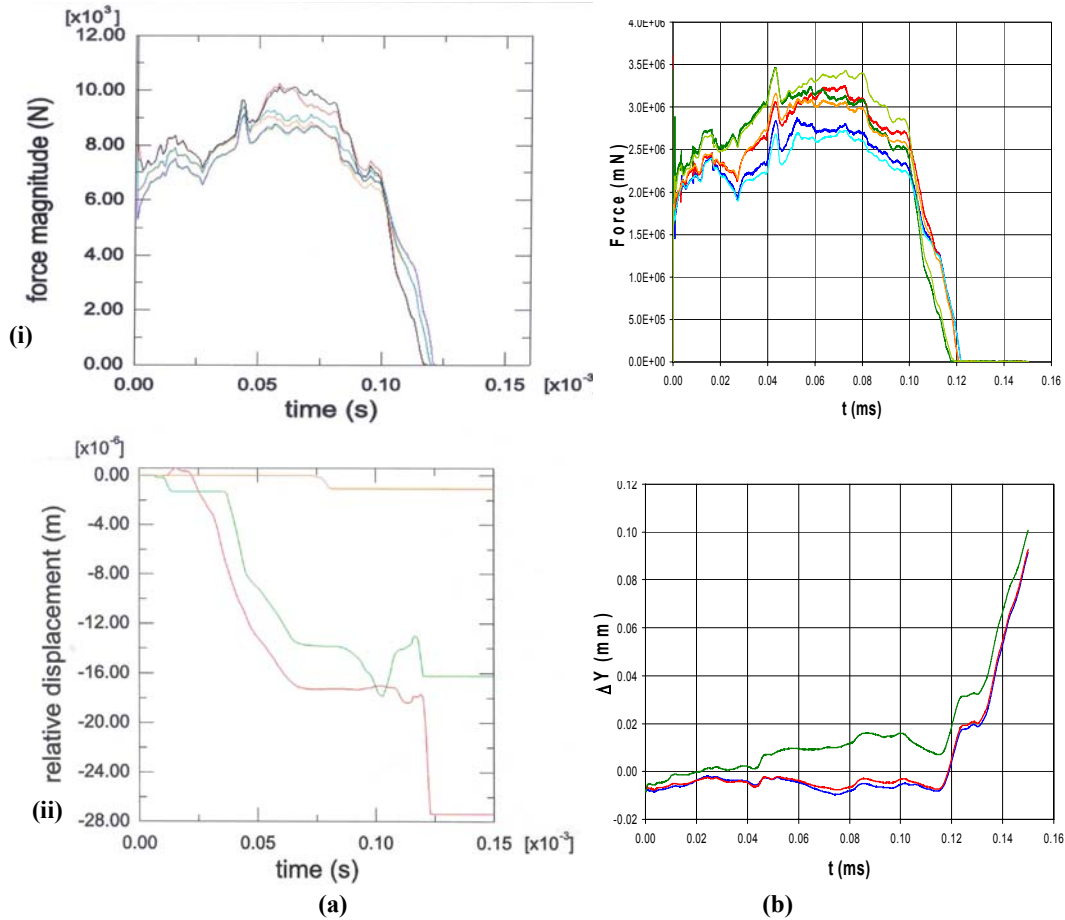


Figure 9: Contact forces (i) and relative slip displacement at contact (ii) for (a) ABAQUS, (b) AUTODYN.

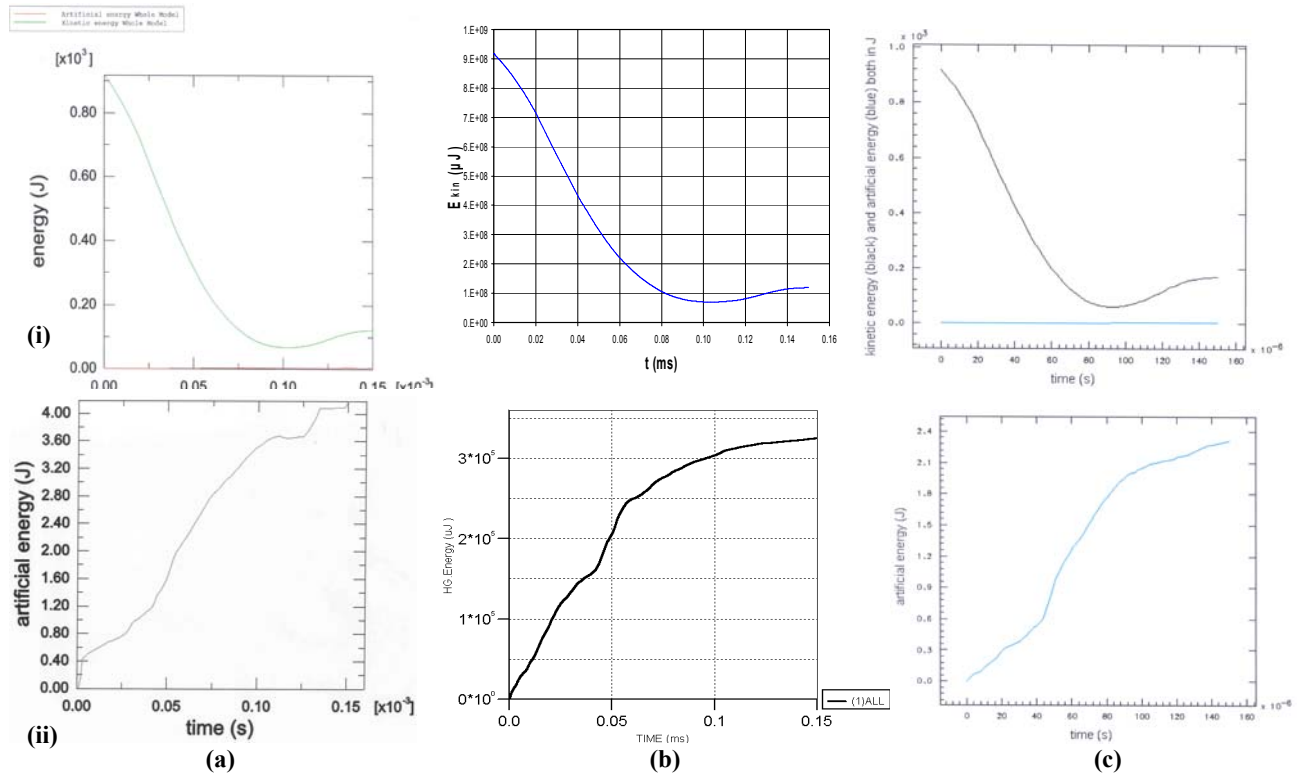


Figure 10: Total (i) and artificial (ii) energies for (a) ABAQUS, (b) AUTODYN, (c) HESIONE.

CONCLUSION

The prediction of unintentional reactions induced by low-velocity impacts will be possible only using a complete set of tools involving a dynamic mechanical constitutive law of the PBX, a method to determine the energy dissipated at the microstructural level and an ignition threshold. These predictions will be possible only using a numerical code to deal with the heterogeneous fields of stress and strain generated by the impact. The choice of the numerical tool is then a crucial one.

Ignition being suspected to happen at most 100 to 150 μs after the impact, a finite element method is the best compromise to model the deformation of the target. A first benchmark has been run between three finite elements codes: ABAQUS/Explicit, AUTODYN and HESIONE, a CEA hydrocode.

Almost all the data collected for the codes show a relatively good agreement. The three codes show “oscillating” value (chessboard pattern) of the stress probably related to the reduced integration scheme used to decrease the duration of the simulations. To reach an accurate prediction of the ignition of the PBX, complete integrated finite elements would be appreciated.

Some differences have been observed, the major ones related to the contact conditions between the projectile and the PBX piece (between ABAQUS and AUTODYN). It could be assume that the use of ALE method, near the region of interest, leads to different results in term of displacement field.

It would be interesting to compare now these codes to experimental data in order to determine the best code for our problem. Unfortunately, the mechanical behaviour of the PBX is unknown especially for coupled high pressure and high strain rate loading conditions.

REFERENCES

- Bennett, J., K. Haberman, J. Johnson, B. Asay, B. Henson (1998), *A constitutive model for the non-shock ignition and mechanical response of high explosives*, J. Mech. Phys. Solids **46** 2303-2322.
- Browning, R. and R. Scammon (2001), *Microstructure model of ignition for time varying loading conditions*, Shock Compression of Condensed Matter, eds M. Furnish, N. Thadhani and Y. Horie, 987-990.
- Chidester S.K., Tarver C.M., Garza R. (1998), Low amplitude impact testing and analysis of pristine and aged solid high explosives, Eleventh International Symposium on Detonation, ONR 33300-5, pp. 93-100, publ. Office of Naval Research, Arlington, VA (USA).
- Dienes, J. (1984), *Frictional hot-spots and propellant sensitivity*, Mater. Res. Soc. Symp. Proc. **24** 373-381
- Dienes, J. (1996), *A unified theory of flow, Hot spots, and fragmentation with an application to explosive sensitivity*, in High Pressure Shock Compression of Solids II, eds L. Davison et al., pp. 366-398, publ. Springer
- Mariotti, C., J.P. Perlat, J.M. Guérin (2003), *A numerical approach for partially saturated geomaterials under shock*, Int. J. Impact Engng **28** 717-741.

Charge and excitation-triggered decomposition of DADNE

Anna V Kimmel^{1,2}, Peter V Sushko², Alexander L Shluger² and Maija M Kuklja^{1,3}

¹ Department of Physics, University of Nevada Las Vegas, NV 89154, USA

² London Centre for Nanotechnology, Department of Physics and Astronomy,
University College London, Gower Street, London WC1E 6BT, UK

³ Division of Materials Research, National Science Foundation, Arlington, VA 22203, USA

PACS numbers:

64.30.+t, 61.66.Hq, 62.50.+p

Keywords: 1,1-diamino-dinitroethylene, DFT, decomposition, electronic excitation, charge trapping

discuss how those dissociation processes can be stimulated by mechanical defects or deformations in line with other types of external stimuli.

I. ABSTRACT

We have studied the electronic structure of a 1,1-diamino-2,2-dinitroethylene molecule (DADNE) in the gas phase and its possible dissociation pathways. It is shown that charging and excitation may not only reduce the activation barriers for decomposition reactions, but also change the dominating chemistry from endo- to exothermic type. Two competing primary initiation mechanisms of FOX-7 decomposition were found: C-NO₂ bond fission and C-NO₂ to CONO isomerization. We discuss how these excitations can be stimulated by mechanical deformations introduced by a shock wave in a solid material.

II. INTRODUCTION

The macroscopic properties of energetic materials (EM) are well established, especially in the gas and liquid phases. However, the microscopic details of the detonation initiation process are not well understood due to both the complexity of the structures of EM and the insufficient experimental tools to study the initiation in situ. Theoretical and computational studies can provide vital insights into the mechanisms of these processes in collaboration with high quality experiments. Our major goal is to study different conditions in EM that may affect (that is facilitate or preclude) the decomposition of constituting molecules including high pressure, high temperature, mechanical deformations, structural and electronic defects, as well as their combinations and interactions in solid EM. In other words, we aim at fundamental understanding of initiation of detonation in energetic crystals from solid state physics and chemistry points of view. We believe that the results obtained from quantum mechanical and multi-scale modeling can clarify the nature of hot spots and details of the initiation mechanisms triggered by the shock wave as well as the conditions for sustained chain reaction leading to detonation and explosion.

In this paper, we focus on decomposition pathways of DADNE from its ground, excited, and charged states and

III. BACKGROUND AND MOTIVATION

The 1,1-diamino-2,2-dinitroethylene, C₂H₄N₄O₄, also known as DADNE, a recently synthesized molecular energetic material [1–3], was selected because of its relative simplicity and its expected low sensitivity to initiation. More generally, this material can serve as a good model for elucidating mechanical, chemical, and optical properties of a wide class of nitroarenes.

One of the immediate, although difficult to simulate, properties of EM exposed to the shock or impact wave is its hydrostatic and/or uniaxial mechanical compressibility and equation of state. Recent studies [4–7] confirmed that much less energy is required to move molecules within the crystalline lattice due to compression than to change intramolecular configurations of individual molecules. It has also been shown for several materials that in a perfect crystal hydrostatic compression narrows the band gap instantaneously [8–10], but it tends to regain its equilibrium value if the system is let to relax [11, 12]. More so, high pressure alone cannot produce any additional states in the band gap [7–9, 12, 13]. It has been noted, however, that some structural defects (e.g. dislocations, grain boundaries, disclinations, and stacking faults [13, 14]) and mechanical deformations (local stress and shear-strain [11, 12, 15]) create localized electronic states in the band gap and thus reduce the value of the gap.

In particular, it has been shown [13] that the edge dislocations in solid explosive RDX and PETN crystals produce electronic states in the band gap. The local defects in the crystalline structure, such as a molecule with a reversed orientation, a dislocation core or grain boundary [12–14, 16], affect the electronic structure and decomposition barriers of crystalline DADNE. It was found that the band gap is reduced by changing the hybridization between the N-*p* and O-*p* molecular orbitals, thereby introduces new local electronic states [16]. Furthermore, the *ab initio* studies of crystalline DADNE have found that highly anisotropic electrical and thermal conductivity are likely to occur due to shear strain in this material [12]. Therefore it could be expected that electronic excitations in deformed material could differ from those in the perfect solid.

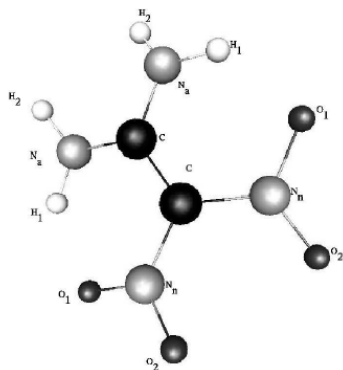


FIG. 1: The structure of 1,1-diamino-2,2-dinitroethylene (DADNE). In the ground state, a DADNE molecule has a non-planar configuration with non-zero torsion angles between nitrogen atoms from amino-groups, and those from nitro-groups.

To elucidate the role of the electronic excitations and trapped charges in decomposition mechanisms of DADNE we have carried out *ab initio* calculations of individual DADNE molecule in different excited and charge states. Although our results cannot be directly extrapolated to practical solid explosives, they provide useful information regarding the role of electronically excited states in decomposition chemistry of these materials.

IV. COMPUTATIONAL DETAILS

We used Density Functional Theory (DFT) and the hybrid B3LYP density functional [21, 22] to calculate the electronic structure of individual molecules. This method has been widely used for simulating organic molecules in general, and nitro-compounds in particular, and proved to be reliable in calculations of atomization energies, reaction activation energies and energy balances. The electronic structure of the DADNE molecule and its fragments as well as the barriers for molecular decomposition were calculated using the Gaussian03 code [23] and 6-31+G(d,p) Gaussian-type basis sets. Vibrational frequencies have been calculated for relevant atomistic configurations so that to distinguish energy minima and transition states and to determine corresponding zero-point energy corrections (ZPEC). All the stationary states have no imaginary frequencies. The transition states (TS) were calculated using the synchronous quasi-Newton method as implemented in the Gaussian03 code [23] and confirmed to have only one imaginary frequency.

V. CHEMICAL REACTIONS INVOLVING CHARGED AND EXCITED STATES

The structure of the ground state DADNE molecule, ionized $[\text{DADNE}]^+$ and negatively charged $[\text{DADNE}]^-$ radicals, and the lowest triplet excited state have been

carefully studied [18, 19]. Positively charged ion has two stable configurations with similar energies and different geometries, which we denote h_a and h_p . The corresponding structures are described in great detail elsewhere [18].

In order to reveal the effect of excited and charged states of DADNE on its decomposition mechanisms, we simulated relevant processes, such as rupture of C-NH₂, C-NO₂, and C=C bonds as well as CONO- and HONO-isomerizations. We found that C-NH₂ and C=C bond ruptures as well as HONO isomerization are not favorable decomposition pathways of DADNE. However, presence of electrons may change energetics and make those reactions feasible [18, 19]. Thus, dissociation of a $[\text{DADNE}]^+$ radical via C=C break requires only 63.8 kcal/mol, much lower than 120.2 kcal/mol in the ground state. Also, in $[\text{DADNE}]^-$, the trapped electron is distributed over nitro-groups, which provides extra attraction between protons and oxygen atoms. This makes the exothermic HONO arrangement possible with the small energy gain of 3.25 kcal/mol and a relatively low barrier of 29.76 kcal/mol.

We found that C-NO₂ bond fission reaction is an endothermic reaction that requires 66.98 kcal/mol, which is in good agreement with 70 kcal/mol from previous calculations [24] and experimental results for nitro-compounds [17]. In the case of positively charged $[\text{DADNE}]^+$, the cleavage of a C-NO₂ bond becomes exothermic with the energy gain of 27.67 kcal/mol for the h_a configuration and 8.08 kcal/mol for the h_p configuration while the barriers for these reactions are 54.71 and 59.10 kcal/mol, respectively.

The decomposition of negatively charged $[\text{DADNE}]^-$ is endothermic with the dissociation energy of 14.48 kcal/mol and the barrier of only 20.62 kcal/mol. Such a significant reduction of the barrier is due to a larger repulsion between nitro-groups accommodating an extra-electron.

In the triplet state of DADNE molecule, the C-NO₂ bond cleavage is also endothermic with the calculated dissociation energy of 12.44 kcal/mol and the barrier of 32.97 kcal/mol.

We confirm that the homolytic C-NO₂ cleavage is a plausible initial decomposition reaction in DADNE. In addition, we reveal that the barrier for this reaction becomes significantly lower in the electronically excited and charged states of the molecule. The presence of NO registered in final products of the decomposition of nitro compounds suggests that the isomerization of C-NO₂ to a C-ONO and/or other intra-molecular rearrangements should take place prior to the decomposition [26] (Fig. 4a). The nitro-nitrite rearrangement followed by CO-NO bond homolysis is now recognized as a feasible step in the thermal decomposition of nitro-aromatic explosives [17]. In our simulations, formation of a stable CONO isomer in the neutral DADNE molecule is an exothermic reaction with a small energy gain of 4.1 kcal/mol. The calculated barrier for this transformation is 63.5 kcal/mol and the transition state is characterized by a geometry in which one nitro-group is rotated with respect to the molecular plane. After the CONO-isomer is formed, the

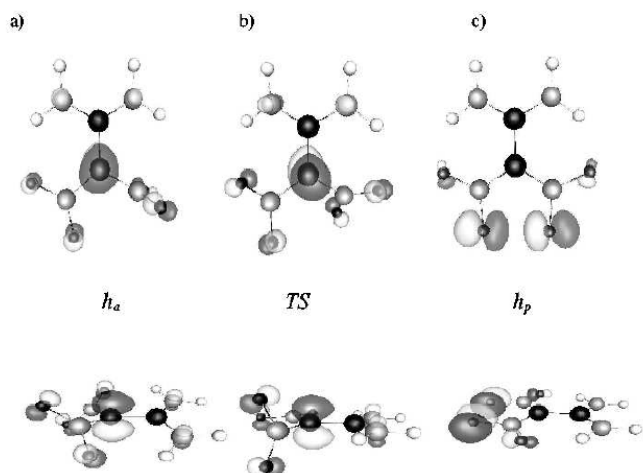


FIG. 2: The structure of $[\text{DADNE}]^+$ molecule, h_a and h_p , and the transition state (TS). a) In the h_a state, the hole is localized on the C atom attached to the nitro-groups, and partially distributed over O atoms of the nitro-groups. b) In the transition state between h_a and h_p , one of the nitro-groups remains within the molecular plane, while the other is oriented perpendicular to it. c) In the h_p state, the hole is localized on collinear p -orbitals of O atoms of the nitro-groups. The h_p configuration is characterized by nearly flat geometry.

CO-NO bond can be cleaved releasing the NO species (see Fig. 4a). The calculated barrier for this reaction is 27.4 kcal/mol and the overall energy gain is 6.6 kcal/mol, which is consistent with the previously reported results [25].

Importantly, we found that the NO species can detach spontaneously once the molecule is charged or excited. Indeed, an additional electron can be trapped by the CONO fragment. The vertical electron affinity of the unrelaxed negatively charged CONO isomer of DADNE molecule is 22.6 kcal/mol. This configuration then relaxes with the spontaneous NO detachment and overall energy gain of 23.8 kcal/mol (with respect to the energy of the negatively charged CONO isomer of the DADNE). Alternatively, an ionization of the molecule (calculated vertical IP is 191.6 kcal/mol, or 8.31 eV) also results in the spontaneous NO detachment with an energy gain of 27.7 kcal/mol (with respect to the energy of the positively charged CONO isomer). It follows from our calculations that isomerization of C-NO₂ to C-ONO does not occur for charged DADNE molecules.

Finally, we note that since the barriers of C-NO₂ to CONO isomerization and C-NO₂ rupture occurring from the singlet and triplet states are comparable, both of these processes are likely to take place at the early stage of the decomposition, which is consistent with the observed existence of both NO and NO₂ products in the mass spectra of DADNE [2]. We predict that once the CONO isomer is formed, trapping of a negative or positive charge as well as photo-excitation will result in a spontaneous detachment of NO specie.

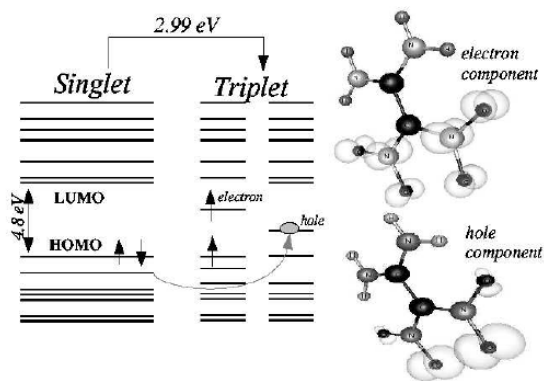


FIG. 3: Schematic energy diagram of the lowest excited triplet state of DADNE molecule. The electron component is localized on nitro-groups and occupies the states perpendicular to the molecular plane. The hole component is localized on the oxygen atoms of the same nitro-groups, but occupies the collinear p -orbitals oriented in the molecular plane.

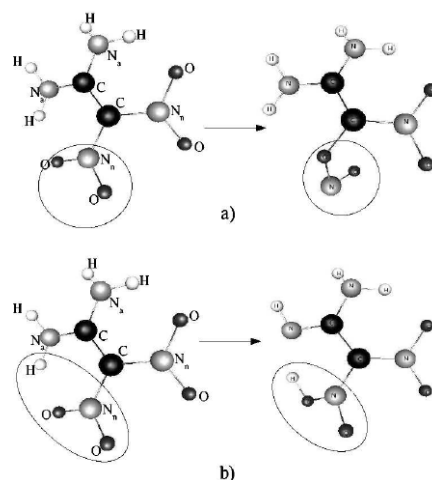


FIG. 4: a) Nitro-nitrite isomerization of DADNE molecule involves rearrangement of one nitro-group with creation of a CONO chain. b) HONO rearrangement occurs due to intramolecular hydrogen migration from amino- to nitro-group.

VI. DISCUSSION AND CONCLUSIONS

In this work, we have considered possible decomposition reactions of the DADNE molecule in the ground as well as charged and excited states. We found that the excitation may not only change the energetics of chemical reactions by reducing the reaction barriers, but also change the type of the dominating chemistry from endothermic to exothermic. Based on our results, we suggest that the C-NO₂ scission and C-NO₂ to CONO isomerization are two competing mechanisms of DADNE dissociation. This conclusion reconciles the seemingly contradictory theoretical predictions [24, 25] and also may help to explain experimental observations [2, 26].

More importantly, our calculations demonstrate that

the excitation and charging of the molecule can have a dramatic effect on the decomposition process by facilitating some mechanisms of dissociation and precluding the others on the example of intro-initrite isomerization reaction. Although calculated for an isolated DADNE molecule, these results should be useful for understanding reactions in solid DADNE because in this molecular crystal molecules are bound via weak electrostatic and van der Waals interactions [2, 6], and the electronic states are mostly defined by intramolecular interactions and are localized on individual molecules [12, 15]. In such materials isotropic or uniaxial stress applied to the perfect lattice accumulates elastic energy without any chemical or significant electronic structure modifications [12, 14]. However, the presence of structural defects, such as dislocations [13], local stress deformations [14], and shear strain deformations [12] lead to modifications of the electronic structure, such as band gap narrowing and appearance of defect levels in the gap. These modifications, in turn, can stimulate formation of excitons as well as charge trapping in the system. In this paper, on the example of isolated DADNE molecule, we have demonstrated that electronic

defects can play a significant role in initiating chemistry by triggering some dissociation channels and breaking the others. Our further studies of the role of electronic excitations in initiation processes in the solid phase will focus on the decomposition of electronically excited molecules in the vicinity of a dislocation core or grain boundary [20].

VII. ACKNOWLEDGMENTS

This work is supported in part by the USA ARO MURI under Grant #W9011NF-05-1-0266. PVS is supported by the Grant-in-Aid for Creative Scientific Research under Grant No. 16GS0205. from the Japanese Ministry of Education, Culture, Sports, Science and Technology. M.K. is grateful to the Division of Materials Research of NSF for support under the Independent Research and Development Program. Any appearance of findings, conclusions, or recommendations, expressed in this material are those of the authors and do not necessarily reflect views of the National Science Foundation.

-
- [1] N. V. Latypov, J. Bergman, A. Langlet, U. Wellmar and U. Bemm, *Tetrahedron* **54**, 11525 (1998).
- [2] H. Ostmark, A. Langlet, J. Bergman, U. Wellmar and U. Bemm, 11th International Sy Detonation, Office of Naval Research, **ONR 33300-5**, 807 (1998).
- [3] U. Bemm, H. Ostmark, *Acta Crystallography* **C54**, 1999 (1997).
- [4] F. J. Zerilli, M. M. Kuklja, *J. Phys. Chem. A*, **111** (9), 1721 (2007).
- [5] F. J. Zerilli, M. M. Kuklja, *J. Phys. Chem. A*, **110**, 5173 (2006).
- [6] F. J. Zerilli, M. M. Kuklja, S. M. Peiris, *J. Chem. Phys.*, **118**(24), 11073 (2003).
- [7] F. J. Zerilli, J. P. Hooper, M. M. Kuklja, *J. Chem. Phys.*, **126**, 114701 (2007).
- [8] M. M. Kuklja, *Applied Physics A-Materials Science and Processing*, **76**(3), 359 (2003).
- [9] M. M. Kuklja, A. B. Kunz, *J. Appl. Phys.*, **86**, 4428 (1999).
- [10] E. J. Reed, J. D. Joannopoulos, L. E. Fried, *Phys. Rev. B*, **62** (24), 16500 (2000).
- [11] M. M. Kuklja, S. Rashkeev, *J. Appl. Phys. Lett.*, **90**, 151913 (2007).
- [12] M. M. Kuklja, S. Rashkeev, *Phys. Rev. B*, **75**, 104111 (2007).
- [13] M. M. Kuklja, A. B. Kunz, *J. Appl. Phys.*, **89**, 4962 (2001).
- [14] M. M. Kuklja, S. Rashkeev, F. Zerilli, *J. Appl. Phys. Lett.*, **82**, 1371 (2003).
- [15] M. M. Kuklja, S. Rashkeev, F. Zerilli, *J. Appl. Phys. Lett.*, **82**, 071904 (2006).
- [16] M. M. Kuklja, *APS Conference Proceedings, in Shock Compression of Condensed Matter*, edited by M. D. Furnish, N. N. Thadhani, and Y. Horie, American Institute of Physics, **620**, 454 (New York, 2002).
- [17] T. B. Brill, K. J. James, *J. Phys. Chem.*, **97**, 8752 (1993).
- [18] A. V. Kimmel, P. V. Sushko, A. L. Shluger, M. M. Kuklja, *J. Chem. Phys.*, **126**(23), 234711 (2007).
- [19] A. Kimmel, P. Sushko, A. Shluger, M. Kuklja, *AIP Conference Proceedings*, Editors: M. L. Elert, M. D. Furnish, R. Chau, N. Holmes, J. Nguyen, **submitted**, (2007).
- [20] A. Kimmel, P. Sushko, A. Shluger, M. Kuklja, to be published (2007).
- [21] A. D. Becke *J. Chem. Phys.*, **98**, 5548 (1993).
- [22] C. Lee, W. Yang, R. G. Parr, *Phys. Rev. B*, **37**, 785 (1988).
- [23] J. Frisch et al., *GAUSSIAN 03*, Pittsburgh, PA: Gaussian (2003).
- [24] P. Politzer, M. C. Concha, M. E. Grice, P. Lane, D. Habbalazadeh, *J. Mol. Str.*, **75**, 452 (1998).
- [25] A. Gindulyte, L. Masaa, L. Huang and J. Karle, *J. Phys. Chem. A.*, **103**, 11040 (1999).
- [26] H.-X. Gao, F.-Q. Zhao, R.-Z. Hu, Q. Pan, B.-Z. Wang, Y. Gao, and S.-L. Gao, *Chinese J. Chem.*, **24**, 117 (2006).

Morphological Analysis of 3D images of pyrotechnical granular materials obtained by microtomography

Dominique Jeulin (1), Thomas Clemenceau (1, 4), Matthieu Faessel (1), Vincent Tariel (1, 2), Gérald Contesse (3), Alain Fanget (3)

- (1) Centre de Morphologie Mathématique, Ecole des Mines de Paris, 35 rue Saint-Honoré, F77300 Fontainebleau, France
- (2) Laboratoire de Physique de la Matière Condensée, UMR CNRS 7643, Ecole Polytechnique, F91128 Palaiseau Cedex, France
- (3) DGA, Centre d'Etudes de Gramat, F46500 Gramat
- (4) Université Paris XIII

Key words: X-ray microtomography, 3D imaging, granular media, image segmentation, mechanical behaviour

Abstract

The modeling of the mechanical behavior of granular media can be based on a precise geometrical description, when coupling Finite Element calculations and 3D images of the grains, obtained by microtomography.

Progress in the area of imaging allowed the development of commercial tomographs with a resolution of the order of the micron. Algorithms are now available to reconstruct the morphology in 3D and to efficiently perform a 3D image processing.

We studied composites with polymeric matrix (pyrotechnical materials) containing grains of sizes and shapes changing on a macroscopic scale.

Because of the conditions of acquisition, the available images are not exploitable without a reliable method of extraction of the grains. After the three-dimensional reconstruction, contours of the grains are extracted using a morphological segmentation, the watershed algorithm implemented in 3D. A robust multi-scale segmentation was developed and validated. The algorithms of image processing were written using the software APHELION[®].

On the extracted grains, a whole set of morphological measurements (covariance, granulometry 3D connectivity, ...) are performed in order to get a quantitative description of the granular media. Then the 3D map of the microstructure can be meshed, for a numerical calculation of homogenisation of its mechanical properties using a Finite Element code.

This is a first step in the prediction of the macroscopic behaviour and for the optimisation of the pyrotechnical properties by controlling the microstructure.

Introduction

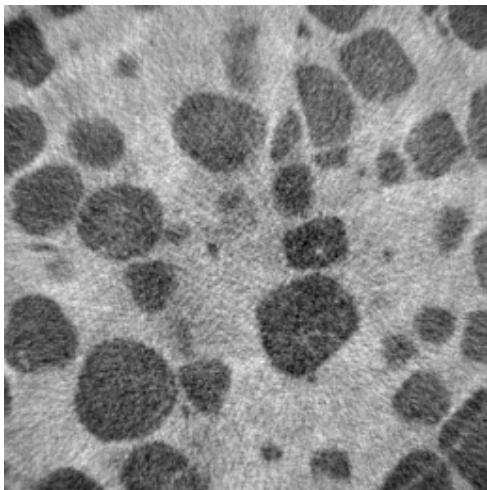
In order to master the safety of energetic materials, it is necessary to have a deep knowledge of the physical processes involved in the use of the aging of these materials. This can be reached from information on the microstructure of materials. To fulfil this task, the Centre d'Études de Gramat (CEG) uses a X-Ray microtomograph system designed by Skyscan[®]. This instrument provides 3D images of materials on a mesoscopic scale. Combined with appropriate image analysis tools, it enables us to obtain 3D information on the morphology of materials. In this presentation, examples of image segmentation and of morphological

characterization of pyrotechnical granular materials are given. In a next step, it is possible to generate 3D meshes on images for further analysis of the behaviour of granular materials by Finite Elements calculations, and to generate models of random media for microstructure optimisation with respect to their properties.

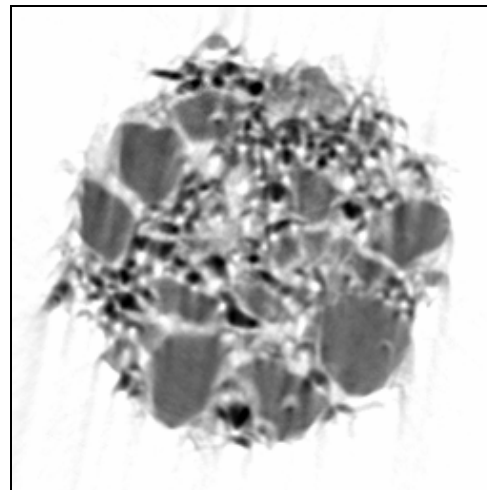
3D image segmentation

Image segmentation is one of the critical steps of image analysis and conditions the quality of measurements performed later. It allows to extract the objects of the image on which analysis relates to and to separate regions of interest from the background of the image. In the present case, this is not an easy task since most often the tomographic reconstruction amplifies the noise of the projections, and generates artefacts, resulting in impressive images for display, but with generally a too weak quality for a quantitative and automatic use. Furthermore, volumetric segmentation often proves to be more complicated than a simple transposition of 2D algorithms in 3D. Image topology frequently differs between 2D and 3D and specific approaches must be considered in each case. The algorithms were developed and implemented on the Aphelion® software. Once calibrated, they can be used automatically on sequences of images obtained on series of materials with similar properties.

Examples of slices in 3D reconstructions of two materials are shown in figures 1 and 2. Material A (figure 1) is a two-phase material (grains in dark and a binder in light-grey). Material B (figure 2) is a three component material containing small dark grains, large grains, and a binder. The resolution of these images is nearly 3 microns. Due to the acquisition of radiographs and to the numerical reconstruction, noise is apparent in the images (figure 1), as well as some linear grey-level artefacts, due to the reconstruction from a finite number of projections (figure 2).



*Fig. 1. Material A; size: 500 x 500 x 150;
resolution: 3 microns*



*Fig. 2. Material B; size: 350 x 350 x 600;
resolution: 3 microns*

These defects make the extraction of the grains difficult, and practically impossible by standard thresholding procedures, so that a specific segmentation procedure was developed. An efficient segmentation procedure developed in mathematical morphology is the watershed segmentation (Beucher, 1990), usually implemented by a flooding process (or region growing) from markers. It is used to extract the contour of grains and separate connected grains. The main difficulty of this procedure is to be able to obtain as many markers as the

number of objects in image. Figure 3 shows results of watershed segmentation with a wrong number of markers. The two possible consequences are:

- Some grains are missed by the segmentation, as they contain no marker (left image).
- Some grains contain more than one marker and they are split into several parts (right image).

To solve this problem, segmentation processes, based on a multi-scale approach of markers, were developed (V. Tariel et al.). Resulting segmentations on materials A and B are shown in figure 4.

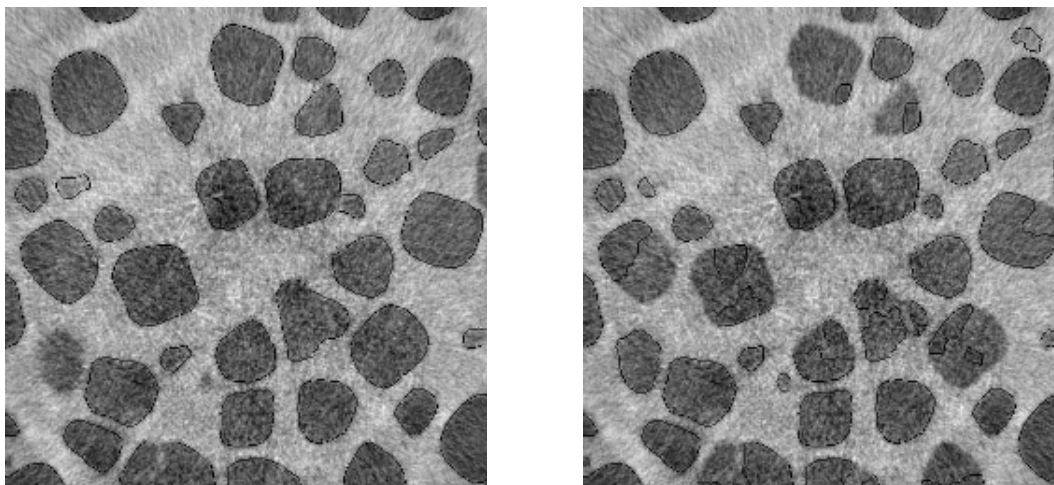


Fig. 3. Miss or split by watershed segmentation

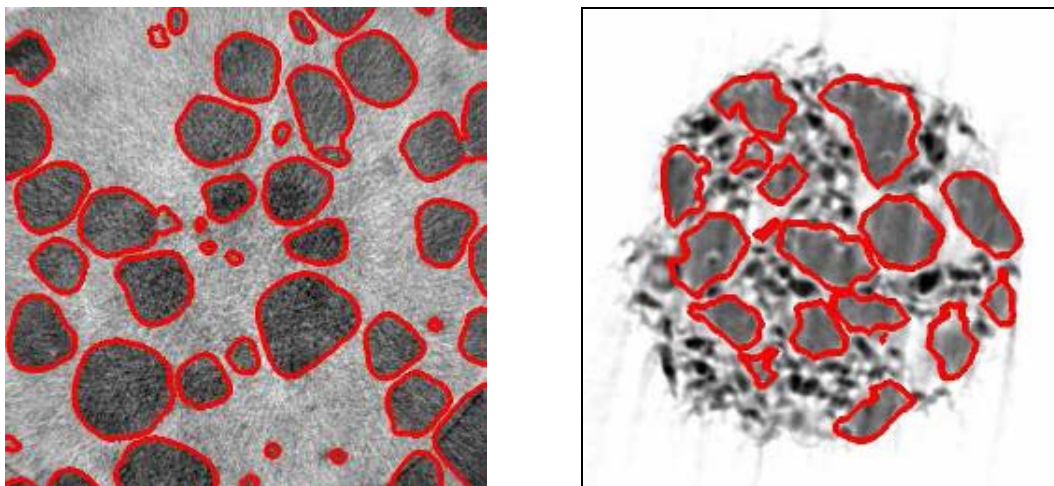
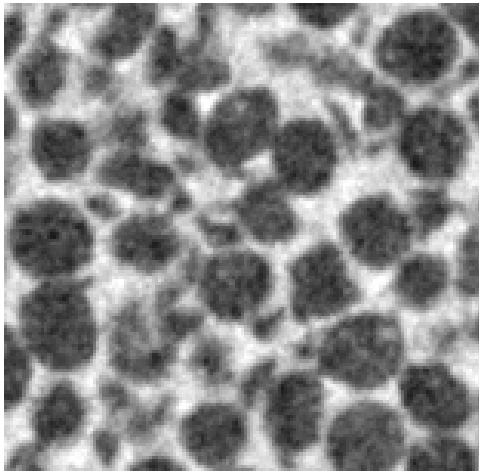


Fig. 4. Final segmentations on materials A and B

Other materials present an important amount of connected grains (especially in 3D) which have to be separated by mean of segmentation in order to permit further individual measurements. This granular phase connectivity does not reflect the effective material structure and is likely to be source of problems and incoherent physical results during the numerical calculations phase. The role of segmentation in this case is to separate grains in line with material effective morphology to be in position to extract individual grain parameters and to carry out realistic physical calculations.



*Fig. 5. Material C; size: 150 x 150 x 250;
resolution: 11 microns*

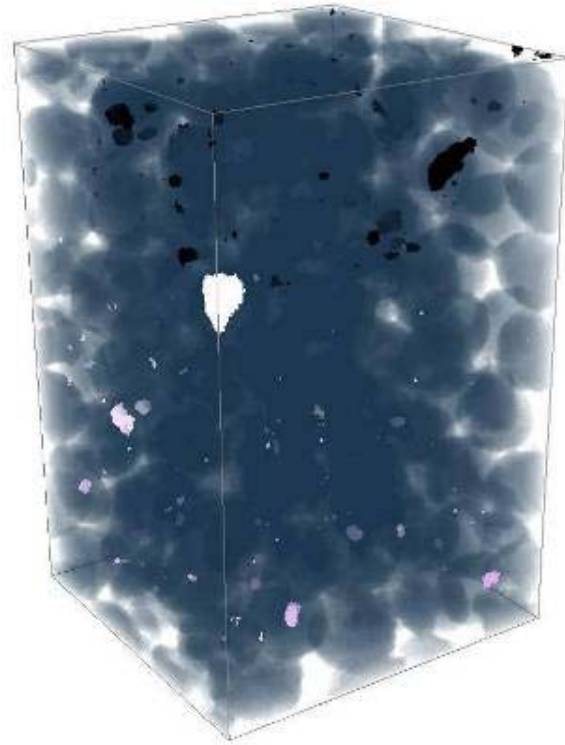


Fig. 6. 3D connected regions of material C

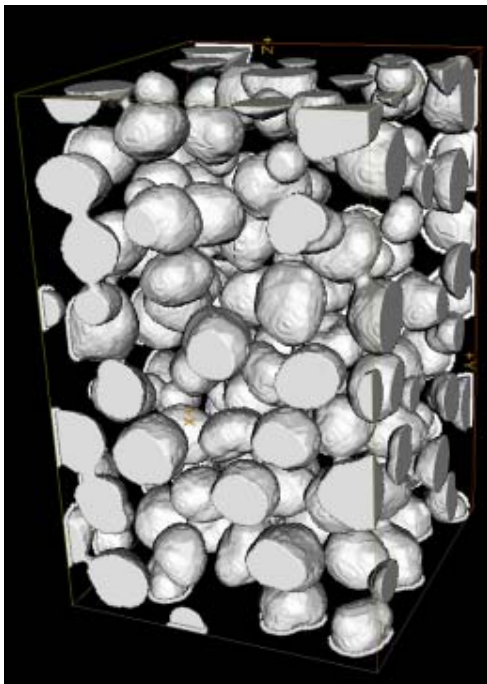


Fig. 7. 3D segmentation of material C



Fig. 8. 3D connected regions on material C segmented

Figures Fig. 5 and Fig. 6 show respectively a two components material slice and the 3D representation of the connected regions of its granular phase (one colour by connected

region). This material has a high granular volume fraction (about 60%). As we can see, if in a 2D section the dark phase does not seem to be very connected, the amount of connected regions in 3D becomes very important (the blue region of the figure Fig. 6 represents 99% of the granular phase total volume). In order to segment correctly such images, specific algorithms were developed. The result of the 3D segmentation is presented in figure 7. Figure 8 shows the corresponding region connectivity, every connected component showing the same colour.

Material characterisation

Once the segmentation process has been successfully accomplished, a whole set of morphological measurements can be performed in order to get a quantitative description of the granular media and the 3D map of the microstructure can be meshed, for a numerical calculation of homogenisation of its mechanical properties using a Finite Element code.

Since image objects have been individualized, it is possible to extract a large amount of information on their size, shape or spatial distributions (Serra, 1982, 1988). Figure 9 shows the 3D representation of drops which were projected in a foam (from top to bottom). As we can observe in figure 10, there is an important variation of the number of drops between the top and the bottom of the foam. This result can be correlated with another one, also obtained thanks to image analysis, concerning the variation of the mean drops volume versus their depth in the foam (figure 11). It appears that the drops are more numerous and smaller in low depths of material and reach deeper depths when their volume (and thus their mass) grows.

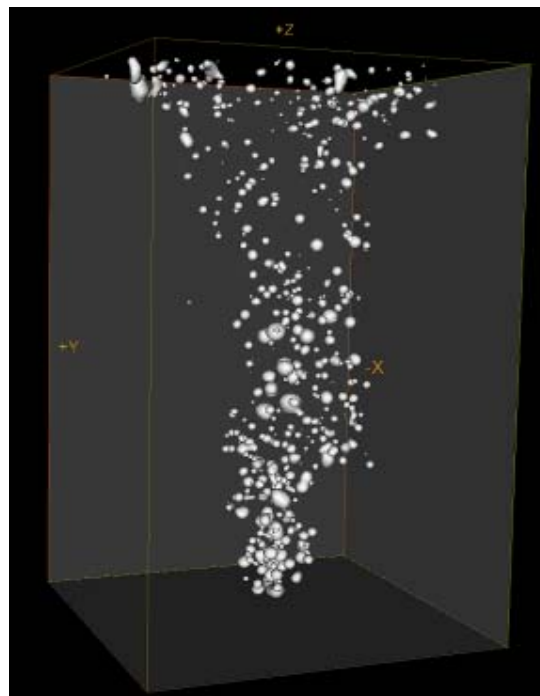


Fig. 9. 3D representation of drops contained in a foam (material D); size: 600 x 600 x 900; resolution: 8 microns

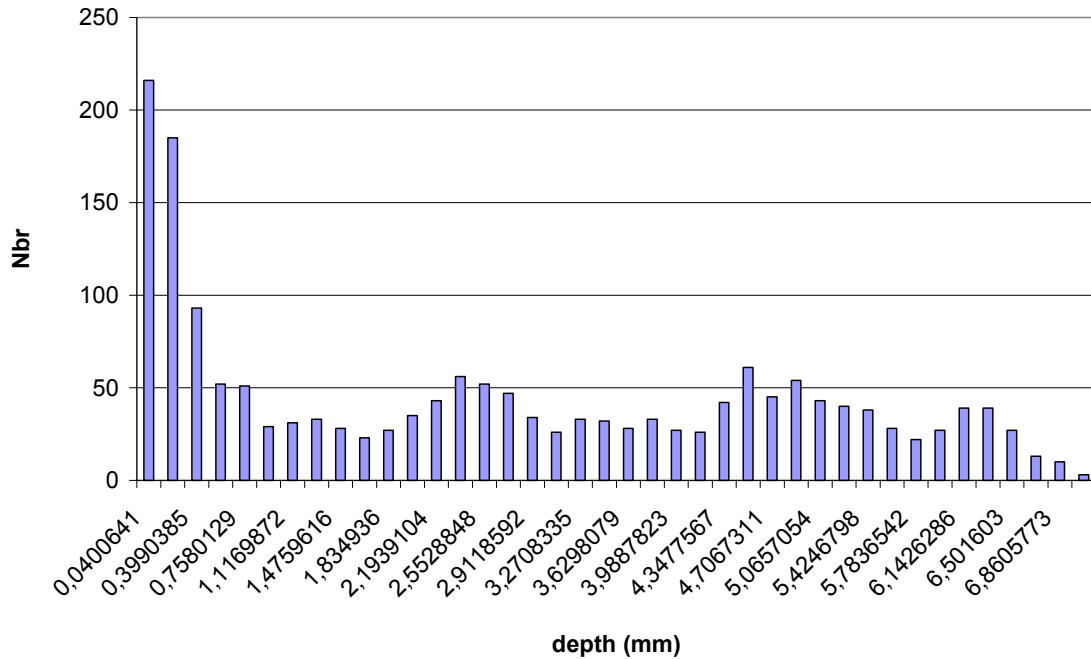


Fig. 10. Material D: drops number vs. depth

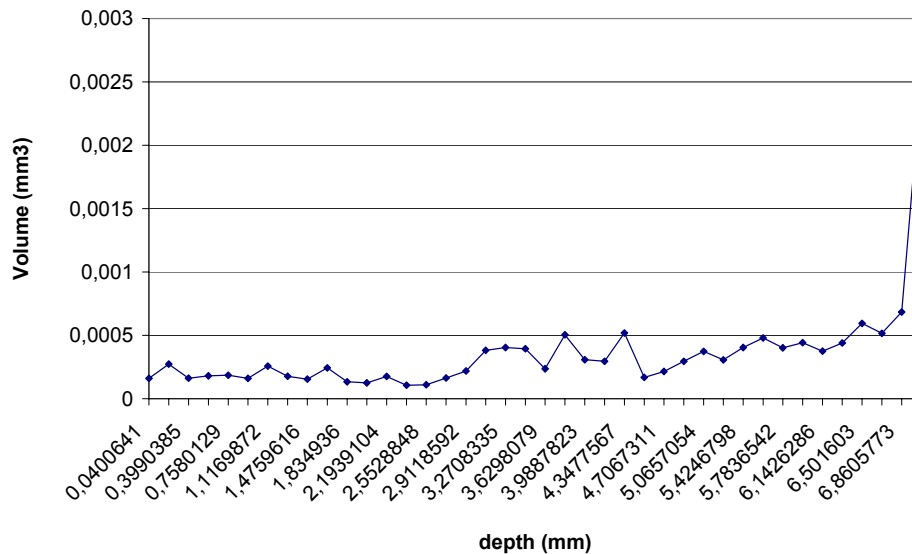


Fig. 11. Material D: mean drops volume vs. depth

3D Size distribution

Material granulometry can also be estimated by mean of mathematical morphology (Serra, 1982, 1988). In this case, granulometry is calculated thanks to a series of morphological “openings” of an image by structuring elements of increasing sizes. The pattern spectrum is the difference of the area of openings by 3D structuring elements of increasing sizes in the granulometry. We can see an example of result obtained with this method for material D in figure 12.

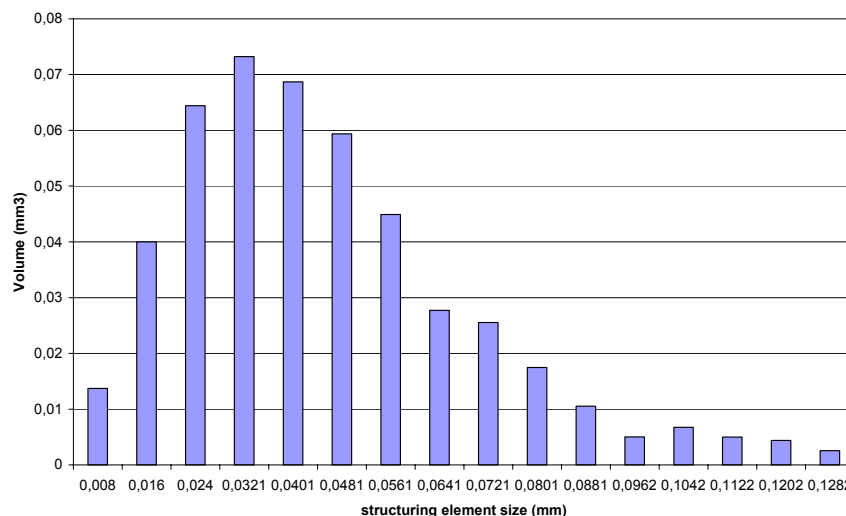


Fig. 12. Granulometry size distribution by 3D morphological openings) of material D

Scales and Covariance

Another useful tool, frequently used in image analysis, is the spatial covariance (Serra, 1982). It is defined as the probability $C(h)$ that two points separated by the vector h belong to the same component (here the grains). Various parts of this function bring information on image parameters such as the volume fraction (value of covariance in the beginning $C(0)$), mean diameter of objects (related to the slope of the covariance function at the beginning $-dC/dh(0)$), the degree of arrangement of the studied structure (presence, number and heights of peaks on the covariance curve), and mean distance of objects (from the position of the first minimum and corresponding next maximum). In addition, it gives a quantitative information on the scale (namely the correlation lengths) in different directions, which is useful for the definition of the morphological RVE (Representative Volume Element). Since this information is available in each direction, it is easy to deduce the isotropy of the material.

Figure 13 represents the spatial covariance for material B. As the covariance is the same for each direction of space, we can conclude that the material grain distribution is isotropic.

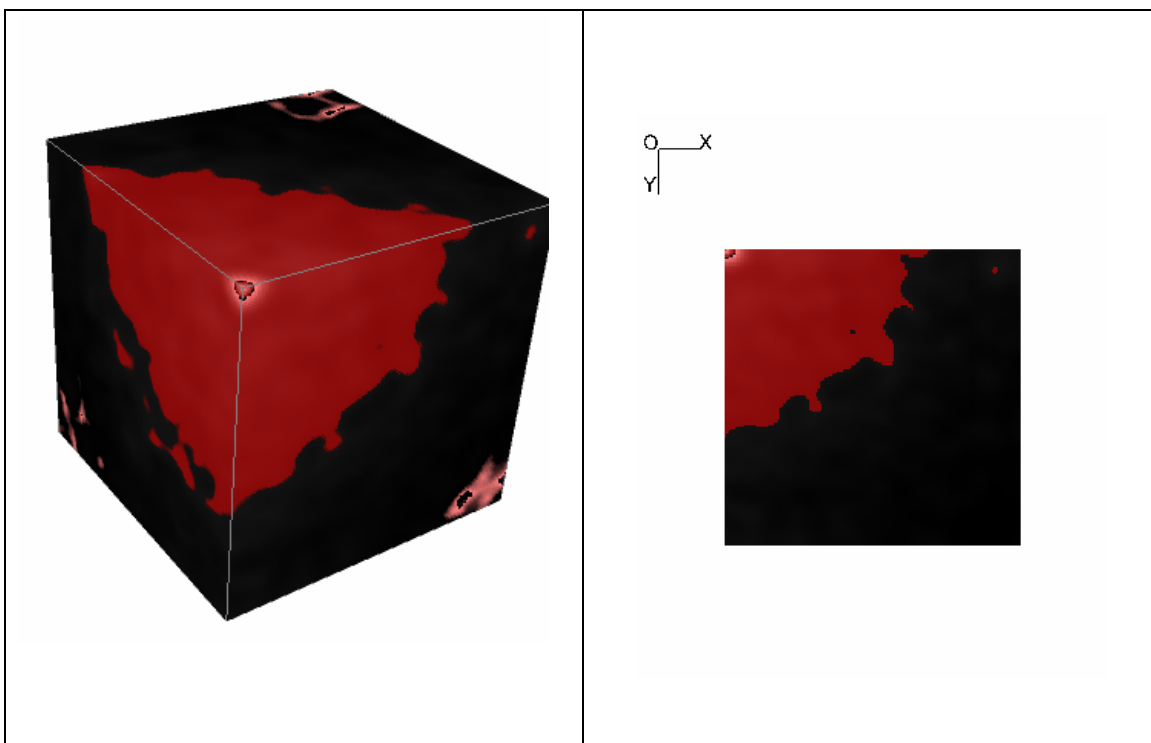


Fig. 13. Spatial covariance for material C(3D view and planar section)

Meshing of microstructures

Finally, it is also possible to use a meshing procedure of the boundary of the grains in the 3D space (figure 14). Then, the meshed image can be introduced in a finite elements code to compute stresses and strains, as well as other fields like the thermal flux and the temperature distribution in the material at a micro scale. These calculations are a first step to predict the macroscopic behaviour of the granular pyrotechnic materials, and will then help us to improve their safety and performances. Fluctuations of properties on different scales can be reached by this approach (Kanit et al., 2006).

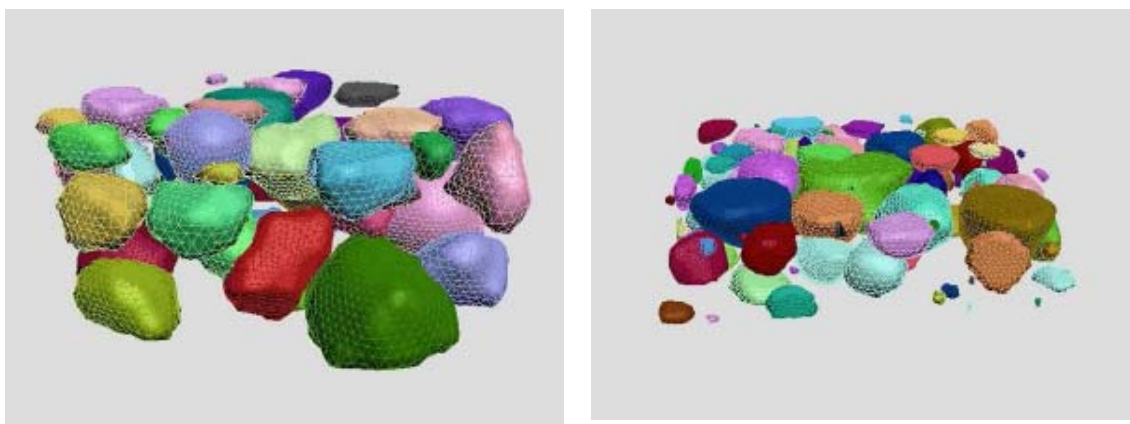


Fig. 14. Example of 3D mesh on a segmented image of a granular pyrotechnical material

Microstructure modelling

The next step of the study of pyrotechnical materials will be the development of models of random granular media. The construction of probabilistic multi-component and multi-scale models will allow us to generate realisations of 3D simulations of microstructures for the prediction of their properties (Jeulin 2001, 2005). This approach is useful to study the effects of changes in the microstructures on their physical behaviour 3D, and to design materials with optimised properties.

Conclusion

New available information on granular materials, namely their 3D microstructure studied by microtomography, combined to powerful image analysis tools developed in mathematical morphology, to finite element calculation, and to microstructure modelling will bring a new insight in the behaviour and safety of pyrotechnical materials.

References

- Beucher S (1990) Segmentation d'images et morphologie mathématique, Thesis, Ecole des Mines de Paris.
- Jeulin D., Ostoja-Starzewski, M. (eds) (2001) Mechanics of Random and Multiscale Microstructures, CISM Lecture Notes N° 430, Springer Verlag.
- Jeulin D. (2005) Random Structures in Physics, in: "Space, Structure and Randomness", Contributions in Honor of Georges Matheron in the Fields of Geostatistics, Random Sets, and Mathematical Morphology; Series: Lecture Notes in Statistics, Vol. 183, Bilodeau M., Meyer F., Schmitt M. (Eds.), 2005, XIV, Springer-Verlag, pp. 183-222.
- Kanit T., N'Guyen F., Forest S., Jeulin D., Reed M., Singleton S. (2006) Apparent and effective physical properties of heterogeneous materials: representativity of samples of two materials from food industry. *Computer Methods in Applied Mechanics and Engineering*, 2006. 195(33-36): pp. 3960-3982.
- Serra J (1982). *Image Analysis and Mathematical Morphology*, vol. I, Academic Press, London.
- Serra J. ed. (1988). *Image Analysis and Mathematical Morphology*, vol. II, Theoretical advances, Academic Press, London .
- Tariel V., Jeulin D., Fanget A., Contesse G. 3D Multi-scale segmentation of granular materials. In : *Proceedings ICS XII*, Saint-Etienne (France), August 30-September 7, 2007.

